

Multi-scale Correlation between Defects and Internal Stresses in Additively Manufactured AISI316L Structures

Von der Fakultät für Maschinenbau, Elektro- und Energiesysteme
der Brandenburgischen Technischen Universität Cottbus–Senftenberg
zur Erlangung des akademischen Grades eines
Doktor der Ingenieurwissenschaften

genehmigte Dissertation

vorgelegt von

Diplomingenieur

Alexander Ulbricht

geboren am 27.10.1980 in Ludwigsfelde

Vorsitzende: Prof. Dr.-Ing. Sabine Weiss

Gutachter: Prof. Dr. Giovanni Bruno

Gutachter: Prof. Dr. Markus Bambach

Tag der mündlichen Prüfung: 14.04.2023

Alexander Ulbricht

*Multi-scale Correlation between Defects and Internal Stresses in Additively Manufactured
AISI316L Structures*

PhD Thesis, April 14th, 2023

Reviewers: Prof. Dr. Giovanni Bruno and Prof. Dr. Markus Bambach

Supervisors: Prof. Dr. Giovanni Bruno and Prof. Dr. Markus Bambach

Mentor: Dr. Alexander Evans

Brandenburgische Technische Universität Cottbus-Senftenberg

Fakultät für Maschinenbau, Elektro- und Energiesysteme

Platz der Deutschen Einheit 1

03046 Cottbus

<https://doi.org/10.26127/BTUOpen-6374>

Contents

Abstract	vii
Zusammenfassung	ix
Acknowledgement	xi
List of Figures	xvii
List of Tables	xxiii
List of Abbreviations	xxv
1 Introduction	1
1.1 Additive Manufacturing	1
1.2 Laser Powder Bed Fusion	2
1.3 State of the Art	3
1.3.1 Void Formation Mechanisms in PBF-LB/M/316L	4
1.3.2 Residual Stress Formation Mechanisms in PBF-LB/M/316L	6
1.3.3 Damage Formation in Quasi-Static Loaded PBF-LB/M/316L	8
1.4 Motivation & Aims	9
1.5 Embedding of this Thesis into Existing Research Projects	10
2 Theoretical Background	13
2.1 X-ray Computed Tomography	13
2.1.1 Working Principle of Laboratory XCT	14
2.1.2 X-ray Radiation	15
2.1.3 Image Reconstruction in Laboratory XCT	18
2.1.4 Synchrotron Computed Tomography	22
2.1.5 Data Treatment	23
2.2 Residual Stress Determination by Neutron Diffraction	24
2.2.1 Residual Stresses and Their Classification	24
2.2.2 Description of Residual Stresses	25
2.2.3 Neutron Diffraction Techniques for the Analysis of Residual Stress	27

3	Material & Manufacturing	31
3.1	PBF-LB/M/316L Machine Parameter	31
3.2	AISI Stainless Steel 316L	32
3.3	Specimens	34
3.3.1	Specimens for Tensile and Creep Tests	34
3.3.2	Specimens for the Analysis of Artificial Voids	36
3.3.3	Specimens for Residual Stress Analysis	38
4	Experimental Details & Results	41
4.1	Void Formation in PBF-LB/M/316L Using Standard Build Parameters	41
4.1.1	Experimental Details	41
4.1.2	Results	43
4.2	Void Formation in PBF-LB/M/316L by Varying the Scan Speed	46
4.2.1	Experimental Details	46
4.2.2	Results	46
4.3	Void Formation in PBF-LB/M/316L by Varying the Layer Thickness .	52
4.3.1	Experimental Details	52
4.3.2	Results	53
4.4	Residual Stress and Porosity in Prisms	57
4.4.1	Experimental Details of the Determination of Residual Stress .	57
4.4.2	Results of Residual Stress Determination	58
4.4.3	Experimental Details of the Determination of the Mesostructure	61
4.4.4	Results: Defect Characterisation	62
4.5	Interlink between Porosity and Damage from Mechanical Loads . . .	65
4.5.1	Experimental Details	65
4.5.2	Results	67
5	Discussion on Defect and Residual Stress Formation	83
5.1	Why to Focus on Void Formation?	83
5.2	The Process of Void Formation in PBF-LB/M/316L	84
5.3	Residual Stresses in PBF-LB/M/316L	90
5.4	Damage Formation in High Temperature Creep and Tensile Deformed PBF-LB/M/316L	94
6	Summary and Concluding Remarks	103
6.1	Void Formation in PBF-LB/M/316L	103
6.2	Residual Stress Formation in PBF-LB/M/316L	103
6.3	Damage in PBF-LB/M/316L	104
6.4	Concluding Remarks	104

7 Outlook & Future Research	107
7.1 Advancements in Imaging	107
7.2 Advancements in Residual Stress Analysis	108
Bibliography	111

Abstract

“ *Science, my boy, is made up of mistakes, but they are mistakes which it is useful to make, because they lead little by little to the truth.*

— **Jules Verne**

(Journey to the Center of the Earth)

Additive Manufacturing of metals has become relevant for industrial applications. The near net-shape production of components produced by Laser Powder Bed Fusion (PBF-LB/M) enables new possibilities in component design combined with a reduction of the amount of needed material. Omitting the extra material, that was part of conventionally produced components due to machining constraints, results in components which in consequence lack the inherent additional safety margins provided by the higher material consumption of conventionally produced components. Therefore, to use PBF-LB/M metals in safety critical applications an in-depth understanding of porosity and internal stresses in parts made by PBF-LB/M is needed. Only non-destructive testing methods—such as computed tomography and residual stress analysis using neutrons—enable the assessment of porosity and stresses in the whole part. In this thesis I tackled creep and tensile static deformed specimens to fill research gaps in this field in terms of analysing PBF-LB/M stainless steel AISI 316L: from structural properties to in-situ behaviour.

The initial void population of AISI 316L is studied using X-ray and synchrotron micro computed tomography. Specimens produced with different process parameters were analysed to quantify the influence of process parameters on the initial void population. The possibility to close voids using the laser illumination of subsequent layers is discussed by a quantitative study of the ability of the laser to melt different multiples of the applied layer thickness.

The formation of internal stress is inherent to components produced by the PBF-LB/M process. These stresses remain in the components after production as residual stresses. In this thesis a study is presented which aims to unravel the mechanisms that define the spatial distribution of the residual stresses, and their magnitude.

In the end, the population of internal voids during mechanical testing is studied by X-ray micro computed tomography. The evolution of damage accumulation in creep specimens is studied at different stages of the creep test. Results are compared to a creep tested conventionally made specimen and to a PBF-LB/M specimen from a tensile test. An interconnection between the PBF-LB/M microstructure and the pattern of damage is revealed.

Zusammenfassung

„ *Wissenschaft, mein Freund, besteht aus Fehlern. Fehlern, die gemacht werden müssen, um der Wahrheit Schritt für Schritt näher zu kommen.*

— **Jules Verne**

(Die Reise zum Mittelpunkt der Erde)

Die additive Fertigung wird immer relevanter für industrielle Anwendungen. Insbesondere der Laser Powder Bed Fusion (PBF-LB/M) Prozess ermöglicht die Herstellung endformnaher metallischer Bauteile, die sich durch dadurch auszeichnen, dass sich durch die nahezu grenzenlose Designfreiheit Bauteile realisieren lassen, deren Materialeinsatz auf ein Minimum reduziert werden kann. Diese Reduktion hat aber zur Folge, dass mittels PBF-LB/M produzierten Bauteilen die zusätzliche Bauteilsicherheit fehlt, die konventionell produzierte Bauteile durch ihr „Mehr“ an eingesetztem Material aufweisen können. Daher ist es, um den Einsatz von PBF-LB/M-Bauteilen in sicherheitskritischen Anwendungen zu ermöglichen, umso wichtiger, ein genaues Verständnis über die Porosität und innere Spannungen in PBF-LB/M Bauteilen zu erhalten. Zerstörungsfreie Messmethoden, wie Computertomographie und Spannungsanalyse mittels Neutronenbeugung, ermöglichen es, das gesamte Bauteil zu analysieren. Diese Doktorarbeit setzt sich zum Ziel, das Wissen über Edelstahl AISI 316L aus dem PBF-LB/M Prozess zu vertiefen: von strukturellen Eigenschaften bis zum in-situ Verhalten.

Der initiale Anteil an Fehlstellen in PBF-LB/M AISI 316L wird mittels Labor- und Synchrotron Röntgenmikrocomputertomographie quantitativ erfasst. Dafür werden Proben, die mit unterschiedlichen Herstellungsparametern produziert wurden, analysiert, um den Einfluss der Herstellungsparameter auf den Fehlstellenanteil in AISI 316L zu bestimmen. Des Weiteren wird die Möglichkeit, bestehende Fehlstellen durch die Laser-Belichtung der nachfolgenden Schichten zu schließen, diskutiert. Dazu wird die Fähigkeit des Lasers, verschiedene Vielfache der Pulverschichtdicke aufzuschmelzen, quantitativ untersucht.

Das Auftreten innerer Spannungen ist eine inhärente Eigenschaft von Bauteilen des PBF-LB/M-Prozesses. Diese inneren Spannungen verbleiben nach dem Bauprozess

als Eigenspannungen im Bauteil. Im Rahmen dieser Doktorarbeit wird untersucht, welche der Mechanismen, die zur Entstehung innerer Spannungen führen, sich wie auf deren räumliche Verteilung im Bauteil auswirken und welche die Größenordnung der Spannungen in AISI 316L bestimmen.

Schlussendlich wird das Auftreten interner Fehlstellen und ihre räumliche Verteilung bei werkstoffmechanischen Versuchen untersucht. Dazu wird der Fehlstellenanteil in PBF-LB/M Kriechproben in verschiedenen Stadien von Kriechversuchen mittels Laborröntgencomputertomographie bestimmt. Diese Ergebnisse werden mit Ergebnissen vergleichbar belasteter konventionell hergestellter Kriechproben, sowie mit PBF-LB/M-Zugproben verglichen. Dabei konnte ein Zusammenhang zwischen der Mikrostruktur des PBF-LB/M-Materials und dem Muster der Fehlstellenverteilung hergestellt werden.

Acknowledgement

” *All energy is only borrowed and one day you have to give it back.*

— **James Cameron**
(Avatar)

First of all, I like to acknowledge my supervisor Giovanni Bruno for giving me the opportunity to fulfil my childhood dream of becoming a proper scientist. His open-mindedness to new ideas combined with his down-to-earth approach to solve problems was a great motivation to finish this work. The supportive team spirit he created in our division 8.5 at BAM encouraged me to ask questions, which improved my scientific work.

I also want to acknowledge my mentor Alex Evans for his support, his comments and the long and fruitful discussions which in the end made me improve this thesis to its current state.

From our team at division 8.5 I especially want to thank Dietmar for sharing with me his almost endless experience with XCT. Itziar, Jakob, Max, Sergei, Tatiana, Tobias and again Alex for discussions, support and fun—especially during these sometimes endless neutron and synchrotron beam times (Why did problems always occur when we wanted to leave?). Also Bernd and Bianca were a tremendous help especially when it comes to administrative barriers at BAM. I also thank Andreas, Carsten, Christian, Fabien and Michael for taking their time to help me solve problems. In addition I acknowledge all the members of the AGIL and ProMoAM project whose work was the foundation to do mine. I especially want to thank Gunther, Luis, Simon and Simon. But this PhD would not be possible in the current state without Prof. Markus Bambach.

I thank my parents and family for their support on this long journey. Last but not least I want to thank my beloved girlfriend Lisa for her moral support during the long period of writing this thesis, for her love and unlimited cheerfulness.

Berlin, in December 2022

Alexander Ulbricht

List of Publications

Journal Articles

1. G. Mohr, S. J. Altenburg, A. Ulbricht, P. Heinrich, D. Baum, C. Maierhofer, K. Hilgenberg:
In-Situ Defect Detection in Laser Powder Bed Fusion by Using Thermography and Optical Tomography—Comparison to Computed Tomography.
Metals, Vol. 10, No. 1, **2020**
<https://doi.org/10.3390/met10010103>
2. A. Ulbricht, C. Gollwitzer, A. Kupsch, F. Léonard, B. R. Müller, T. Oesch, Y. Onel, T. Thiede, U. Zscherpel:
Moderne Methoden der CT-gestützten Strukturanalyse.
tm - Technisches Messen, 87(2), 81-92, **2020**
<https://doi.org/10.1515/teme-2019-0125>
3. A. Ulbricht, S. J. Altenburg, M. Sprengel, K. Sommer, G. Mohr, T. Fritsch, T. Mishurova, I. Serrano-Munoz, A. Evans, M. Hofmann, G. Bruno:
Separation of the Formation Mechanisms of Residual Stresses in LPBF 316L.
Metals, Vol. 10, No. 9, **2020**
<https://doi.org/10.3390/met10091234>
4. P. Scholz, A. Ulbricht, Y. Joshi, C. Gollwitzer, S. Weidner:
Microstructure of polymer-imprinted metal–organic frame works determined by absorption edge tomography Additive Manufacturing Hybrid Demonstrator.
International Journal of Materials Research, Vol. 111, No. 1, 55-64, **2020**
<https://doi.org/10.3139/146.111817>
5. T. Mishurova, B. Sydow, T. Thiede, I. Sizova, A. Ulbricht, M. Bambach, G. Bruno:
Residual Stress and Microstructure of a Ti-6Al-4V Wire Arc Additive Manufacturing Hybrid Demonstrator.
Metals, Vol. 10, No. 6, **2020**
<https://doi.org/10.3390/met10060701>

6. A. Ulbricht, G. Mohr, S. J. Altenburg, S. Oster, C. Maierhofer, G. Bruno:
Can Potential Defects in LPBF Be Healed from the Laser Exposure of Subsequent Layers? A Quantitative Study.
Metals, Vol. 17, No. 7, 2021
<https://doi.org/10.3390/met11071012>

7. A. Charmi, R. Falkenberg, L. A. Ávila, G. Mohr, K. Sommer, A. Ulbricht, M. Sprengel, R. Saliwan Neumann, B. Skrotzki, A. Evans:
Mechanical anisotropy of additively manufactured stainless steel 316L: An experimental and numerical study.
Materials Science and Engineering: A, Vol. 799, p. 140154, 2021
<https://doi.org/10.1016/j.msea.2020.140154>

8. I. Serrano-Munoz, T. Fritsch, T. Mishurova, A. Trofimov, D. Apel, A. Ulbricht, A. Kromm, R. Hesse, A. Evans, G. Bruno:
On the interplay of microstructure and residual stress in LPBF IN718.
Journal of Materials Science, Vol. 56, 5845–5867, 2021
<https://doi.org/10.1007/s10853-020-05553-y>

9. I. Serrano-Munoz, A. Ulbricht, T. Fritsch, T. Mishurova, A. Kromm, M. Hofmann, R. C. Wimpory, A. Evans, G. Bruno:
Scanning Manufacturing Parameters Determining the Residual Stress State in LPBF IN718 Small Parts.
Advanced Engineering Materials, Vol. 23, 2100158, 2021
<https://doi.org/10.1002/adem.202100158>

10. M. Sprengel, A. Ulbricht, A. Evans, A. Kromm, K. Sommer, T. Werner, J. Kellerher, G. Bruno, T. Kannengießler:
Towards the optimization of post-laser powder bed fusion stress-relieve treatments of stainless steel 316L.
Metallurgical and Materials Transactions A, Vol. 52, 5342–5356, 2021
<https://doi.org/10.1007/s11661-021-06472-6>

11. J. Schröder, A. Evans, T. Mishurova, A. Ulbricht, M. Sprengel, I. Serrano-Munoz, T. Fritsch, A. Kromm, T. Kannengießler, G. Bruno:
Diffraction-Based Residual Stress Characterization in Laser Additive Manufacturing of Metals.
Metals, Vol. 11, No. 11, 2021
<https://doi.org/10.3390/met11111830>

12. L. A. Ávila Calderón, B. Rehmer, S. Schriever, A. Ulbricht, L. A. Jácome, K. Sommer, G. Mohr, B. Skrotzki, A. Evans:
Creep and creep damage behavior of stainless steel 316L manufactured by laser powder bed fusion.
Materials Science and Engineering: A, Vol. 830, p. 142223, **2022**
<https://doi.org/10.1016/j.msea.2021.142223>
13. E. D'Accardi, R. Krankenhagen, A. Ulbricht, M. Pelkner, R. Pohl, D. Palumbo, U. Galietti:
Capability to detect and localize typical defects of laser power bed fusion process: an experimental investigation with different non destructive techniques.
Progress in Additive Manufacturing, **2022**
<https://doi.org/10.1007/s40964-022-00297-4>
14. S. Oster, T. Fritsch, A. Ulbricht, G. Mohr, G. Bruno, C. Maierhofer, S. J. Altenburg:
On the registration of thermographic in-situ monitoring data and computed tomography reference data in the scope of defect prediction in laser powder bed fusion — an in-depth study.
Metals, Vol. 12, No. 6, **2022**
<https://doi.org/10.3390/met12060947>
15. H. Markötter, B. R. Müller, A. Kupsch, S. Evsevlev, T. Arlt, A. Ulbricht, S. Dayani, G. Bruno:
A review of the X-ray Imaging at the BAMline (BESSY II).
Advanced Engineering Materials, 2201034, **2023**
<https://doi.org/10.1002/adem.202201034>
16. A. Ulbricht, L. A. Ávila Calderón., K. Sommer, G. Mohr, A. Evans, B. Skrotzki, G. Bruno: **Evolution of Creep Damage of 316L produced by Laser Powder Bed Fusion.**
Advanced Engineering Materials, 2201581, **2023**
<https://doi.org/10.10.1002/adem.202201581>


Conference Papers

1. T. Mishurova, I. Serrano-Munoz, T. Fritsch, A. Ulbricht, M. Sprengel, A. Evans, A. Kromm, M. Madia, G. Bruno:
A Critical Discussion on the Diffraction-Based Experimental Determination of Residual Stress in AM Parts.
Structural Integrity of Additive Manufactured Materials and Parts, ed. N. Shamsaei and M. Seifi, 122-138, **2020**
ASTM International, 7th-10th October 2019, National Harbor, MD, USA
<https://doi.org/10.1520/STP163120190148>
2. E. D'Accardi, A. Ulbricht, R. Krankenhagen, D. Palumbo, U. Galietti:
Capability of active thermography to detect and localize pores in Metal Additive Manufacturing materials.
IOP Conf. Ser.: Mater. Sci. Eng., 1038, 012018, **2020**
The 49th AIAS Conference (AIAS 2020), 2nd-5th September 2020, Genova, Italy
<https://doi.org/10.1088/1757-899X/1038/1/012018>
3. S. Oster, C. Maierhofer, G. Mohr, K. Hilgenberg, A. Ulbricht, S. J. Altenburg:
Investigation of the thermal history of L-PBF metal parts by feature extraction from in-situ SWIR thermography.
Proc. SPIE 11743, Thermosense: Thermal Infrared Applications, XLIII, 7430C, **2021**
SPIE Defense + Commercial Sensing, 12th-17th April 2021, Florida, United States (online only)
<https://doi.org/10.1117/12.2587913>

List of Figures

1.1	Principle sketch of a Laser Powder Bed Fusion of Metals (PBF-LB/M) system	2
1.2	Orientation maps of Laser Powder Bed Fusion of AISI Stainless Steel 316L (PBF-LB/M/316L) manufactured at different Inter-Layer Dwell Time (ILT) [19] showing columnar grain orientation	4
1.3	General illustration of Lack-of-Fusion (LoF) void formation	6
2.1	Principle sketch of a laboratory X-ray Computed Tomography (XCT) set-up	14
2.2	Basic principle of back-projections: All acquired projections are positioned around a virtual centre. The projections are projected to this virtual centre. The point of view of the projections shown in this sketch is marked by a yellow arrow in fig. 2.1	14
2.3	X-ray absorption	16
2.4	The connection between object space, Radon space (<i>i.e.</i> , sinogram) and Fourier space.	19
2.5	Blurring of the projection due to deviation of the physical focal spot size from a ideal point source	21
2.6	General sketch of a Synchrotron X-ray Computed Tomography (SXCT) set-up: The parallel X-Ray beam transmits the sample and is converted into visible light by the scintillator. The visible light is imaged onto the CCD-screen after magnification by an optical lens.	23
2.7	Length scale of residual stresses	25
2.8	Diffraction at lattice planes of a crystalline structure under compression d_C , stress-free d_0 and under tension d_T	28
2.9	Schematic of the STRESS-SPEC beamline at MLZ, Garching, Germany .	29
3.1	Build angle of the compared specimen extracted from built tower and wall geometries as depicted in the paper by Charmi et al. [17]	32
3.2	Creep curves of the investigated specimens of table 3.5. t_i marks the point of interruption of the tests as presented in the paper of Ávila et al. [67]	35
3.3	Shape of the specimen DPK002	36
3.4	DPK003-A specimen	37

3.5	Schematics of the two border fill scan strategies and photo of the produced specimens	39
4.1	Tensile specimen scanned at 3 heights	43
4.2	Tensile specimen scanned at 3 heights	44
4.3	Magnified view of an average sized pore in the tensile specimen	44
4.4	Largest and smallest void found in a small pin extracted from a wall geometry	46
4.5	Comparison between XCT and metallurgic cuts showing the High-Volumetric Energy Density (VED) tower (at the left in both images), the Low-VED tower (at the right in both images) and the base section produced using the optimal VED (at the bottom in both images)	47
4.6	Distribution of internal voids in the Low-VED tower (at the left in both images) and the High-VED tower (at the right in both images)	49
4.7	Virtual transversal cut at the height of the ninth layer ($450\mu\text{m}$) of the Low-VED tower. Larger voids are filled with unmolten powder particles.	50
4.8	Virtual cuts combined with the CAD revealing the <i>healed</i> non-exposed corner	51
4.9	3D-rendering of the void distribution in the cylindrical specimen. Images taken from Ulbricht et al. [38]	53
4.10	Segmented voids in Q4–Q6 showing only a limited amount of voids formed at the periphery of the non-exposed quarters. Images taken from Ulbricht et al. [38]	54
4.11	Segmented voids in Q7–Q9 showing the structured voids. Images taken from Ulbricht et al. [38]	55
4.12	Visualisation of the porosity per quarter given in table 4.10	56
4.13	Virtual cut from the mid of the inner cylinder showing the borders of Q9 (upper blue frame) and Q8 (lower blue frame). Yellow lines emphasise the structure of the internal surfaces. Images taken from Ulbricht et al. [38]	56
4.14	ND measurement positions in the mid height plane	58
4.15	Comparison of Residual Stress (RS) maps of the two scan strategies including results from laboratory X-ray diffraction at the surface (<i>The big semi-translucent squares in the bulk represent the almost cubic Neutron Diffraction (ND) gauge volume (orientated differently for different stress components), whereas the small semi-translucent squares at the edges represent the laboratory X-ray measurement positions</i>). Images taken from Ulbricht et al. [39]	60

4.16	Line scans in both samples for all three orthogonal directions using the combined data from ND and laboratory X-ray Diffraction (XRD). Images taken from Ulbricht et al. [39]	61
4.17	XCT reconstructions of the ND reference cube sectioned from a twin  Perimeter-to-Centre (PtC) specimen. Images taken from Ulbricht et al. [39]	63
4.18	Comparison of the radiograms and XCT emphasising the internal defect structure of the prisms. In both bottom corners of the specimen an accumulation of voids was observed.	64
4.19	Combined image showing the four studied creep specimens. Photographs of the PBF-LB/M/316L specimen K01 and the hot rolled specimen A5.12 were taken after the XCT scans when the two specimens were already cut for further analysis. Original images provided by Luis Ávila.	67
4.20	3D rendering of the broken hot rolled creep specimen. The two parts were virtually merged.	68
4.21	3D rendering of the bottom end of the hot rolled creep specimen. (in respect to the orientation of the virtually merged parts depicted in 4.20)	68
4.22	3D rendering of the broken creep specimen K04. The two parts were virtually merged.	70
4.23	3D rendering of longer bottom section (in respect to the build direction) of the broken specimen K04. Rupture surface and internal void distribution is shown.	70
4.24	Rendering of several voids. Comparison of PBF-LB/M/316L and hot rolled material at the same scale.	71
4.25	Virtual cuts of the bottom section of K04 showing crack growth by connecting to clusters	72
4.26	XCT reconstructions of creep specimen K01 at different stages of mechanical testing. The void spatial distribution is shown.	74
4.27	3D rendering of the void distribution in the creep specimen K01 before the test and at the interrupt time of $t_i = 143$ h	74
4.28	3D rendering of the biggest void in the creep specimen K01 at t_0 and at the interrupt time of $t_i = 143$ h	75
4.29	XCT reconstructions of creep specimen K05 at different stages of mechanical testing. The void spatial distribution is shown.	76
4.30	3D rendering of the void distribution in the creep specimen K05 before the test and at the interrupt time of $t_i = 44.8$ h	76
4.31	3D rendering of the bottom part (closest to the build plate) of K05 . . .	77
4.32	XCT reconstructions of bottom part (closest to the build plate) of creep specimen K05. Void distribution in the short part is shown	77

4.33	3D rendering of the broken tensile specimen. The two parts were virtually merged.	79
4.34	Virtual cut at the diameter of the bottom part.	80
4.35	3D rendering of the bottom part's rupture surface.	80
4.36	Virtual cut of the bottom part of the fractured tensile specimen. Segmented voids are closed voids. Non-segmented voids are open to the rupture surface.	81
5.1	General illustration of the influence of shape, orientation and positioning of voids becoming potential defects respective to external loads	84
5.2	Optical tomography of the laser exposure of the layers below and above the non-exposed quarter Q9. Images taken from Ulbricht et al. [38]	86
5.3	Combination of the void distribution obtained from XCT and hatching orientation obtained from Optical Tomography (OT). The angles were obtained from the analysis of the XCT data. Images taken from Ulbricht et al. [38]	87
5.4	Third orientation of LoF voids obtained from the combination of virtual cuts of the XCT data and OT images from the last fully illuminated layer below the quarters. Images taken from Ulbricht et al. [38]	89
5.5	Uncalibrated apparent maximum surface temperature obtained from thermography data acquired <i>during</i> the build process at the sample's mid build height. Each border fill scan started and ended at the bottom right hand. Fig. a) and b) display the mid-height layer, fig. c) and d) display an average of 40 layers at the mid-height. Images taken from Ulbricht et al. [39]	91
5.6	Cooling rates determined by the difference between images taken at $t_1 = 1$ ms and $t_2 = 2$ ms after an apparent surface temperature of 700 K was observed at. Fig. a) and b) display the mid-height layer, fig. c) and d) display an average of 40 layers around the middle of the total build height. Images taken from Ulbricht et al. [39]	92
5.7	Normal (<i>i.e.</i> , build direction) stress component (contour lines) in MPa (fig. 4.15e-f) combined with thermography results (fig. 5.5c-d) to highlight the compressive stresses at the laser's turn locations. Images taken from Ulbricht et al. [39]	94
5.8	Combination of XCT images of K04 and microscopy images of a similar untested specimen of the same microstructure. The microscopy images of the microstructure were obtained from a similar PBF-LB/M/316L specimen and were scaled to match the resolution of the XCT images. The microscopy images were provided by Konstantin Sommer.	96

5.9	3D rendering of the void distribution in the longer bottom part of the broken tensile specimen	99
5.10	Three distinct voids of different shape are marked in the longer bottom part of the broken tensile specimen	100
5.11	3D rendering of the three shapes of voids found in the broken tensile specimen.	101

List of Tables

3.1	Optimal machine parameters for AISI 316L as suggested by the machine manufacturer SLM Solutions GmbH	32
3.2	Characteristics of the AISI 316L Powder Particles	33
3.3	Chemical composition of the AISI 316L Powder as provided by its supplier	33
3.4	Chemical composition of the conventional hot rolled AISI 316L material	34
3.5	Experimental data of the creep tests of the PBF-LB/M/316L specimens K01, K04, K05 and the conventional hot rolled specimen as presented in the paper of Ávila et al. [67]	35
3.6	Overview of the position and characteristics of the non-exposed quarters. The height to be exposed included the height of the non-exposed quarter plus the thickness of the first fully exposed layer above ($50\mu\text{m}$)	38
4.1	Acquisition parameters for a tensile specimen scanned at three different heights	42
4.2	Acquisition parameters for tensile specimens	42
4.3	SXCT acquisition parameters for the small pin extracted from the wall .	42
4.4	XCT acquisition parameters for the small pin extracted from the wall . .	43
4.5	Acquisition parameters for tensile specimens obtained from three build angles	45
4.6	Acquisition Parameters for DPK002	46
4.7	Porosity values of the three sections	48
4.8	Acquisition Parameters for the overview scan	52
4.9	Acquisition Parameters for tensile specimens	52
4.10	Porosity values in the 9 quarters. The nominal porosity of each quarter would be 100 % (assuming all powder particles are removed)	54
4.11	Distribution of orthogonal d_0^{311} -spacing values of the reference cube . .	59
4.12	Acquisition parameters for the scan of the stress-free cube	61
4.13	Acquisition parameters for the scan of the grid of stress-free cubes . . .	62
4.14	Acquisition parameters for the hot rolled specimen and the PBF-LB/M/316L specimen K04 in their broken state (The long and short broken part of each specimen were scanned separately)	66
4.15	Acquisition parameters for K01 and K05 in the before and intermediate state	66

4.16	Acquisition parameters for K01 and K05 in their broken state (The long and short broken part of each specimen were scanned separately)	67
4.17	Parallel length of the creep specimen obtained from XCT data.	73
5.1	Hatch orientation obtained from XCT and matching OT layer orientation	89

List of Abbreviations

AISI	American Iron and Steel Institute
AM	Additive Manufacturing
BAM	Bundesanstalt für Materialforschung und -prüfung (Federal Institute for Materials Research and Testing, Berlin, Germany)
CAD	Computer Aided Design
CCD	Charge-Coupled Device
CNC	Computer Numerical Control
CSSM	Constrained Solidification Shrinkage Mechanism
CtP	Centre-to-Perimeter
DED-LB/M	Direct Energy Deposition using a Laser Beam
DED-Arc	Wire Arc Additive Manufacturing
FBP	Filtered Back-Projection
fcc	face-centered cubic
ILT	Inter-Layer Dwell Time
LoF	Lack-of-Fusion
ND	Neutron Diffraction
NDT	Non-Destructive Testing
ML	Machine Learning
OT	Optical Tomography
PBF-LB/M/316L	Laser Powder Bed Fusion of AISI Stainless Steel 316L
PBF-LB/M	Laser Powder Bed Fusion of Metals
PtC	Perimeter-to-Centre

RoI	Region-of-Interest
RS	Residual Stress
SDD	Source-Detector Distance
SNR	Signal-to-Noise Ratio
SOD	Source-Object Distance
SS	Stainless Steel
SXCT	Synchrotron X-ray Computed Tomography
TGM	Temperature Gradient Mechanism
VED	Volumetric Energy Density
XCT	X-ray Computed Tomography
XRD	X-ray Diffraction

” *We are stuck with technology when what we really want is just stuff that works.*

— **Douglas Adams**
(The Salmon of Doubt)

1.1 Additive Manufacturing

The international standards organisation *ASTM International* (formerly known as *American Society for Testing and Materials*) describes Additive Manufacturing (AM) as a “process of joining materials to make objects from 3D model data, usually layer upon layer, as opposed to subtractive manufacturing methodologies” [1]. This general description of AM is valid for many different types of materials. In industrial applications mainly polymers, ceramics and metals are used as the feedstock material [2]. The main advantage of AM is the increased freedom of design choices when compared to conventional subtractive manufacturing methods [3]. Sophisticated subtractive manufacturing techniques to be compared against are Computer Numerical Control (CNC) machines. Here, software controlled application of different tools, such as drills, saws, or grinders, mounted to a robotic arm, shape the final form of an object by removing material. The main constraint of these techniques is that the freedom of movement of the tools is limited by their size and by the manoeuvrability of the robotic arm. Complex hollow structures, or structures filled with three-dimensional grids cannot be manufactured using subtractive production techniques. AM techniques do not have these constraints. In a layer-wise AM process, a three-dimensional design is sliced into vertically stacked layers. These layers are produced and fused together in the same production step. This work is focussed on the analysis of AM metals, especially on the analysis of Stainless Steel (SS) American Iron and Steel Institute (AISI) 316L produced by the AM process PBF-LB/M. In the following this is shorted to PBF-LB/M/316L.

1.2 Laser Powder Bed Fusion

PBF-LB/M is a AM technique that creates objects from 3D models by melting powdered feedstock material. As depicted in fig. 1.1, a PBF-LB/M machine schematically consists of the following parts: a build platform of adjustable height, a feedstock powder reservoir, a rake to apply new layers of powder, a laser to melt the powder, and a system of guiding mirrors to guide the laser to any position on the build platform [2].

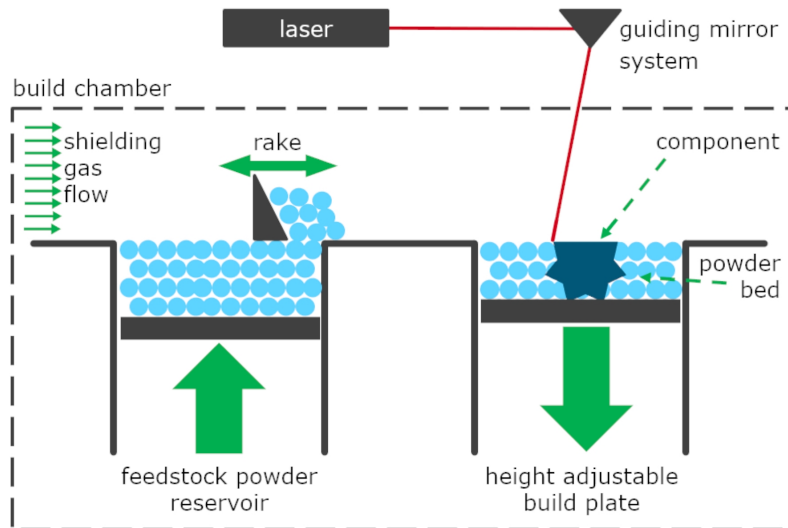


Fig. 1.1: Principle sketch of a PBF-LB/M system

To build objects using the PBF-LB/M technique a 3D model of the object has to be sliced into layers of a thickness of several tens of micrometres. To create a solid area within the sliced shape of the object, a scanning strategy has to be applied that fully illuminates the area. Depending on the machine parameter applied, the laser can melt tracks of the feedstock powder that are between tens and a few hundred micrometres wide. To illuminate a sliced area of several centimetres many laser tracks have to be placed side by side. The size and orientation of these scan tracks is defined by the scan strategy. There are several different scan strategies, which—depending on the used feedstock material—can influence the material properties of the produced components in many ways. In the following sequence plan a generic PBF-LB/M build process is described. Typically, the build process consists of a repetition of the following steps until the object construction is finished:

1. The build platform moves down by a certain amount of micrometres. This will define the thickness of the layer.

2. The rake applies feedstock powder onto the lowered build platform to fill the layer.
3. The laser illuminates sections of the build platform defined by the shape of the slice and the applied scan strategy.
4. Steps 1-3 are repeated until all slices are illuminated.

Among the various AM techniques for the manufacturing of metallic objects the PBF-LB/M process has a main advantage: The process can produce net-shaped objects including high-resolution features (e.g., a grid of struts). A disadvantage of PBF-LB/M compared to other AM techniques for metals is the limited size of the manufactured objects. Commercial PBF-LB/M systems equipped with one laser are usually equipped with a build chamber sized less than 100l [4], and subsequently, can produce objects smaller than this.

1.3 State of the Art

In recent years, PBF-LB/M has evolved from a technique for rapid prototyping to a mature production process in several industries, such as automotive, aerospace and rail [5, 6]. Due to increasing interest in this technology there is a need of detailed understanding of the influence of the PBF-LB/M process to assess the service life of components produced by PBF-LB/M. Especially, if these components are supposed to be used in critical applications concerning loads and temperature it needs to be understood why the PBF-LB/M material's response to external loads differs from the conventionally produced material [7, 8]. The analysis of metals manufactured by PBF-LB/M has been a topic in material science for the last decades with the first Wohlers report on the state of the then-called Rapid Prototyping dating back to 1996 [9]. For objects produced by PBF-LB/M three inherent features to the production process must be addressed when assessing the service life of the objects:

1. *Unusual* microstructures depending on process parameters [10, 11] (see fig. 1.2)
2. Void formation during the build process [12]
3. Build up of internal stresses during the build job that remain as RS in the object after production [8, 13, 14]

Void formation and Residual Stress formation will be addressed in the scope of this thesis, and will be described in detail in the following sections.

Studies of PBF-LB/M steels have revealed that they exhibit significantly different microstructures in the as-built condition compared to conventionally manufactured variants of the same alloy (cast, wrought) [15, 16, 17, 18]. PBF-LB/M steels consist of a non-isotropic columnar grain morphology [5, 15, 16, 17] which is determined by the process parameters used. For instance, Mohr et al. [19] have shown that even slight changes to the process parameters such as a variation of the ILT result in a variation of grain orientations in the columnar microstructure.

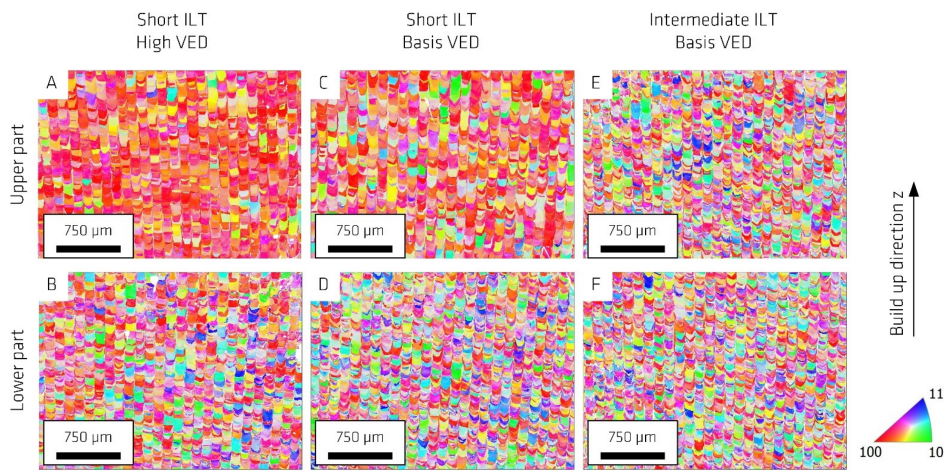


Fig. 1.2: Orientation maps of PBF-LB/M/316L manufactured at different ILT [19] showing columnar grain orientation

1.3.1 Void Formation Mechanisms in PBF-LB/M/316L

Void formation in welding has been a topic to research for decades [20, 21]. There are many process parameters of the build whose interplay can cause void formation in PBF-LB/M. Here the focus will be set on the formation mechanisms of two major types of voids found in PBF-LB/M objects: LoF voids and keyhole pores. The formation of the two sets of voids can be understood through a common quantity in PBF-LB/M, the VED. The VED is defined by:

$$VED = \frac{P}{v h t} \quad (1.1)$$

where P is the laser power, v is the scan speed, h is the hatching distance, and t is the layer thickness. For many metals used in PBF-LB/M, machine manufacturers provide a set of parameters that should lead to the least amount of voids in a produced

object. Significant changes from the VED (calculated from the manufacturer's process parameters) lead to void formation. An increased VED causes keyhole pores, whereas an reduced VED causes LoF voids.

Keyhole Pores Keyhole pores are an ever-present class of voids in PBF-LB/M [12], which form when an excessive amount of energy is introduced to the melt pool by the laser [22]. As described by King et al. [23]: “In keyhole-mode laser welding, the power density of the laser beam is sufficient to cause evaporation of the metal and formation of plasma. Metal evaporation causes the development of a vapour cavity that enhances the laser absorption.” Therefore, the energy of the laser beam is not absorbed by powder particles at the surface. Instead due to the keyhole-shaped wedge formed by evaporating powder, the laser can reach deeper laying powder particles [24]. Fast cooling rates in PBF-LB/M caused by the scan speed and very localised heating from the laser in combination with uneven sized powder particles in the powder bed make this an unstable phenomenon. Hence, if the keyhole collapses inert shielding gas can be trapped in pores at the bottom of the keyhole-shaped wedge [25]. The penetration of the laser is not limited to layers of unmolten powder particles but can also occur in already void-free solidified material. If the VED of the build process is high enough, the melt pool can entrap keyhole pores in addition to re-melting the existing solidified material [26]. Since keyhole pores consist of entrapped gas, their shape is mainly spherical. Since they form at the bottom of the keyhole-shaped wedge, they are not found close to the built objects top surface.

Lack-of-Fusion Voids LoF occurs when the melt pool widths of neighbouring scan tracks do not overlap sufficiently as depicted in fig. 1.3. Most of the reasons that cause the lack of overlap are described by equation 1.1. A sufficient change to any of the quantities that lead to a decrease in the VED might cause LoF void formation. If the layer thickness exceeds the depth of the melt pool, insufficient overlap can occur. Also, a reduction in laser power or increased scan speed can result in narrower track width, which could cause insufficient overlap. An increase in the hatching distance can also cause insufficient overlap. As depicted in the schematic drawing in fig. 1.3b the resulting voids are of irregular shape. Due to their irregular shape, LoF voids much more likely serve as crack initiation zones than spherical gas pores, especially when the loading direction is perpendicular to the the orientation of the LoF voids [11].

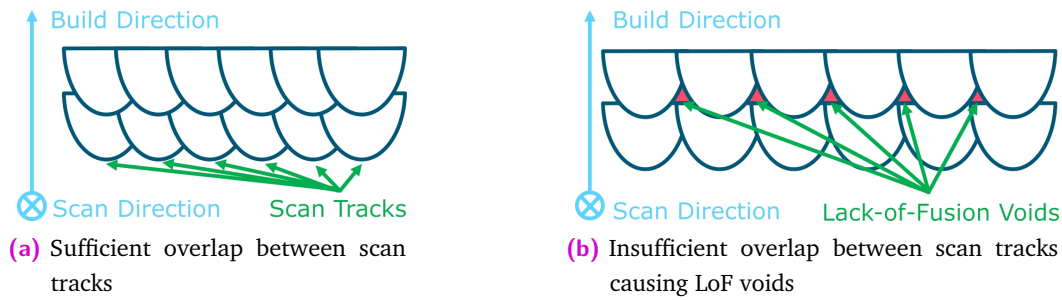


Fig. 1.3: General illustration of LoF void formation

Void formation is inherent to the PBF-LB/M production process. Hojjatzadeh et al. [27] listed four typical mechanisms that can lead to void formation in PBF-LB/M: “pore transfer from feedstock powder [28], instability of depression zone during printing process [25], vaporization of volatile elements [29], gas precipitation [30]”. Hence, it is essential to distinguish voids from potential defects. On-line monitoring of the PBF-LB/M process has been studied to predict whether void formation will result in formation of potential defects within the finished part [26, 31, 32, 33, 34, 35, 36, 37]. Among the on-line monitoring techniques, thermography enables temperature changes of the apparent surface temperature to be monitored without the need of complex sensors to be installed in the build chamber [26, 33]. Thermal irregularities during the build process can be correlated to void [26, 38] and RS formation [39]. Therefore, based on these inherent aspects of the PBF-LB/M process, it is necessary to understand how the laser interacts with layers of solidified material and with layers of unmolten powder. Recent studies have revealed that the laser melts subjacent layers of material in addition to the current surface layer [5, 40]. As described in chapter 1.2, this effect is needed to provide a strong bonding between the layers and to prevent LoF voids [41, 42]. Several studies in this field have reported results on the interaction between melt pool and powder from simulations [25, 43, 44] and experiments [45, 46]. They have reported that the laser energy via different stages of dissipation can melt powder particles beyond the current top layer.

1.3.2 Residual Stress Formation Mechanisms in PBF-LB/M/316L

The process of laser beam melting inherently induces stresses in components produced by PBF-LB/M [8, 13]. Such stresses can have implications on service life. These stresses remain in the component after the process and without the application of external loads, and are called RS [47]. Mercelis and Kruth [13] have

described two interlinked mechanisms that form the RS distribution in PBF-LB/M: the Temperature Gradient Mechanism (TGM), and the cool down phase, which results in a Constrained Solidification Shrinkage Mechanism (CSSM):

Constrained Solidification Shrinkage Mechanism During solidification the melt bonds with either the underlying or adjacent solidified material. The solidification leads to shrinkage of the previously molten metal. Due to the bonding to the surrounding solidified material, this shrinkage is restricted, placing the solidifying material into tensile stress while the surrounding and underlying already solidified material is placed under compression. The PBF-LB/M process is applied layer upon layer. Therefore, the solidification of every layer (and re-solidification of the underlying material that melts) induces compressive stresses into the subjacent layers, increasing the amount of compressive stresses in the built component. These compressive stresses in the subjacent layers are balanced by tensile stresses in the surface region due to stress equilibrium and remain in the part after the PBF-LB/M production process is finished.

Temperature Gradient Mechanism The material is heated up locally during the laser illumination. This heated material would expand but its expansion is constrained by the cooler surrounding solidified material. When the thermal stresses from this constrained expansion reach the yield strength of the material, local plastic deformation occurs. When the laser moves on, the material cools down and the plastically deformed material shrinks. As mentioned above this shrinkage is restricted by the surrounding solidified material. Therefore, further compressive stress are introduced into the the subjacent layers with tensile stress in the region which was locally heated. It should be noted that the TGM does not require melting, and therefore, is mainly present in the layers below the currently illuminated surface.

The two mechanisms are interlinked and their combined effect on RS formation has been studied in recent years [48, 49, 50, 51]. As mentioned before, the RS distribution of PBF-LB/M parts shows tensile stresses near the surface [52]. Tensile surface stresses are usually unwanted for industrial components, since these stresses can facilitate crack initiation [14, 53]. Therefore, different attempts to reduce the magnitude of RS in PBF-LB/M by alternating the build process parameters have been studied. Wang et al. [50] have altered the length of scan tracks. They found that a reduction of the length of the scan tracks could reduce the residual stresses in long bars of as-built PBF-LB/M/316L. This RS reduction can be associated to the CSSM. Roehling et al. [51] reported reduced RS values in bridge-shaped as-built

PBF-LB/M/316L specimens, when each illuminated layer was heated to 625 °C after solidification. This decreased the amount of RS of their specimens. They also reported that reaching the temperature of 625 °C had a greater effect than the dwell time at this temperature. Here, the thermal history of the specimen was altered, employing the TGM to reduce the RS levels. In both studies, RS could be successfully reduced, although different RS forming mechanisms were exploited. So far, there is still an uncertainty on the quantitative influence that the two mechanisms have on the shape and magnitude of the resulting RS distribution.

1.3.3 Damage Formation in Quasi-Static Loaded PBF-LB/M/316L

To enable the prediction of the service life of PBF-LB/M parts and components, they must be studied under the application of external loads. The material used in this thesis is AISI 316L. AISI 316L is widely used in industry [5, 6]. Its PBF-LB/M variants have been reported to be feature higher strength than conventionally made 316L [54], while possessing good ductility [17, 55, 56]. The tensile properties of AISI 316L have been a topic for research during the recent years [57, 58, 59]. Still, there is limited research on the creep behaviour of AISI 316L. Yu et al. [60] have studied the creep behaviour of AISI 316L specimens produced using a meandering stripe scan strategy. They have studied the impact of scan speed variation on the creep behaviour of small plates which were tested in a small punch creep testing rig. They concluded that the increased porosity cause by excessive scan speeds scan speeds results in inferior creep resistance. This result is very comprehensible if one brings to the mind that LoF voids are irregular shaped and have sharp edges which can easily serve as crack initiation zones. Williams et al. [18] have studied creep behaviour in AISI 316L specimens built using a *chessboard* scan strategy combined with 67° rotation of the chessboard's orientation for each layer. The combination of the two features of the scan strategy lead to a microstructure of elongated grains parallel to the build direction. The used 67° rotation scan strategy is known to reduce porosity in PBF-LB/M/316L [38, 61]. Herzog et al. [62] postulated in 2016 that a porosity value in PBF-LB/M/316L of less than 0.5 % (*i.e.*, a density value larger than 99.5 %) should be achieved by parameter optimisation of the PBF-LB/M process. In more recent studies of PBF-LB/M/316L a porosity value of less than 0.1 % was achieved [17, 63]. Therefore, the observed porosity by Williams et al. [18] of 0.4 % appears to be larger than expected. Creep describes the propensity of a material to deform plastically under mechanical stresses at elevated temperatures [64]. Creep occurs under long term exposure to stresses that usually are below the yield strength of the material. To predict the long term stability of PBF-LB/M components in

operating conditions (*i.e.*, at high temperatures), knowledge about their creep behaviour is essential.

1.4 Motivation & Aims

In this work void formation in AISI 316L is studied using XCT analysis of specimens produced using several different process parameters. XCT provides a three-dimensional analysis of objects (the technique is described in a detailed way in chapter 2.1). It literally adds a new dimension to the meaningfulness of the analysis compared to 2D methods such as optical microscopy on metallurgic cuts when it comes to material with non-isotropic microstructure [65]. The analysis of the 3D XCT data enables the understanding of the impact of process parameters on void formation at specimen size levels. The initial void distribution is studied in creep and tensile specimens produced using process parameters which were optimised by the PBF-LB/M machine manufacturer for PBF-LB/M/316L. Also, keyhole pores and LoF voids are studied to understand their formation mechanisms. The XCT results of this work are correlated to thermography data [26] obtained during the build job. This enables the analysis of how irregularities observed in the thermographic data result in actual voids formed in the final component. Several studies in this field have reported results on the interaction between melt pool and powder from simulations [25, 43, 44] and experiments [45, 46]. Based on their results this work aims to evaluate how the laser illumination of superjacent layers affects the formation of voids in underlying layers. Void creation or healing in these underlying layers cannot be predicted from the analysis of the on-line monitoring signals directly [26]. Therefore, this work studies the ability of the laser to melt different multiples of the optimised thickness of powder layers. The mechanisms of void formation in these thicker powder layers are derived from the analysis of XCT data.

The second aspect considered within this thesis on the inherent features of PBF-LB/M is the formation of RS in PBF-LB/M/316L. An improved understanding of RS formation is important to improve the knowledge of the effects of changes of certain process parameters on the RS distribution. Based on the two stress generation mechanisms described by Mercelis and Kruth [13] in section 1.3.2, this work aims to unravel the interlinked influence of the two mechanism onto RS formation by using stress analysis based on neutron diffraction. Identifying the magnitude of each mechanism will enable designers of PBF-LB/M/316L parts to improve process parameters to achieve the desired RS distribution of their parts. The RS results obtained by neutron diffraction are compared to thermographic data [39] obtained

during the build. The analysis of the thermal history of specimens enables the understanding of the TGM's influence on the RS distribution in the as-built part. In return, features of the RS distribution that cannot be assigned to the thermal history must be caused by CSSM, or to paraphrase Sir Arthur Conan Doyle's Sherlock Holmes [66]: When you have eliminated all which is TGM, then whatever remains, however improbable, must be the result of CSSM.

The third aspect considered within this thesis on the inherent features of PBF-LB/M is the damage formation in PBF-LB/M/316L under external loading conditions. Creep damage formation at elevated temperatures is discussed in this work. Only a few studies address creep behaviour of PBF-LB/M/316L. Yu et al. [60] and Williams et al. [18] emphasise how the the creep behaviour of PBF-LB/M/316L depends on the used build parameters. Ávila et al. [67] have presented a detailed comparison of creep deformation in PBF-LB/M/316L and hot rolled AISI SS 316L. Based on the work by Ávila et al. [67] I non-destructively studied the evolution of damage in creep specimens of PBF-LB/M/316L. Creep specimens of PBF-LB/M/316L were analysed by XCT at different stages of creep testing to study the formation mechanisms of creep damage. XCT results are compared to the microstructure of PBF-LB/M/316L to reveal the formation mechanisms of creep damage. These results are compared to the XCT data of broken tensile specimens to further increase the understanding of damage formation mechanisms in this PBF-LB/M/316L. An increased understanding of how PBF-LB/M/316L microstructures determine the formation of damage in the material becomes relevant when assessing these materials for the use in industrial applications.

In general, this work aims to combine results from fundamental research of void and RS formation and their repercussions on tensile and creep behaviour.

1.5 Embedding of this Thesis into Existing Research Projects

This thesis was embedded into two interlinked in-house projects on additive manufacturing of metals at the Bundesanstalt für Materialforschung und -prüfung (Federal Institute for Materials Research and Testing, Berlin, Germany) (BAM). The scope of the project *ProMoAM* (Method Development for Process Monitoring in Additive Manufacturing) was the development of on-line sensor systems to monitor the production of metallic AM parts and components at the three AM techniques available at BAM (PBF-LB/M, Direct Energy Deposition using a Laser Beam (DED-LB/M), Wire Arc

Additive Manufacturing (DED-Arc)) [26, 68, 69]. Experts from different divisions at BAM joined for this project to develop, build and benchmark non-destructive monitoring techniques to discover faults in AM components during the build job. My task in this project was to assess the quality of the as-built specimens by XCT to provide a *ground truth* of the void distribution within the specimens. Results from on-line monitoring were compared to the *ground truth* in order to obtain threshold values of the on-line signals that resulted into voids within the final part. The results of the XCT analysis was mainly used to assess the quality of thermographic measurements that were obtained during the build process. Thermography is based on analysing the apparent radiated heat of the current top surface during the build process by thermographic cameras [26, 33].

The project *AGIL* (Microstructure Development in Additively Produced Metallic Components: from Powder to Mechanical Failure) aimed at assessing the quality of AM parts and their feedstock material at different stages of their service life. Experts from different divisions at BAM joined this project to analyse the quality specimens using destructive and non-destructive techniques. The work packages of this project consist of the analysis of the feedstock material for PBF-LB/M [70], the microstructure of as-built PBF-LB/M and DED-LB/M specimens, the microstructure of specimens after a stress relieving heat treatment, and before in-between and after mechanical testing. The assessment of the mechanical properties of specimens using tensile, creep and single-edge-notch-bending tests was also part of the *AGIL* project [67, 71]. My task within the project was to characterise specimens at different stages of their service life regarding their internal void spatial distribution (using XCT) as well as their residual stress fields. Due to the close connection between *ProMoAM* and *AGIL* results from thermography were used for the interpretation of XCT and ND results.

Theoretical Background

” *As with most of life’s problems, this one can be solved by a box of pure radiation.*

— **Andy Weir**
(The Martian)

In this thesis the analysis of specimens is based on results from XCT and RS determination using neutrons. This chapter describes the theoretical background of the two techniques.

2.1 X-ray Computed Tomography

XCT started in 1973 when the Briton Godfrey N. Hounsfield presented the first medical XCT system [72]. Industrial XCT derived from it using higher voltage X-ray sources since radiation doses do not have to be taken into account in contrast to medical XCT. High resolution inspection of components was enabled by the invention of micro-focus X-ray sources in combination with algorithms that enable reconstructing volumes with improved sharpness of the object. Nowadays, industrial XCT using micro-focus X-ray sources is a well established Non-Destructive Testing (NDT) technique to quantitatively inspect parts and components in industry and material science [73]. Micro-focus XCT-scanners were used to acquire all XCT-data of this thesis.

This chapter is based on the book *Einführung in die Computertomographie* by Thorsten M. Buzug [74] and describes the generation of X-rays, their interaction with the scanned object’s material, the way they are recorded, and the reconstruction into a 3D representation of the object.

2.1.1 Working Principle of Laboratory XCT

In industrial laboratory XCT an object is placed on a rotation stage of an manipulator system that is placed between an X-ray source and a 2D flat panel detector (see fig. 2.1).

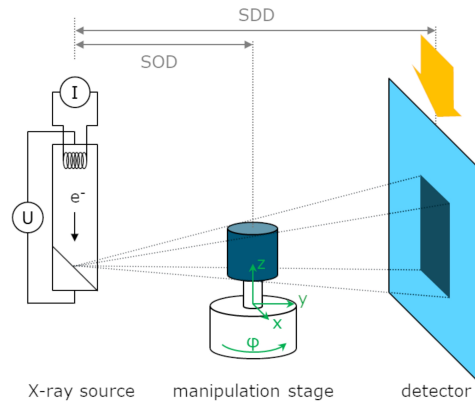


Fig. 2.1: Principle sketch of a laboratory XCT set-up

During a stepwise rotation of the object, X-ray radiographs (so-called projections) are acquired. These projections are reconstructed into a 3D volume. The most common method currently used is the Filtered Back-Projection (FBP) (see fig. 2.2). The magnification of these cone-beam based laboratory XCT scanners is defined by the ratio of the Source-Object Distance (SOD) and Source-Detector Distance (SDD) (see fig. 2.1).

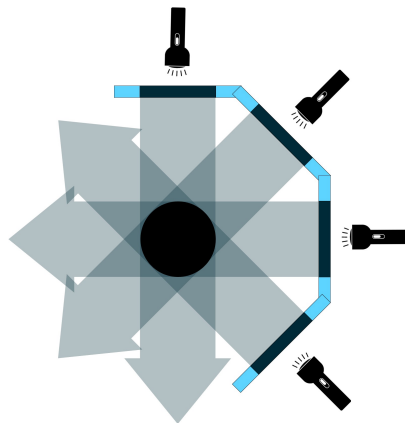


Fig. 2.2: Basic principle of back-projections: All acquired projections are positioned around a virtual centre. The projections are projected to this virtual centre. The point of view of the projections shown in this sketch is marked by a yellow arrow in fig. 2.1

2.1.2 X-ray Radiation

In 1895 Wilhelm Conrad Röntgen discovered a new type of radiation which was able to penetrate materials non-transparent to visible light [75, 76, 77]. He named them X-rays and was awarded the Nobel price in 1901 for his discovery. In the following only the physical relations concerning computed tomography will be discussed.

Generation of X-rays

In a X-ray source of a laboratory XCT system a filament is heated to generate electrons which are accelerated in a vacuum by a electric field. The electric field is generated by a acceleration voltage U between the filament (*i.e.*, cathode) and a metal target (*i.e.*, anode) as depicted in fig. 2.1. When these accelerated electrons hit the anode material, they decelerate due to interaction with the target's atoms. The energy loss of the electrons usually takes place in multiple events, resulting in the generation of a continuous spectrum of electro-magnetic waves (*i.e.*, *bremstrahlung*) in the spectral range of 10^{-8} m to 10^{-13} m. These waves are called X-rays.

The energy of the emitted waves is related to the velocity v of the electron, which is determined by the accelerating voltage U set between anode and cathode (see fig. 2.1). The velocity of an electron can be derived from the energy conservation equation:

$$eU = \frac{1}{2} m_e v^2 \quad (2.1)$$

where e is the electric charge of an electron, and m_e is the mass of the electron. It can occur that the entire energy of an accelerated electron eU being transformed into a single photon. The maximum energy E such a photon can be determined the shortest wavelength λ of the radiation, that can be derived from the following equation:

$$E = eU = h \frac{c}{\lambda} \quad (2.2)$$

where h is the Planck constant, and c the speed of light. Hence, the shortest X-ray wavelength is given by:

$$\lambda = \frac{12.398}{U} \quad (2.3)$$

where U is in kilovolts, and λ is in Angstroms ($1 \text{ \AA} = 0.1 \text{ nm}$). Therefore, the higher the accelerating voltages the shorter the minimum wavelengths of the generated X-rays.

The continuous spectrum is superimposed by a line spectrum which is created by the interaction of fast electrons with electrons of the inner shells of the atoms of the

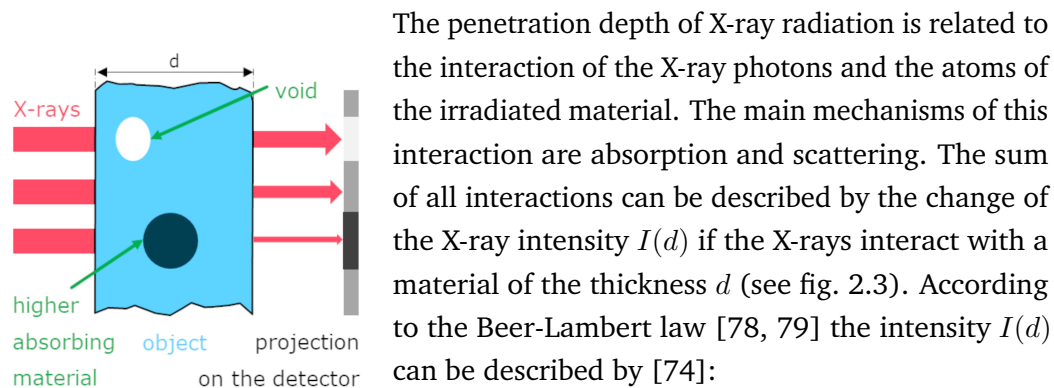
anode material. This line spectrum is called *characteristic radiation* and consists of discrete peaks, whose wavelength solely depends on the anode material.

If electrons of the K -shell of the target material are ejected of the atom by a collision with a fast electron, electrons from higher energy level shells fill the vacant position in the K -shell. During this process the energy difference between shells is emitted as X-ray photon. Due to the discrete energy difference between the shells, these photons have discrete wavelengths. These wavelengths form sharp lines in the continuous X-ray spectrum which are characteristic for the material used in the anode. The position of the K -lines in the spectrum can be derived from Moseley's law as defined in [74]:

$$\lambda = \frac{hc}{E_n - E_l} = \frac{hc}{13.6 \text{ eV} (Z - 1)^2 (1 - 1/n^2)} \quad (2.4)$$

whereas Z defines the effective nuclear charge of an atom and n its principal quantum number.

X-ray–Material–Interaction



The penetration depth of X-ray radiation is related to the interaction of the X-ray photons and the atoms of the irradiated material. The main mechanisms of this interaction are absorption and scattering. The sum of all interactions can be described by the change of the X-ray intensity $I(d)$ if the X-rays interact with a material of the thickness d (see fig. 2.3). According to the Beer-Lambert law [78, 79] the intensity $I(d)$ can be described by [74]:

Fig. 2.3: X-ray absorption

$$I(d) = I_0 e^{-\int_0^d \mu(E,x) dx} \quad (2.5)$$

The attenuation coefficient $\mu(E, x)$ is described by the sum of the absorption coefficient $\mu_a(E, x)$ and the scattering coefficient $\mu_s(E, x)$. It should be noted that the Beer-Lambert law only hold for a pencil beam geometry without scattered radiation. Absorption and scattering are caused by one of the following four interactions:

Rayleigh Scattering Rayleigh scattering occurs if the the wavelength of the X-ray radiation exceeds the atom diameter of the irradiated material. In this case the X-ray radiation interacts with the whole atom and cause oscillation of the

electrons in the atom. Rayleigh scattering is caused by X-ray photons which have an energy of less than 20 keV.

Compton Effect Elastic scattering (*i.e.*, Compton effect) occurs if the energy of the incoming X-ray photon exceeds the binding energy of the atom's electrons. If a photon hits an electron its flight path will be changed and some of its energy will be absorbed by the hit electron. Due to change of the flight path these scattered X-ray photon might hit the detector at an unknown position, and therefore increase the noise level of the acquired image. Mainly, Compton scattering occurs for X-rays photons of an energy level of 100 keV up to 1 MeV.

Photoelectric Effect The photoelectric effect ionises the atom. The whole energy of the X-ray photon is absorbed by the an electron of the irradiated material. Since the photoelectric effect mainly involves electrons of the inner atom hull, it occurs more often for heavier atoms. The full absorption of the emitted X-ray photons is the main attenuation mechanism for X-ray radiation. It mainly occurs for X-rays photons of an energy level of less than 100 keV.

Pair Production At very high energy levels of X-ray photons (above 1.022 MeV) the photons interact with the electric field of the hit atom. The energy of the incoming X-ray photon is fully converted into the creation of an electron-positron-pair.

Detection of X-rays in Laboratory XCT

In laboratory XCT systems usually flat panel detectors are used. Many detectors of computed tomography systems are based on the same design: a scintillator layer that converts X-ray radiation into visible light, followed by a photo diode layer that converts visible light into current, and a substrate layer that provides electrical and mechanical infrastructure [80]. A detector is usually divided into several blocks of detector elements to decrease the read-out time by parallelisation. Each element consists of a certain number of square shaped elements (called pixel) in the size range of about $100\ \mu\text{m}$. To prevent stray radiation (see sec. 2.1.2) from being distributed between neighbouring pixel of a detector element anti-scatter grids are used as collimator in front of the detector elements [74, 80]. To prevent negative read-out values of the detector elements manufacturers calibrate their systems in a way that every pixel provides a ground signal even without excitation from X-ray photons. A flat field correction of the acquired projections needs to be performed since this ground signal is not uniform through the whole panel. The same is valid for the ability to convert X-ray photons into current. Due to fluctuations

in production and also through ageing, the ability to convert X-ray photons into current changes between the detector elements. Therefore, the acquired projections will also be bright field corrected to minimize the influence of the detector on the image quality of the projections.

2.1.3 Image Reconstruction in Laboratory XCT

The goal of XCT is to reconstruct a 3D representation from a number of projections acquired at different rotation angles of an object (see fig. 2.1). If these projections are positioned around a virtual centre according to their rotation angle the back-projection of these images into this virtual centre would create a 3D representation of the scanned object (see fig. 2.2). For simplicity reasons the following description assumes a two dimensional problem (*i.e.*, a horizontal 2D slice of the 3D volume). The back projection helps solving an inverse problem: the real object function $f(x, y)$ is needed but one only can record the projections of the object $p(\xi)$. The foundation to solve this inverse problem was already found by the bohemian mathematician Johann Radon in 1917 [81]. However, it could be solved for the first time in the 2nd half of the 20th century when the invention of computers enabled the solve of his complex equations. Each pixel of an acquired projection represents the integral of the X-ray attenuation coefficient μ along a line from source to detector. Inhomogeneities of the μ along this line (*i.e.*, attenuation of different materials and/or thicknesses) prevent the problem to be solved by a simple inversion. But the spatial distribution of these attenuation coefficients will provide information about the internal structure of the object. Along a line γ the Radon transform \mathcal{R} is defined as:

$$p_{\gamma}(\xi) = \mathcal{R}(\gamma) = \int_{\gamma} f(x, y) ds \quad (2.6)$$

The visualisation of the Radon Transform is called a sinogram. It contains the integral attenuation values of a detector pixel for all angles of the acquisition. The Radon Transform assumes continuous physical signals, whereas the XCT systems discretised these values. Therefore, reconstructing an object using the inverse Radon Transform on a discrete sinogram is very difficult. Hence, the acquired discretised sinograms are transformed into the Fourier space using the Fourier-Slice-Theorem. The Fourier-Slice-Theorem states that the 1D Fourier transform of the Radon transform $\mathcal{F}_1\{p(\xi)\}$ is equal to the the sliced line through the origin of the Fourier space of the 2D Fourier transform of the function $\mathcal{F}_2\{f(x, y)\}$. Reconstructing the object from the Fourier space using the inverse Fourier Transform is much easier since the Fourier Transform is well suited for discretised values (see fig. 2.4).

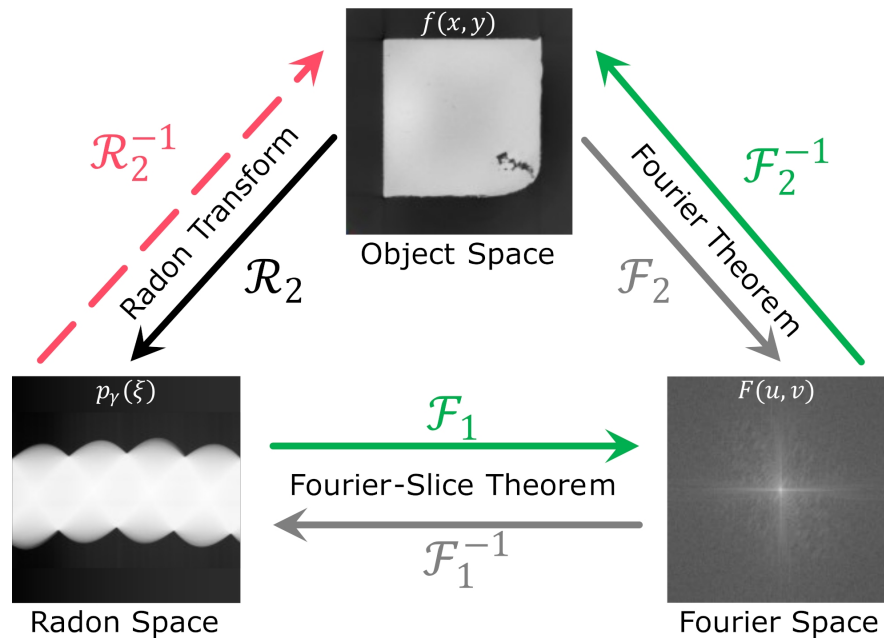


Fig. 2.4: The connection between object space, Radon space (i.e., sinogram) and Fourier space.

In 1984 Feldkamp, Davis and Kress presented a FBP method to reconstruct projection data from 2D detectors [82]. The simple back projection algorithm described above leads to blurred reconstructed objects since every point of the object is spatially smeared. To prevent this the projections $p(\xi)$ must be filtered using a high-pass filter $g(\xi)$. Mathematically this is realised by a convolution (i.e., $p * g$) of p and g . In the Fourier domain the convolution can be realised by the multiplication of the Fourier transform of p and g . In technical implementations also a low-pass filter in form of a window function is applied to suppress high frequencies in the Fourier domain which will reduce the noise in the reconstructed volume.

Remark In case of the assumed 2D slice to be reconstructed the FBP algorithm reconstructs the object correctly. When applied on a 3D volume obtained from a cone-beam geometry, the FBP algorithm assumes the cone-beam to be a set of fan-beams. This simplification leads to a small soft focus in the reconstructed volume for every slice which is not the center slice of the volume.

Image Artefacts and Image Quality

The quality of a reconstructed XCT image in terms of noise, sharpness and resolution can be influenced by the chosen settings of the XCT systems as well as by artefacts

of the 3D reconstruction of the FBP. Some typical effects and artefacts that influence the image quality are described in this section.

Signal-to-Noise Ratio The main influence of image quality is the Signal-to-Noise Ratio (SNR).

$$SNR = \frac{\text{signal level}}{\text{noise level}} = \frac{\mu}{\sigma} \quad (2.7)$$

where μ denote the mean value and σ the standard deviation of the signal. Improvements of the SNR can be achieved by an increase of the number of X-ray photons measured in transmission. This increase can be realized by either increasing the acquisition time per projection and/or by increasing the current of the X-ray tube. As described in 2.1.2 X-ray radiation are emitted in a continuous spectrum. Therefore, an increase in the current of an X-ray source will increase the number of photons in the full spectral range. Since the number of counts per detector element that can be processed before read-out is limited (65 536 counts for 16 bit detectors and 16 384 counts for 14 bit detectors) it might be necessary to pre-filter the low energy photons to prevent saturation of the detector element by the photons of the free beam. Usually, metal filters are applied to the escape window of the X-ray tube to block low energy photons. The downside of this approach is that not only low energy photons are blocked by the filter but photons of all energy ranges. Therefore, the overall counting time of an acquisition should be increased to compensate the loss of photons. If increasing the acquisition time cannot be applied due to saturation, several shorter timed acquisitions of the same projections can be averaged to improve the SNR.

Beam Hardening Artefacts as described in chapter 2.1.2 X-ray radiation is emitted in an wide spectral range. During transmission of an object, X-ray photons of lower energy levels are more likely to be absorbed or scattered away from the detector than photons of higher energy (see chapter 2.1.2). This results in a shift of the spectral range toward higher energy levels. Current X-ray detectors are not energy dispersive, that means they cannot differentiate photons of different energy. Since the detector elements do not differentiate the energy of the counted photons, the increased absorption of soft photons can lead to lower grey values in center of the reconstructed volumes of mono-material objects or to streak artefacts around the objects of heavier materials in a multi-material object. To prevent beam hardening artefacts the soft photons could be filtered from the incoming beam by a metal pre-filter. Also, most reconstruction algorithms provide a mathematical solution to decrease the influence of beam hardening in the reconstructed image.

Blurring Due to Focal Spot Size In this work laboratory XCT scanners were used. The focal spot size of the X-ray tubes varies between the used scanners and also depends on the applied power to the X-ray source. Since the focal spot is not a point source as depicted in fig. 2.1 blurring effects could occur at the borders of the images as depicted in fig. 2.5. This blurring usually is in the range of the focal spot size and, therefore, has an larger impact at higher magnifications. Hence, the yielded minimum pixel size of the projections should be larger than the focal spot size of the used parameters of the X-ray source.

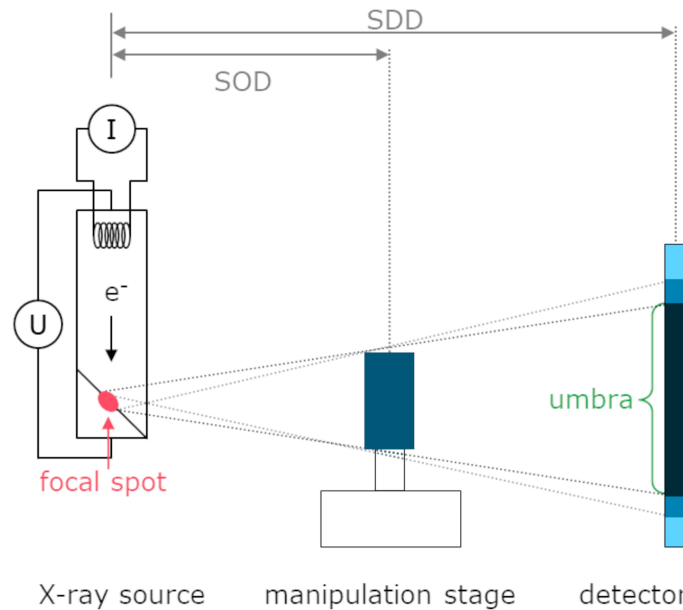


Fig. 2.5: Blurring of the projection due to deviation of the physical focal spot size from a ideal point source

Ring Artefacts During the service life of a detector some of its pixels might fail. Instead of providing the count of all received photons of a projection they return a constant value. Since the reconstruction of the same pixel in the projections forms a ring in the 3D image, a constant value for this pixel will be reconstructed as a ring of this constant value. In the sinogram these pixels of constant value appear as a straight line. Therefore, replacing the information of this pixel with the average of its neighbours is usually performed by the acquisition software. Hence, the position of dead detector pixels must be known prior to the reconstruction.

2.1.4 Synchrotron Computed Tomography

SXCT results presented in this work were conducted at the beam line *BAMline* at the Berlin synchrotron BESSY II. Therefore, the capabilities of BESSY II are referred to in this section.

X-Rays can also be generated with relativistic electrons which are being deflected by a magnetic field. This is exploited in an electron storage ring, also called synchrotron. The main advantage of synchrotron produced X-rays compared to a laboratory X-ray source is the photon flux. An up to 1000 times larger photon flux (*i.e.*, photons/second [83]) than a conventional X-ray tube enables scans at high resolutions (voxel size $< 1\ \mu\text{m}$) without the need of significantly increased scanning times [84]. A second advantage is the parallelism of the beam. On the one hand, it enables the use of simpler reconstruction algorithms than cone-beam based laboratory XCT. On the other hand, reconstruction artefacts that are caused by the cone-beam do obviously not occur. The set-up of a SXCT beamline differs significantly from laboratory XCT equipment. Instead of electrons being accelerated between an anode and cathode, a storage ring, where electrons are kept at a constant kinetic energy level, is used. A combination of a linear accelerator and a smaller booster synchrotron is used to accelerate the electrons up to an energy in the range of 10^{12} eV (At BESSY II energies of up to 1.7×10^9 eV can be achieved). These high energy electrons are injected into a storage ring where they are forced into a circular flight path.

The flight path is controlled by the bending and focussing magnets. Wigglers, undulators and wavelength shifter are used to generate X-Rays. The SXCT beam line *BAMline* at BESSY II is located after a 7 T wavelength shifter. If the electrons' flight path is changed, bremsstrahlung is emitted in the form of X-rays. The energy of these X-rays can be filtered to a specific energy by a set of monochromators. The large distance between the bending and focussing magnets and the beam lines (at *BAMline* this distance is 35 m) results in an almost parallel beam. Due to the assumed parallel beam there is almost no geometric magnification of the projections as compared to a laboratory XCT set-up. At a SXCT beamline the magnification of the projected object is performed by a set of optical lenses placed in front a Charge-Coupled Device (CCD) screen. Therefore, X-rays have to be transformed into visible light using a scintillator material. At *BAMline* the scintillator consists of cadmium tungstate (CdWO_4). A general sketch describing a SXCT beamline's set-up is depicted in fig. 2.6. Due to the use of a parallel beam the FBP reconstruction algorithm is correct for every slice, instead of just the center slice for laboratory XCT systems. The parallel beam also enables the 360° rotation of a cone beam laboratory X-ray system to be reduced to a

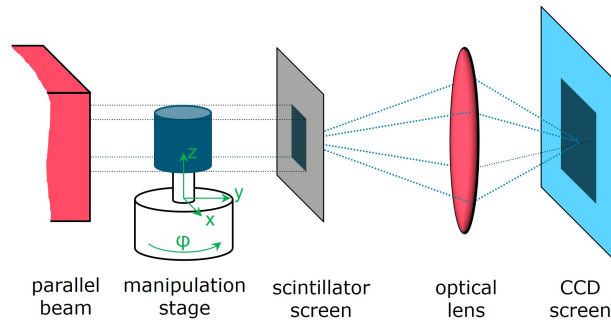


Fig. 2.6: General sketch of a SXCT set-up: The parallel X-Ray beam transmits the sample and is converted into visible light by the scintillator. The visible light is imaged onto the CCD-screen after magnification by an optical lens.

180° rotation without a loss of information. Energy selection at *BAMline* is performed by a double multilayer monochromator. The first mirror is used to monochromatise the energy spectrum by diffraction. The second mirror is used to direct it towards the beam line. Typical laboratory XCT image artefacts (*i.e.*, beam hardening or the influence of the focal spot size) do not occur with a monochromatic beam at a SXCT beamline. The usable energy range for SXCT at *BAMline* is 7 keV to 60 keV enabling a maximum flux density of up to $8 \times 10^{10} \text{ photons s}^{-1} \text{ mm}^{-2}$.

2.1.5 Data Treatment

All presented XCT and SXCT images were filtered after reconstruction using the plug-in *Non-Local Means Denoising* [85, 86] of the open-source imaging software *Fiji* [87] to reduce noise without blurring edges. Most segmentation of voids was performed using the commercial software *VG Studio MAX* Version 3.1–3.4 (Volume Graphics GmbH, Heidelberg, Germany). A lower threshold of 8 voxels was used to define the smallest detectable void. The segmentation of creep voids in the broken creep samples (see chapter 4.5 and 5.4) was performed using the open source software *iLastik* [88] since its machine learning segmentation mechanisms were able to segment creep induced voids in a more sophisticated way than the threshold based algorithms of *VG Studio MAX*.

Remark PBF-LB/M material consists of a columnar grain morphology parallel to the build direction. To reflect this fact in the XCT data, the bottom part of the depicted reconstructed volumes always represents the part which was located close to the build plate.

2.2 Residual Stress Determination by Neutron Diffraction

The following chapter is based on the paper *Residual stress. Part 1 – Measurement techniques* by Philip J. Withers and Harshad K. D. H. Bhadeshia [47] and the book *Neutrons and Synchrotron Radiation in Engineering Materials Science: From Fundamentals to Applications* edited by Peter Staron, Andreas Schreyer, Helmut Clemens and Svea Mayer [89].

2.2.1 Residual Stresses and Their Classification

Residual Stresses (RS) are stresses that exist in a body without the application of external loads or forces. RS are classified into three groups by the scale over which they self-equilibrate [47]:

Type I These macro-stresses (σ_I) vary over the size of an object. Changes to the equilibrium of bodies in which Type I RS exist always will cause macroscopic changes to the body [90]. Therefore, the influence of this type of RS has to be considered concerning the service life of the component.

Type II These intergranular RS (σ_{II}) vary over the length-scale of a few grains within the material of the body. In polycrystalline materials intergranular RS nearly always exist due the different thermal and elastic properties of differently orientated grains [47]. Type II stresses occur in multi-phase crystalline materials where the the lattice parameter varies between phases. Changes to the equilibrium of bodies in which type II stresses exist, can cause macroscopic changes to the body [90].

Type III These RS (σ_{III}) vary within a single grain. They include RS caused by dislocations as well as RS due to coherence at interfaces. Changes to the equilibrium of bodies in which type III stresses exist, do not cause macroscopic changes to the body [90].

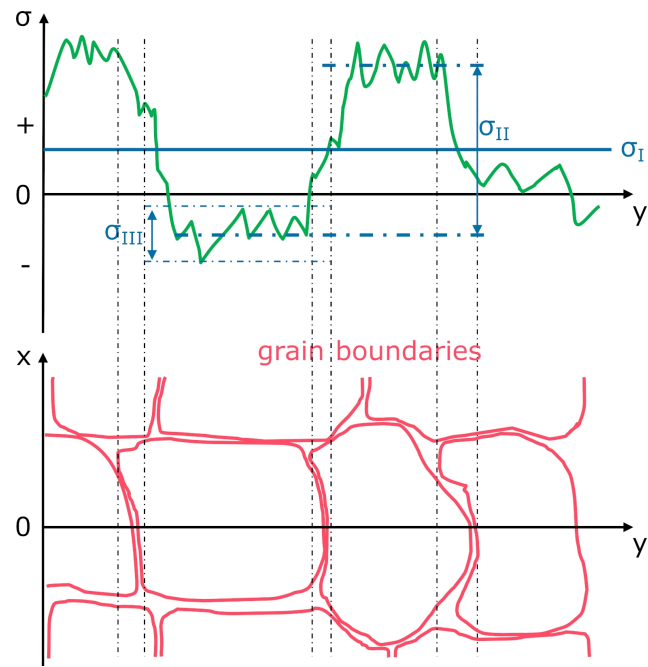


Fig. 2.7: Length scale of residual stresses

2.2.2 Description of Residual Stresses

Stress Tensor

All volumes can be divided into infinitesimal small volume elements. These volume elements are subject to forces from its vicinity, which act on the surface of these volume elements. The surface of the volume elements can be described by the spatial orientation of their respective normal vector \mathbf{n} . For simplicity reasons the Cartesian coordinate system is used for the following equations.

$$\mathbf{n} = \begin{pmatrix} n_1 \\ n_2 \\ n_3 \end{pmatrix} \quad (2.8)$$

The acting forces also can be described as a vector:

$$\mathbf{F} = \begin{pmatrix} F_1 \\ F_2 \\ F_3 \end{pmatrix} \quad (2.9)$$

The stress tensor $\boldsymbol{\sigma}$ describes the application of the acting force \mathbf{F} onto the respective orthogonal section of the surface A of the volume element:

$$\boldsymbol{\sigma} \cdot \mathbf{n} = \frac{\mathbf{F}}{A}, \quad \sigma_{ij} n_j = \frac{F_i}{A} \quad (2.10)$$

The diagonal entries (σ_{ii}) of the stress tensor $\boldsymbol{\sigma}$ describe the stress components which act along the normal direction of the six surfaces of the cubic volume elements. These are usually referred to as *normal stresses*. Its other components (σ_{ij} , $i \neq j$) describe the stress components which act parallel to the respective surfaces of the volume elements. They are referred to as *shear stresses*.

$$\boldsymbol{\sigma} = \begin{pmatrix} \sigma_{11} & \sigma_{12} & \sigma_{13} \\ \sigma_{21} & \sigma_{22} & \sigma_{23} \\ \sigma_{31} & \sigma_{32} & \sigma_{33} \end{pmatrix} \quad (2.11)$$

Strain Tensor

The acting forces on an infinitesimal volume element of an component result in a displacement $\mathbf{u}(\mathbf{x})$.

$$\mathbf{u} = \begin{pmatrix} u_1 \\ u_2 \\ u_3 \end{pmatrix} \quad (2.12)$$

For “small” displacements (*i.e.*, $\|\nabla \mathbf{u}\| \ll 1$) which is valid for most engineering materials with the exception of rubber-like materials [89] the relation between displacements and strains is given by:

$$\varepsilon_{ij} = \frac{1}{2} \left(\frac{\partial u_i}{\partial x_j} + \frac{\partial u_j}{\partial x_i} \right) = \frac{1}{2} (u_{i,j} + u_{j,i}) \quad (2.13)$$

The results from equation 2.13 can be combined to a second rank tensor:

$$\boldsymbol{\varepsilon} = \begin{pmatrix} \varepsilon_{11} & \varepsilon_{12} & \varepsilon_{13} \\ \varepsilon_{21} & \varepsilon_{22} & \varepsilon_{23} \\ \varepsilon_{31} & \varepsilon_{32} & \varepsilon_{33} \end{pmatrix} \quad (2.14)$$

Hooke's Law

Hooke's law connects stresses and strains in a linear equation:

$$\boldsymbol{\sigma} = \mathbf{C} \boldsymbol{\varepsilon} \quad (2.15)$$

whereas \mathbf{C} is the fourth rank *stiffness tensor* or elasticity tensor. If isotropy of a crystalline material is assumed, the 21 different entries of the *stiffness tensor* can be reduced to two. The fourth rank tensor is given in the Voigt notation.

$$\mathbf{C} = \begin{pmatrix} 1 - \nu & \nu & \nu & 0 & 0 & 0 \\ \nu & 1 - \nu & \nu & 0 & 0 & 0 \\ \nu & \nu & 1 - \nu & 0 & 0 & 0 \\ 0 & 0 & 0 & \frac{1-2\nu}{2} & 0 & 0 \\ 0 & 0 & 0 & 0 & \frac{1-2\nu}{2} & 0 \\ 0 & 0 & 0 & 0 & 0 & \frac{1-2\nu}{2} \end{pmatrix} \quad (2.16)$$

Therefore, for the isotropic case Hooke's law can be simplified to:

$$\sigma_{ij} = \frac{E}{1 + \nu} \varepsilon_{ij} - \frac{\nu E}{(1 + \nu)(1 - 2\nu)} \delta_{ij} \varepsilon_{kk} \quad (2.17)$$

whereas δ is the Kronecker function (which is defined as $\delta_{ij} = 1 \quad \forall i = j$ and $\delta_{ij} = 0 \quad \forall i \neq j$), E is the Young's modulus, and ν the Poisson's ratio of the material.

2.2.3 Neutron Diffraction Techniques for the Analysis of Residual Stress

Neutrons possess a high penetration, of the order of centimetres in most metals used in engineering. This is up to three orders of magnitude higher than that for X-rays [91]. Therefore, they are well suited to determine (bulk) residual elastic strain profiles which are needed to calculate the respective RS.

Principle of Diffraction

Stress determination using diffraction is based on using measurements of lattice spacing using diffraction. Diffraction occurs under the condition specified by Bragg's law whereby constructive interference of incoming planar waves occurs. In a lattice many different families of planes can be defined. To differentiate the plane families the Miller indices are used. They determine these plane families by a set of three integers h , k and l which describe the values of the three orthogonal base vectors of this plane family in the reciprocal space. William Lawrence Bragg and his father

William Henry Bragg postulated the connection between diffraction angle of the planar wave and lattice spacing in 1913 [92]:

$$2d^{hkl} \sin \theta^{hkl} = n \lambda \quad (2.18)$$

where d^{hkl} denotes the lattice spacing of the hkl plane family, θ^{hkl} its diffraction angle and λ the wavelength of the incoming planar wave.

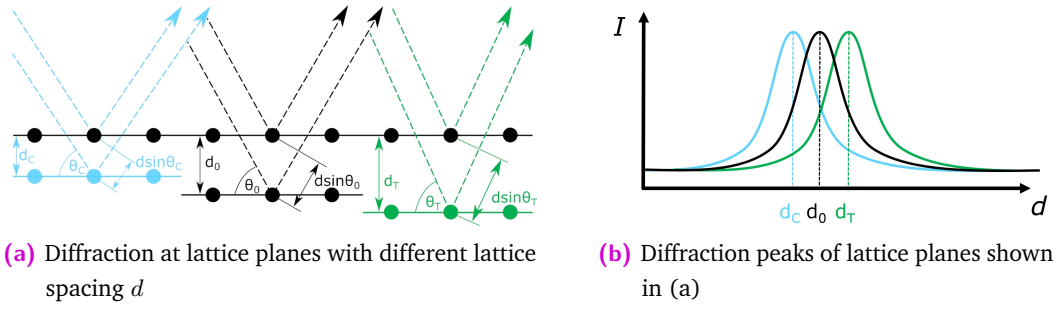


Fig. 2.8: Diffraction at lattice planes of a crystalline structure under compression d_C , stress-free d_0 and under tension d_T

Therefore, the lattice spacing d^{hkl} can be calculated from the measured diffraction angles. If a strain-free reference value of the lattice spacing is known, the elastic strain can be calculated. There are different approaches to determine a strain-free reference (e.g., filings or pulverised material). For AM metals often a small cubic sample (i.e., coupon) of an edge length of a few mm (ideally from a twin specimen) is used, since in contrast to powders it received the same thermal treatment as the object itself. Also, if removed from the twin object by electrical discharge machining, coupons are not plastically deformed as filings. The small cubic sample of an edge length of a few mm is used as stress-free reference, since most engineering stresses (type I) are assumed to be balanced over the small sample size. From the difference in value of the lattice spacing d^{hkl} of a component and the lattice spacing d_0^{hkl} of a strain-free reference sample of the same material, the elastic strain can be calculated by the following equation:

$$\varepsilon^{hkl} = \frac{d^{hkl} - d_0^{hkl}}{d_0^{hkl}} = \frac{d^{hkl}}{d_0^{hkl}} - 1 = \frac{\sin \theta_0^{hkl}}{\sin \theta^{hkl}} - 1 \quad (2.19)$$

from the elastic strain ε^{hkl} the stresses σ^{hkl} can be determined as shown in section 2.2.2. So, the atomic lattice planes are used as an so-called *atomic strain gauge*.

Remark It should be noted that the use of a distinct hkl -peak requires the use of the respective Young's modulus E^{hkl} and Poisson ratio ν^{hkl} of the selected reflection in equation 2.17. These can be derived from the Eshelby-Kröner model [93, 94]. For face-centered cubic (fcc) iron based materials (as presented in this work) usually the Fe_{311} -peak is selected due to the low accumulation of inter-granular stresses reported for this reflection in iron based fcc materials [91].

Diffraction Set-up

Present neutron beamlines rely on neutrons produced either by a spallation source or by a nuclear reactor. Mainly thermal neutrons using a wavelength of 1 \AA to 3 \AA are used for strain scanning achieving a resolution of up to 10^{-4} for the lattice spacing which corresponds to a resolution of 20 MPa in steel [89]. Since, in this work results from the STRESS-SPEC diffraction instrument [95] (Maier-Leibnitz Zentrum, Garching, Germany) are presented, the diffraction set-up for a reactor beamline is described. To select the wavelength a bent Si_{400} single crystal monochromator is used. The monochromatised neutron beam is usually shaped to a rectangular form by a system of beam-defining slits as depicted in fig. 2.9. The diffracted neutron beam is also shaped into a rectangle by a radial collimator. Therefore, the signal received by the detector results from diffraction within a gauge volume of the component which has the shape of a parallelepiped (*i.e.*, rhomboid).

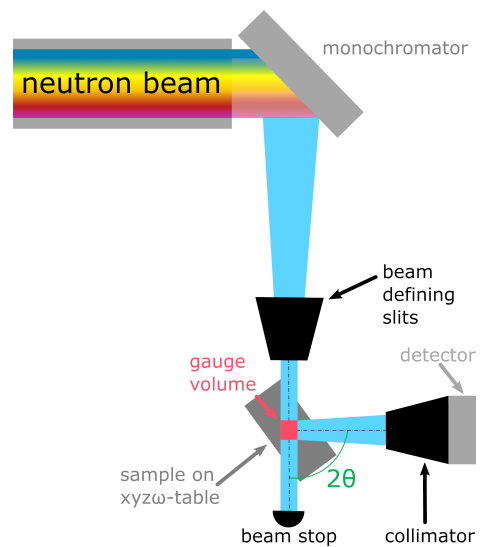


Fig. 2.9: Schematic of the STRESS-SPEC beamline at MLZ, Garching, Germany

“ Any sufficiently advanced technology is indistinguishable from magic.

— Arthur C. Clarke

(Profiles of the Future: An Inquiry Into the Limits of the Possible)

3.1 PBF-LB/M/316L Machine Parameter

All specimens described in this work were produced in-house at BAM by division 9.6 (Additive Manufacturing of Metallic Components) on a commercial PBF-LB/M system SLM280HL (SLM Solutions AG, Lübeck, Germany). This system is equipped with an 400 W continuous wave ytterbium fibre laser, which formed a focal spot size of $80\ \mu\text{m}$ at an emitted laser wave length of 1070 nm [26]. All build jobs were performed under an Argon shielding atmosphere. The resulting oxygen content in the build chamber was below 0.1 % [38].

The scope of the project AGIL did not involve the characterisation of influence of surface roughness on mechanical properties. Therefore, an as-built specimen geometry was chosen to enable the mechanical extraction of different types of specimen for mechanical testing (cylindrical tensile specimens, cylindrical creep specimens and cuboid single edge notch bending specimens). Within the project a as-built cuboidal specimen size of $112 \times 20 \times 13\ \text{mm}^3$ was agreed. In addition to versatility issues the near net-shape specimen geometry helped to avoid variations of properties due to geometrical changes in the building direction, which might influence the resulting microstructure [67, 96]. 18 tower-shaped specimen were build on a base plate sized $280 \times 280\ \text{mm}^2$ in several production lots. Additionally, the build angle was altered to study its influence on void formation. Tensile specimens from towers oriented 45° and 0° towards the build plate were studied as well as tensile specimens extracted at the same angles from a wall geometry as depicted in fig. 3.1.

Tab. 3.1: Optimal machine parameters for AISI 316L as suggested by the machine manufacturer SLM Solutions GmbH

Laser Power	Scan Velocity	Hatch Distance	Layer Thickness
P	v	h	t
275 W	700 mm s ⁻¹	0.12 mm	0.05 mm

A meandering stripe scanning strategy was used without additional border and contour scans. The stripe orientation was alternated by 90° between even and odd layers.

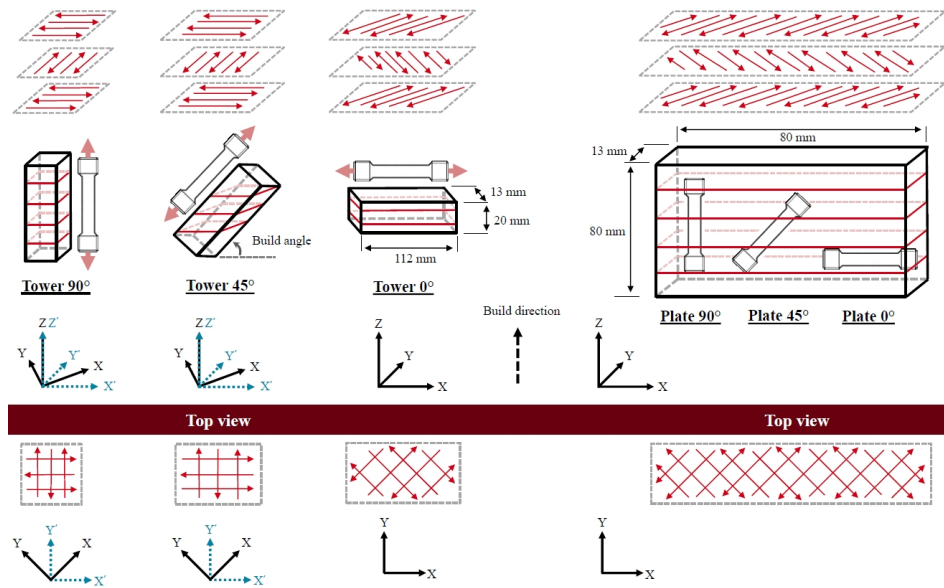


Fig. 3.1: Build angle of the compared specimen extracted from built tower and wall geometries as depicted in the paper by Charmi et al. [17]

The machine was additionally retrofitted with an thermographic camera system to enable a detailed on-line monitoring of the build process. A detailed description of the thermography set-up can be found in Mohr et al. [26] and Ulbricht et al. [38].

3.2 AISI Stainless Steel 316L

For all PBF-LB/M/316L specimens in this work gas atomised powder supplied by the PBF-LB/M machine manufacturer SLM Solutions AG was used. The powder was gas atomised under nitrogen atmosphere. The characterisation was performed by the

supplier and its characteristics are given in the following tables. The resulting solid material is crystalline and based on a fcc unit cell.

Tab. 3.2: Characteristics of the AISI 316L Powder Particles

Apparent Density	Mean Diameter	D ₁₀	D ₅₀	D ₉₀
4.58 g μm ⁻³	35 μm	18 μm	31 μm	56 μm

Tab. 3.3: Chemical composition of the AISI 316L Powder as provided by its supplier

Element	Minimum /wt%	Actual /wt%	Maximum /wt%
Fe	Balance	Balance	Balance
C	–	0.017	0.030
Si	–	0.60	1.00
Mn	–	0.92	2.00
P	–	0.012	0.045
S	–	0.004	0.030
Cr	16.00	17.7	18.00
Ni	10.00	12.6	14.00
Mo	2.00	2.35	3.00
N	–	0.10	0.10

The conventional 316L specimens were extracted from hot rolled plates. The chemical composition of the hot rolled material was given by the supplier and is listed in the following table.

Tab. 3.4: Chemical composition of the conventional hot rolled AISI 316L material

Element	Minimum /wt%	Actual /wt%	Maximum /wt%
Fe	Balance	Balance	Balance
C	–	0.017	0.030
Si	–	0.45	0.60
Mn	–	1.23	2.00
P	–	0.031	0.045
S	–	0.001	0.015
Cr	16.5	16.9	18.00
Ni	10.00	10.1	13.00
Mo	2.00	2.03	2.50
N	–	0.05	0.10

3.3 Specimens

3.3.1 Specimens for Tensile and Creep Tests

After an initial heat treatment of 450 °C for 4 h the towers were removed from the base plate using a band saw. Creep and tensile specimens were produced by turning. Round creep specimens had dimensions of 100 mm × M12. Their parallel length was 60 mm, their diameter was 8 mm. The tensile specimen had dimensions of 64 mm × M10 with parallel length of 32 mm and 6 mm diameter. Their parallel length is 36 mm. Creep testing was conducted by PhD student Luis Ávila and performed by research assistant Sina Schriever. The two researchers are members of division 5.2 (Experimental and Model Based Mechanical Behaviour of Materials) at BAM. The mechanical and microstructural analysis of these specimens was performed by Luis Ávila as is reported in [67]. The testing parameters and results are given in table 3.5. Creep curves of the specimens examined within this thesis are given in fig. 3.2. Three PBF-LB/M/316L specimens were examined by XCT. Two specimens were examined in the starting condition pre-testing, interrupted at the starting stages of tertiary creep, and post-fracture. One additional specimen was examined in the post fracture condition. A benchmark specimen for a PBF-LB/M/316L creep specimen manufactured from hot rolled 316L was also tested in the pre-testing, interrupted and final fracture condition.

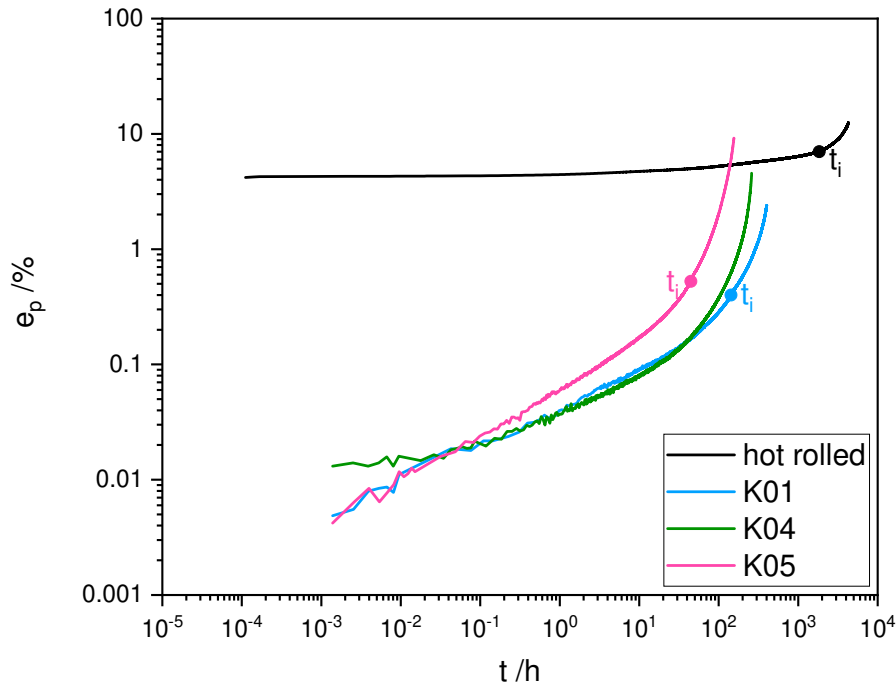


Fig. 3.2: Creep curves of the investigated specimens of table 3.5. t_i marks the point of interruption of the tests as presented in the paper of Ávila et al. [67]

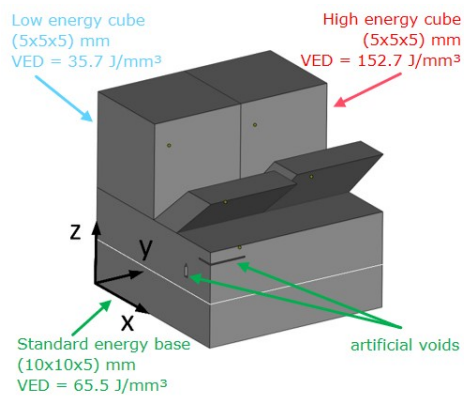
Tab. 3.5: Experimental data of the creep tests of the PBF-LB/M/316L specimens K01, K04, K05 and the conventional hot rolled specimen as presented in the paper of Ávila et al. [67]

		K01	K04	K05	hot rolled
Testing Temperature	T	600 °C	600 °C	650 °C	600 °C
Applied Stress	R_0	200 MPa	225 MPa	175 MPa	225 MPa
Stress-rupture Life	t_u	402 h	260 h	155 h	4287 h
Time of Interruption	t_i	143 h	–	44.8 h	1844 h
Total Strain under Load	e_{ti}	0.19 %	0.17 %	0.18 %	4.4 %
Elastic Strain under Load	e_e	0.19 %	0.16 %	0.18 %	0.27 %
Plastic Strain under Load	e_i	0.00 %	0.01 %	0.00 %	4.16 %
Creep Strain under Load	e_f	2.40 %	4.60 %	9.20 %	8.40 %
Total Plastic Strain	e_p	2.40 %	4.61 %	9.20 %	12.6 %

3.3.2 Specimens for the Analysis of Artificial Voids

Artificial Voids from Variation of VED

To provoke the formation of extensive populations of voids, the process parameters were subsequently altered. Three different VED were used on three parts of a specimen of AISI 316L. As depicted in fig. 3.3 the specimen DPK002 was built containing a base section of $10 \times 10 \times 5 \text{ mm}^3$ using the standard VED of 65.5 J mm^{-3} , a high VED tower (size: $5 \times 5 \times 5 \text{ mm}^3$; $\text{VED} = 152.7 \text{ J mm}^{-3}$) and a low VED tower (size: $5 \times 5 \times 5 \text{ mm}^3$; $\text{VED} = 35.7 \text{ J mm}^{-3}$).



(a) CAD of the specimen



(b) Photo of the produced specimen

Fig. 3.3: Shape of the specimen DPK002

As for the tensile and creep specimen an meandering stripe scan strategy with 90° rotation for each layer was applied. For the base section the same standard parameters for 316L were used as for the tensile and creep specimens. A lower VED was achieved by reducing the laser power to 150 W while keeping the remaining machine parameters constant. The high VED tower was also based on standard parameters but the scanning velocity was reduced to 300 mm s^{-1} while keeping the remaining parameters constant. Further information on the production can be found in [26].

Healing of Previously Unexposed Layers

To study the ability of the laser to melt subjacent layers a cylindrical specimen was designed. It had a diameter of 7 mm and a height of 12 mm. The build used the same standard machine parameters as the creep and tensile specimen. Based on

the standard layer thickness of $50\mu\text{m}$ this resulted in a total of 240 layers. At nine heights, a quarter of the cross-section of the cylinder was not exposed by the laser. The position of the quarters were rotated over the build height to prevent heat accumulation (see fig. 3.4a). A surrounding staircase was part of the design. The non-exposed layers start height was aligned to the steps of the staircase for an easier registration of the non-exposed quarters in the XCT data. A gap between the inner cylinder and the staircase was introduced to enable the removal of the staircase for a XCT scan with a higher resolution (see fig. 3.4). This design was derived from Gobert et al. [97]. Additionally, an embossed T shaped mark was added to the cylinders top surface to enable a easier registration of the XCT data of different resolutions onto each other. The scan strategy differed from the previously described specimens: To minimize the porosity in the specimen a meandering stripe scan strategy was applied where the orientation of the stripe pattern rotated by 67° for each layer [61]. To create smooth surfaces and precise part dimensions a contour fill scan and border scan were used additionally. The execution order for the 3 scan strategies was the following: meander stripe scan, fill contour scan and border scan. At the location of the non-exposed quarters the contour scan followed the inner borders of the part to allow the removal of unmolten powder from the quarters. A void visible at the outer surface of the cylinder at a position of a quarter is depicted in fig. 3.4d (yellow mark). Prior to the actual specimen a small cylindrical base was built. This enabled the removal from the base plate using a band saw without cutting into the actual specimen.

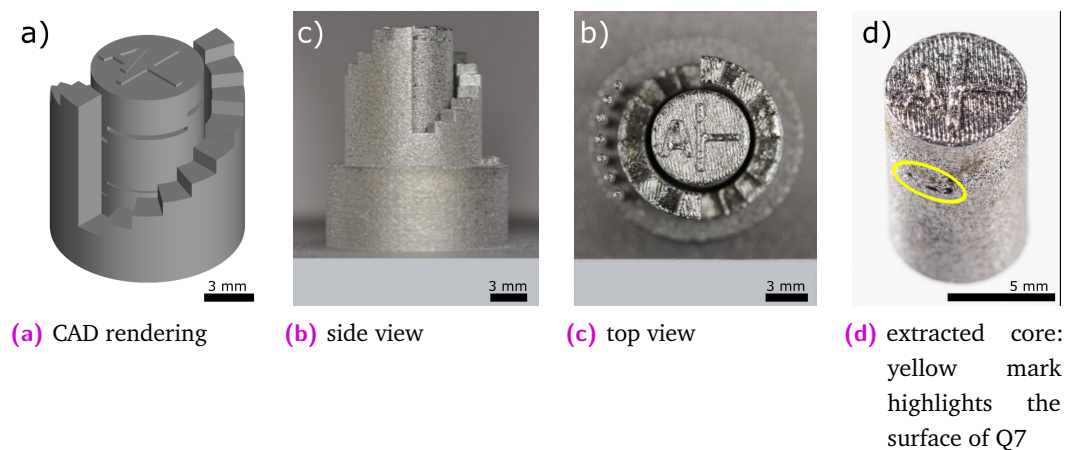





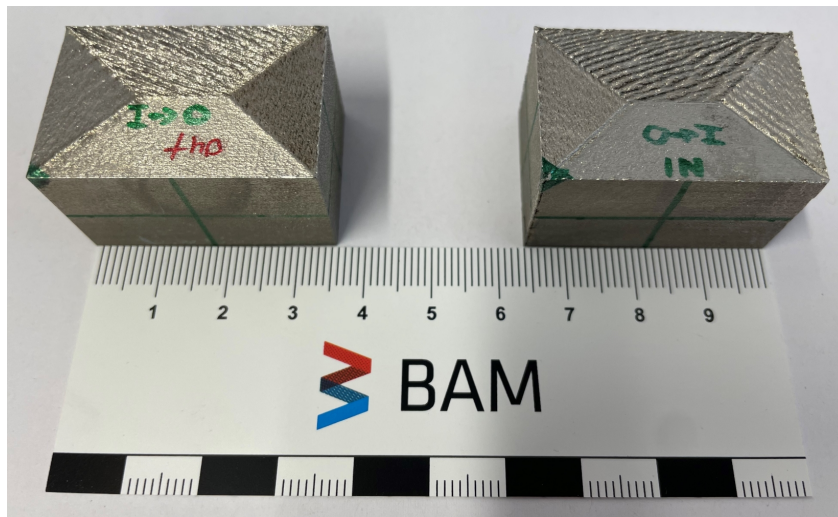
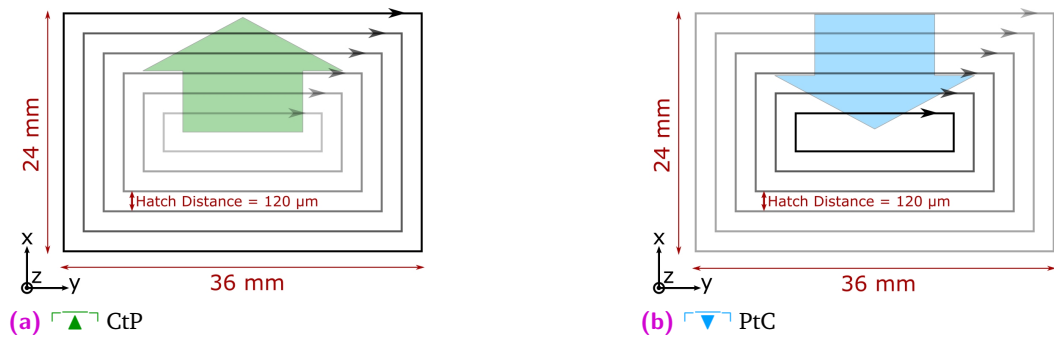
Fig. 3.4: DPK003-A specimen

Tab. 3.6: Overview of the position and characteristics of the non-exposed quarters. The height to be exposed included the height of the non-exposed quarter plus the thickness of the first fully exposed layer above ($50\ \mu\text{m}$)

number of the quarter	start height from base	number of non-exposed layers	height of the non-exposed layers	number of the layers	height to be exposed
Q1	3 mm	1	$50\ \mu\text{m}$	61	$100\ \mu\text{m}$
Q2	4 mm	2	$100\ \mu\text{m}$	81–82	$150\ \mu\text{m}$
Q3	5 mm	3	$150\ \mu\text{m}$	101–103	$200\ \mu\text{m}$
Q4	6 mm	4	$200\ \mu\text{m}$	121–124	$250\ \mu\text{m}$
Q5	7 mm	5	$250\ \mu\text{m}$	141–145	$300\ \mu\text{m}$
Q6	8 mm	6	$300\ \mu\text{m}$	161–166	$350\ \mu\text{m}$
Q7	9 mm	7	$350\ \mu\text{m}$	181–187	$400\ \mu\text{m}$
Q8	10 mm	8	$400\ \mu\text{m}$	201–208	$450\ \mu\text{m}$
Q9	11 mm	9	$450\ \mu\text{m}$	221–229	$500\ \mu\text{m}$

3.3.3 Specimens for Residual Stress Analysis

To unravel how the two known formation mechanisms for RS, the TGM and the CSSM [13], shape the RS distribution in PBF-LB/M/316L components two prism-shaped specimen of $36 \times 24 \times 24.5\ \text{mm}^3$ were designed [39]. A band saw was used to remove the specimens from the base plate. Therefore, the final height of the specimens was reduced to 21 mm from the initial 24.5 mm. The two specimen were built using the standard parameters provided by the machine's supplier as listed in table 3.1 on page 32. The two specimens also feature an almost identical border fill scan strategy. The difference was the directions of how the rectangular scan vectors were applied: one was illuminated from the centre towards the perimeter (Centre-to-Perimeter (CtP), ), and the other from the perimeter towards the centre (PtC, ) as depicted in fig. 3.5. Using the same geometric scan vectors in the two specimen enables similar solidification shrinkage, whereas the different illumination direction creates a different thermal history for each of the two specimen. Therefore, similarities in the two specimen could be assigned to the CSSM and differences to the TGM. As d_0 reference to determine RS values from the ND data a cube of $3 \times 3 \times 3\ \text{mm}^3$ was used. The cube was extracted from the bottom of an interrupted test build of a PtC () specimen.



(c) Photo of the two specimens (left: CtP , right: PtC)

Fig. 3.5: Schematics of the two border fill scan strategies and photo of the produced specimens

Experimental Details & Results

” *When you really want to know how things work, study them when they fall apart.*

— **William Gibson**
(Zero History)

This chapter combines the results of studies on void formation in PBF-LB/M/316L as well as studies on RS formation, and studies on the materials response to mechanical loads at elevated temperatures.

4.1 Void Formation in PBF-LB/M/316L Using Standard Build Parameters

4.1.1 Experimental Details

To study the inherent porosity in PBF-LB/M/316L specimens using the machine manufacturer’s standard parameters the effect of build height, build angle and object size was analysed in different XCT experiments. A small pin of a diameter of $500\mu\text{m}$ was analysed using SXCT to determine if a lower boundary of pore size could be determined.

Build Height

A tensile round specimen was analysed for voids at three heights. Scans were performed at a custom build XCT scanner at BAM in div. 8.5 (Micro Non-Destructive Testing). The scanner was equipped with a 225 kV micro focus X-ray tube (X-RAY WorX GmbH, Garbsen, Germany) and a 2k flat panel detector (PerkinElmer, Inc., Waltham, USA). The used X-ray parameters are shown in table 4.1.

Tab. 4.1: Acquisition parameters for a tensile specimen scanned at three different heights

Voltage	Current	Projections			Filter	Voxel Size
		N ^o	Time	Average		
210 kV	90 μ A	2400	2 s	3	0.25 mm Cu 0.25 mm Al	5.4 μ m

Build Angle and Size of the Built Object

The six tensile samples extracted from tower and wall geometry were built using standard build parameters (see table 3.1 on page 32). The XCT data acquisition was performed on the commercial XCT scanner GE V|tome|x 180/300 (GE Sensing Inspection Technologies GmbH, Wunstorf, Germany). The scanning parameters are given in table 4.2.

Tab. 4.2: Acquisition parameters for tensile specimens

Voltage	Current	Projections			Filter	Voxel Size
		N ^o	Time	Average		
200 kV	50 μ A	2000	2 s	3	0.25 mm Ag	10 μ m

Minimum Void Size

In order to study possible voids with sizes below that of the resolution of laboratory XCT, small pins ($L = 5$ mm, $\varnothing = 0.5$ mm) were extracted from the wall in vertical orientation (*i.e.* build direction) and horizontal orientation (*i.e.*, parallel to the wall's long side). These pins were scanned at the SXCT beamline BAMline. The used parameters are given in table 4.3.

Tab. 4.3: SXCT acquisition parameters for the small pin extracted from the wall

Energy	Projections			Filter	Voxel Size
	N ^o	Time	Average		
50 keV	2500	5 s	–	–	0.438 μ m

The pin was also scanned using laboratory XCT for comparison. The used parameters of the commercial XCT Scanner GE v|tome|x 180/300 (GE Sensing & Inspection Technologies GmbH, Wunstorf, Germany) are given in the table below.

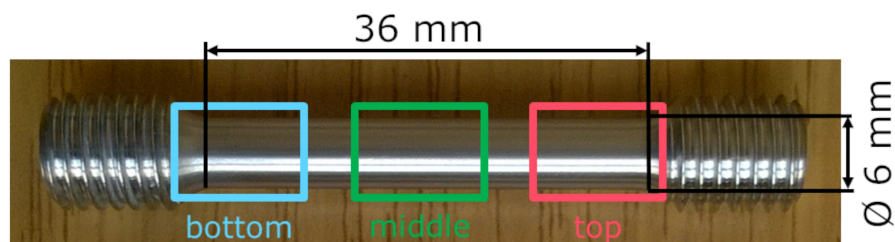
Tab. 4.4: XCT acquisition parameters for the small pin extracted from the wall

Voltage	Current	Projections			Filter	Voxel Size
		№	Time	Average		
140 kV	60 μ A	1700	2 s	3	–	1.3 μ m

4.1.2 Results

Build Height

The following figures show the void distribution of an PBF-LB/M/316L tensile specimen before mechanical testing. To study the influence of the build height on void distribution the tensile specimen was scanned using laboratory XCT at three different heights (see fig. 4.1).



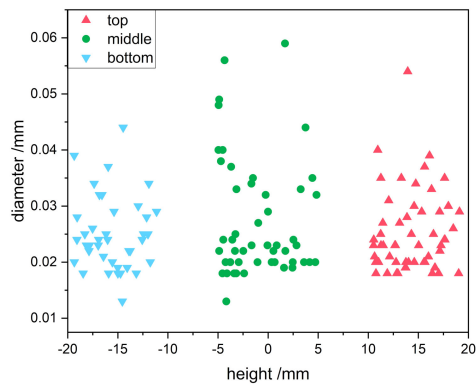
(a) Position of the scanned heights



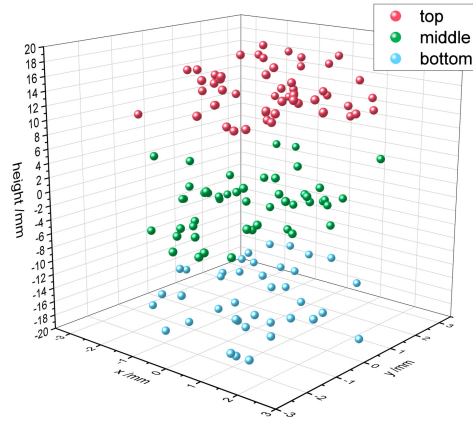
(b) Virtual cut of the scanned heights

Fig. 4.1: Tensile specimen scanned at 3 heights

As shown in fig. 4.2 build height does not seem to have a significant influence to void formation in this specimen. Segmented voids seem to be evenly distributed in the analysed volumes. The shape of the voids is not perfectly spherical. To determine the size of the segmented voids different methods could be applied: For robustness of the results one can determine the equivalent diameter of a sphere of the same volume or of the same surface area than of a segmented void. The two methods



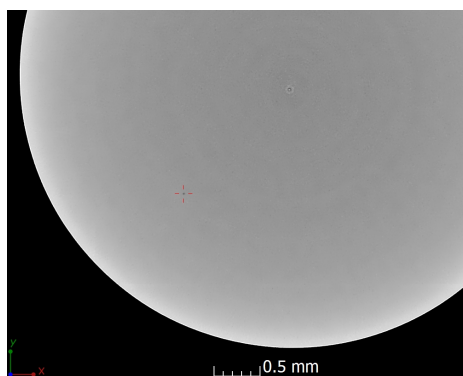
(a) Size of the segmented voids based on the evaluation of the voids' volume



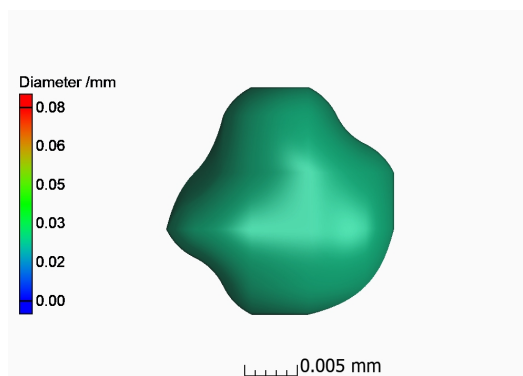
(b) 3D Distribution of voids in the tensile specimen

Fig. 4.2: Tensile specimen scanned at 3 heights

create slightly different results. The average volume of voids in the specimen was $4476.55 \mu\text{m}^3$ which correspond to a equivalent diameter of $20.44 \mu\text{m}$. The average surface area of the voids was $1917.45 \mu\text{m}^2$ which corresponds to an average diameter of $24.71 \mu\text{m}$. The difference in diameter depending on the calculation method is almost the voxel size of $5.4 \mu\text{m}$. Size determination based on volume evaluation is used in this work. Fig. 4.3 shows a average sized void of the mid section of the specimen.



(a) top view of a virtual cut containing the void ($\varnothing = 25 \mu\text{m}$)



(b) 3D rendering of the void's shape

Fig. 4.3: Magnified view of an average sized pore in the tensile specimen

Build Angle and Size of the Built Object

The analysis of the different heights of one tensile specimen did not reveal significant dependencies of the void formation on the build height 4.2a. Therefore, only the mid section of the specimens were scanned and analysed. All scans were analysed using the commercial software *VG Studio MAX 3.1* (Volume Graphics GmbH, Heidelberg, Germany). To ensure a comparable segmentation result, the same Region-of-Interest (RoI) was used for the void analysis.

Remark Due to subtle manufacturing differences in diameter the volume of the used RoI was not completely the same for each of the six specimens. All segmented voids were of mainly spherical shape. Porosity only changed slightly between the specimens' build orientation. For both, tower and wall geometry, the specimens of 45° orientation feature the highest number of segmented voids.

Tab. 4.5: Acquisition parameters for tensile specimens obtained from three build angles

	Analysed Volume	Volume of Voids	N ^o of Voids	Porosity
	\mm ³	\mm ³		\%
Tower 0°	443.1586	0.0005	28	<0.001
Tower 45°	443.7266	0.0015	73	<0.001
Tower 90°	442.5135	0.0009	42	<0.001
Wall 0°	443.1867	0.0007	43	<0.001
Wall 45°	445.1126	0.0013	59	<0.001
Wall 90°	444.6265	0.0010	57	<0.001

Minimum Void Size

For a vertically oriented pin extracted from the top section of the wall, only a few pores were detected. The largest segmented pore had a diameter of $\varnothing = 11 \mu\text{m}$ whereas the smallest had a diameter of $\varnothing = 2.7 \mu\text{m}$. Since this size is well above the voxel size of $0.438 \mu\text{m}$ there seems to be a lower boundary for voids in this specimen of PBF-LB/M/316L at $2.7 \mu\text{m}$. The larger void diameter shown in 4.4a emphasises the need of high resolution XCT results for a precise determination of the void's size.

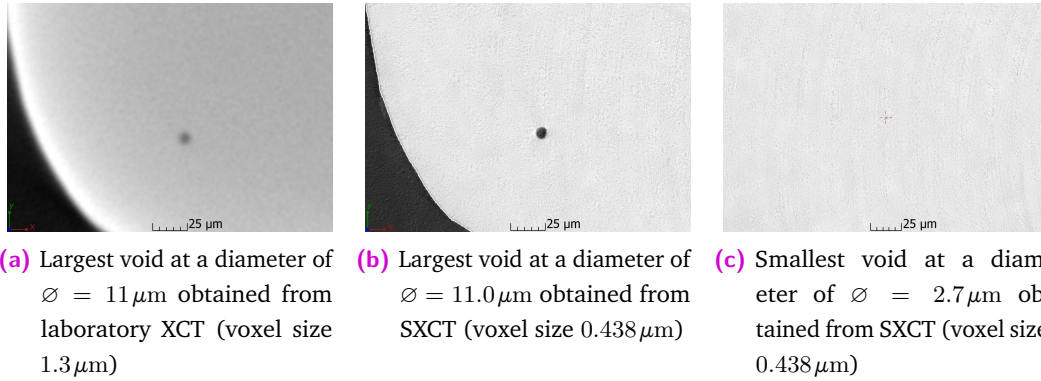


Fig. 4.4: Largest and smallest void found in a small pin extracted from a wall geometry

4.2 Void Formation in PBF-LB/M/316L by Varying the Scan Speed

4.2.1 Experimental Details

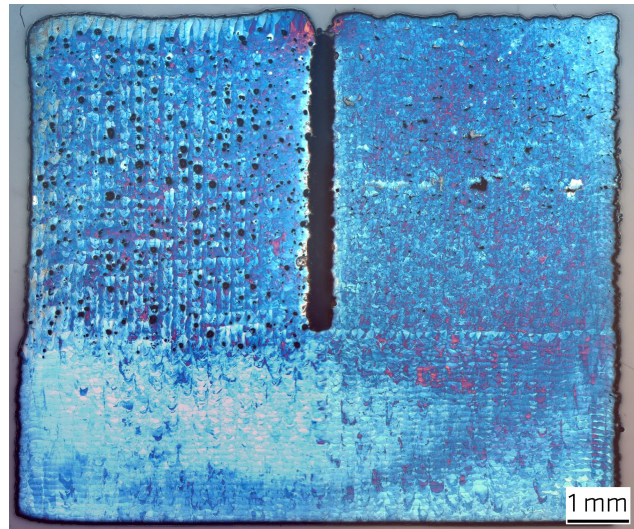
Since the use of standard parameters—as expected—did not result in a significant amount of voids the build parameters were altered to provoke the formation of voids. This was done in order to study void formation as a function of process parameters. As described in section 3.3.2 three different build parameter settings were used within a single specimen. A base section build using the standard VED was used as a reference. Two towers were build on top of the base with lower and higher than standard VED. XCT images were acquired using the same custom XCT scanner [98]. The scanning parameters used are given in table 4.6.

Tab. 4.6: Acquisition Parameters for DPK002

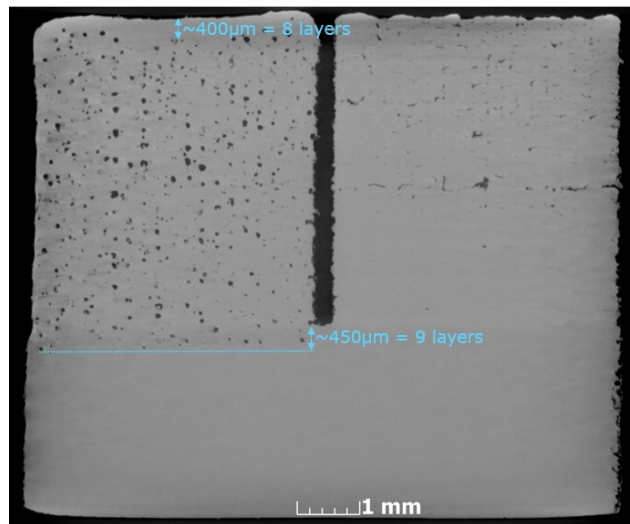
Voltage	Current	No	Projections		Filter	Voxel Size
			Time	Average		
200 kV	50 μ A	2000	2 s	3	0.25 mm Ag	7.12 μ m

4.2.2 Results

In the Low-VED tower exclusively LoF voids were detected and in the High-VED tower keyhole pores were present (see fig. 4.5 and fig. 4.6).



(a) metallographic cut of the DPK002 specimen made by Gunther Mohr [26]



(b) virtual cut of XCT volume matching the cut from (a)

Fig. 4.5: Comparison between XCT and metallurgic cuts showing the High-VED tower (at the left in both images), the Low-VED tower (at the right in both images) and the base section produced using the optimal VED (at the bottom in both images)

LoF voids of the Low-VED tower feature a non-spherical shape (see right tower in fig. 4.5a and fig. 4.5b) as described in section 1.3.3. They appear throughout the build volume of the Low-VED tower (see left tower in fig. 4.6a and fig. 4.6b) at the intersection of consecutive stripes of the scanning pattern.

The keyhole pores of the High-VED tower are spherical. In contrast to the voids in the Low-VED tower the appearance of the keyhole pores of the High-VED tower

is not limited to the volume of the High-VED tower (left tower in fig. 4.5a and fig. 4.5b). The increased energy input of the laser resulted in the formation of keyhole pores in the base section. Keyhole pores were present in nine layers of the base section. Interestingly, there is almost no porosity detectable at the top eight layers of the high XCT tower (see left tower in fig. 4.5b). In contrast to the low XCT tower, the top surface of the high XCT tower features a concave shaped dent in the centre (see fig. 3.3b on page 36).

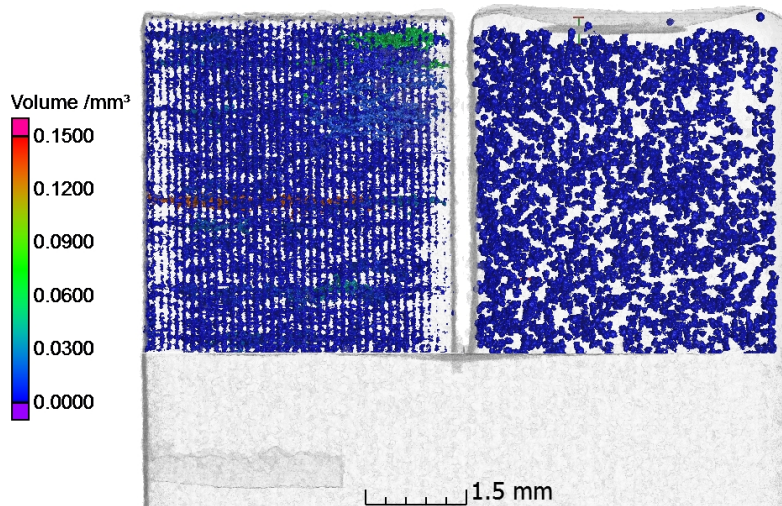
Remark The segmentation of voids within the XCT data was limited to the physical volume of the towers above the base section. Therefore, the keyhole pores induced into the base section below the High-VED tower were not part of segmented region, and consequently not displayed in fig. 4.6 and not part of the porosity values given in table 4.7.

As seen in the tensile specimens, the base section (produced using the standard VED parameters) did not contain many voids (see fig. 4.5 and table 4.7). As highlighted in fig. 4.5b the higher VED used for the High-VED tower seemed to have caused a deeper penetration of the material by the melt pool. This is observed by the presence of keyhole pores observed $450\mu\text{m}$ (equivalent to nine layers) within the already solidified base section.

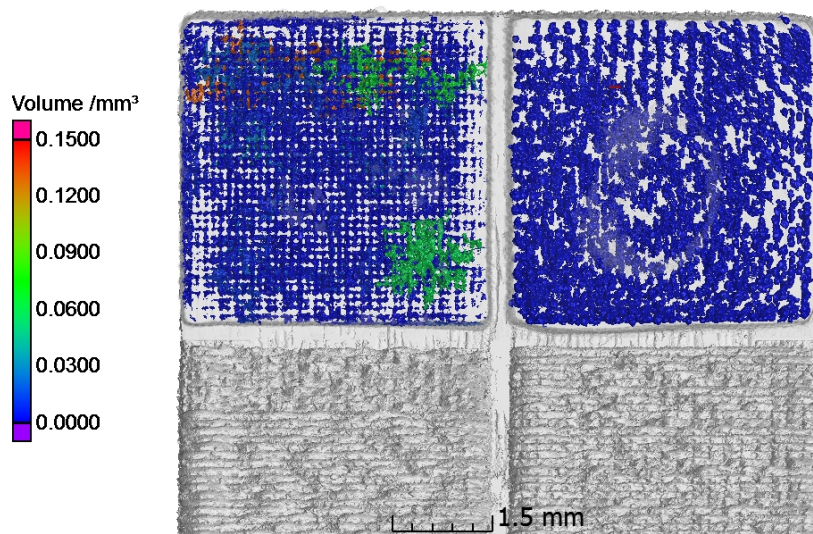
The ability to analyse the void distribution in 3D enables a more detailed analysis than 2D metallographic cuts. This becomes evident when comparing the information displayed in fig. 4.5 and fig. 4.6. The alignment of the LoF voids to the scanning pattern is only visible when the metallographic cut is placed exactly at intersection of scan stripes. Otherwise only void-free material can be seen. This limitation does not apply to the 3D XCT data. Therefore, regardless of the laser scan pattern, the void distribution can be correlated to it. In Section 4.3 on page 52 a detailed analysis of the effect of scanning patterns on void orientations within the void distribution is discussed. Metallographic cuts bear one significant advantage to the XCT data, which is the ability to visualise the shape of the melt pools (see fig. 4.5a). Such details cannot be obtained from XCT data only changes in the X-ray absorption are visualised.

Tab. 4.7: Porosity values of the three sections

	VED J mm^{-3}	Volume $\backslash\text{mm}$	Porosity $\backslash\%$
Base Section	65.5	$10 \times 10 \times 5$	0.003
Low-VED Tower	35.7	$5 \times 5 \times 5$	2.7*
High-VED Tower	152.7	$5 \times 5 \times 5$	7.4



(a) front view



(b) top view

Fig. 4.6: Distribution of internal voids in the Low-VED tower (at the left in both images) and the High-VED tower (at the right in both images)

Remark to * The porosity for the Low-VED tower is underestimated. The analysing routines of the used software *VG Studio MAX* segment voids by the grey level difference between gas in the voids and metal. In the Low-VED tower the LoF voids were partly filled with feedstock powder particles. Therefore, these particles reduce the apparent volume of these voids. Some powder particles can be seen in the void in the centre of the Low-VED tower (see fig. 4.5b and in fig. 4.7).

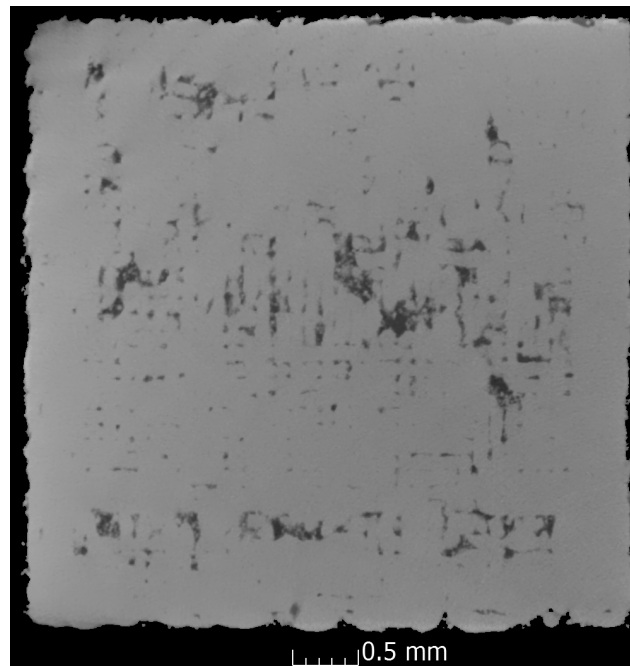
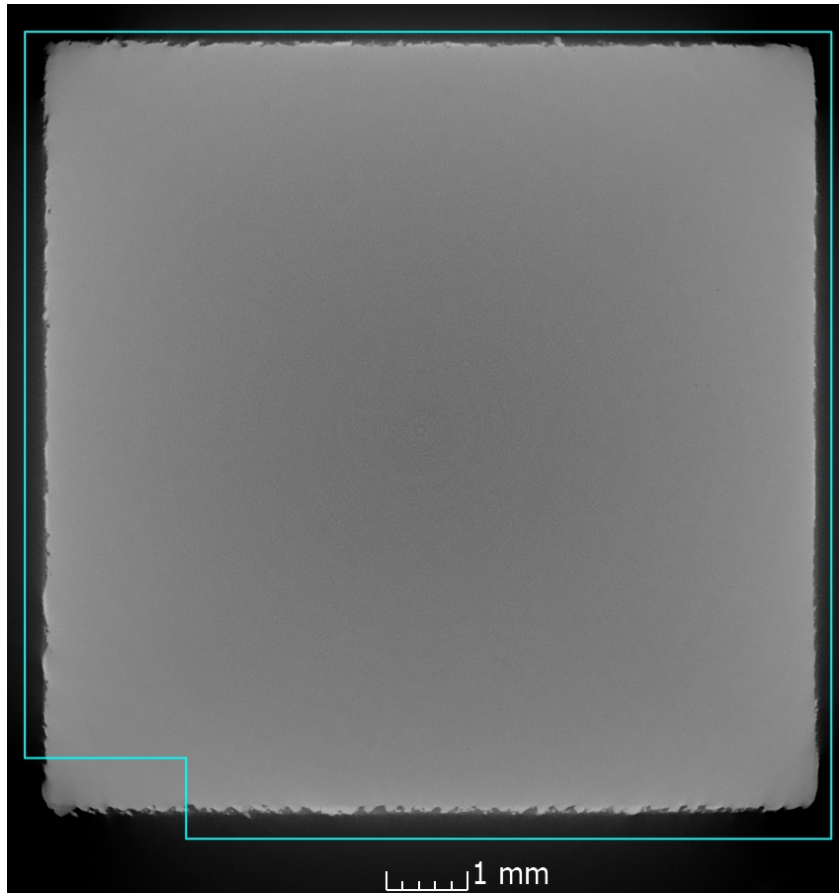
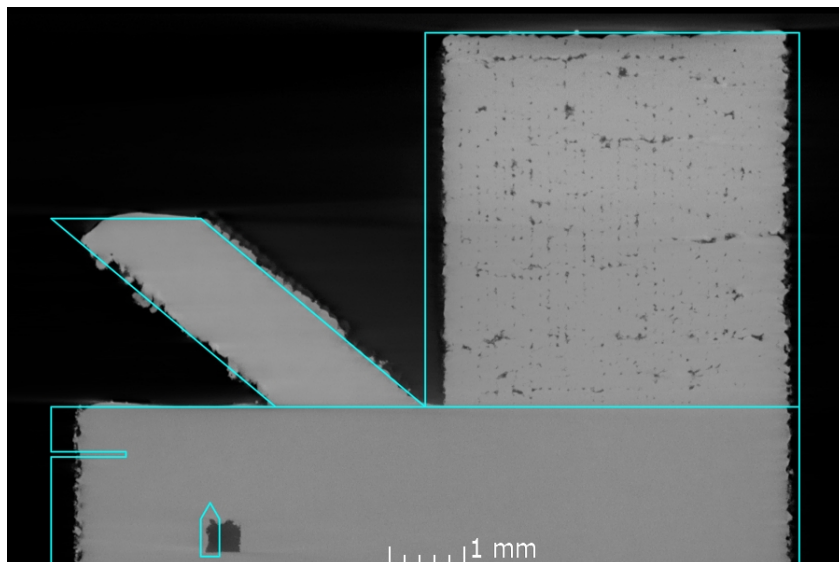


Fig. 4.7: Virtual transversal cut at the height of the ninth layer ($450\mu\text{m}$) of the Low-VED tower. Larger voids are filled with unmolten powder particles.

In addition to the towers, also artificial voids were added to the base section of the specimen by non-exposing certain areas by the laser. Fig. 4.8 shows an overlay of the Computer Aided Design (CAD) model of a one layer thick non-exposed edge with the XCT data of that specific area. The virtual cuts clearly show that the metal powder at the non-exposed edge was completely molten and solidified as a void-free area from the laser exposure of subsequent layers. This interesting result inspired a follow-up experiment to answer the question how many layers of powder can be molten by the laser without inducing any kind of voids. The results of this experiment are presented in the following section.



(a) Top view of the non-exposed corner



(b) Side view of the non-exposed corner

Fig. 4.8: Virtual cuts combined with the CAD revealing the *healed* non-exposed corner

4.3 Void Formation in PBF-LB/M/316L by Varying the Layer Thickness

4.3.1 Experimental Details

XCT acquisitions of the specimen DPK002 were made of the full specimen as well as of the separated inner cylinder. The commercial XCT scanner GE v|tome|x 180/300 (GE Sensing & Inspection Technologies GmbH, Wunstorf, Germany) was used to scan the whole specimen. The used scan parameters are given in table 4.8.

Tab. 4.8: Acquisition Parameters for the overview scan

Voltage	Current	Projections			Filter	Voxel Size
		N°	Time	Average		
222 kV	45 μ A	3000	2 s	3	1 mm Al	10 μ m

After the removal of the staircase using a band saw, the inner cylinder was scanned using a custom built XCT scanner. The scanner is based on a 225 kV micro focus X-Ray source (X-Ray WorX GmbH, Garbsen, Germany) and a flat panel detector with 2048×2048 pixels (PerkinElmer, Inc., Waltham, USA) [98]. Combining two scans of two heights a voxel size of $(5 \mu\text{m})^3$ was achieved. The scan parameters are given in table 4.9.

Tab. 4.9: Acquisition Parameters for tensile specimens

Voltage	Current	Projections			Filter	Voxel Size
		N°	Time	Average		
210 kV	60 μ A	3000	2 s	4	1 mm Cu 0.25 mm Al	5 μ m

The overview scan and the high resolution scan were registered onto each other using *VG Studio MAX*. The software was also used to determine the angle of the LoF voids in reference to a virtual 0° line. The software dimensioning tools were used to correlate the orientation of the LoF voids to the orientation of the stripe pattern obtained from thermographic OT data during the build job [38]. OT captures an intensity which is proportional to temporal integral of the thermal radiation in a defined wavelength range [99].

4.3.2 Results

In fig. 4.9b a ring of voids close to the perimeter of the cylinder is visible: Voids formed at the intersection of bulk and contour scan. It has been reported in literature [100, 101, 102] that this region is prone to void formation. Apart from these voids the results show that most of the feedstock powder in the unexposed quarters was molten by the laser exposure of the subsequent layers and solidified as void-free material. Fig. 4.9 shows the segmented voids. The porosity in the layers is directly linked to the amount of those voids found in the quarters. As shown in table 4.10 and fig. 4.10 no additional porosity was found in Q1 to Q4. In Q5 to Q9 LoF voids were observed.

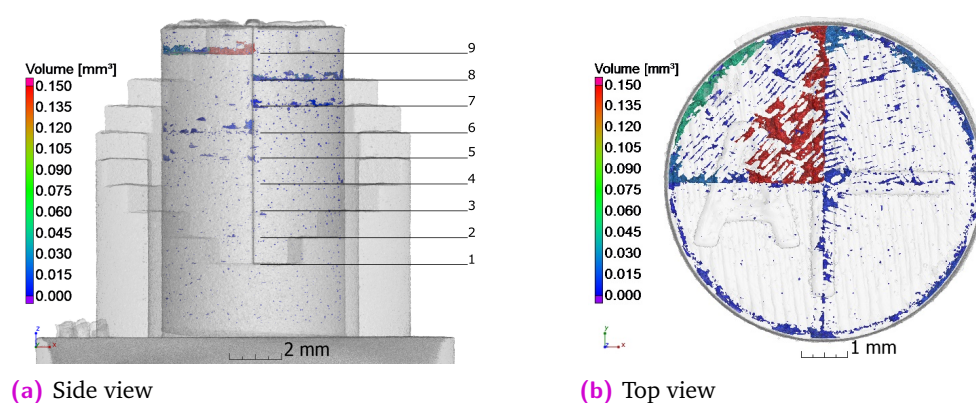
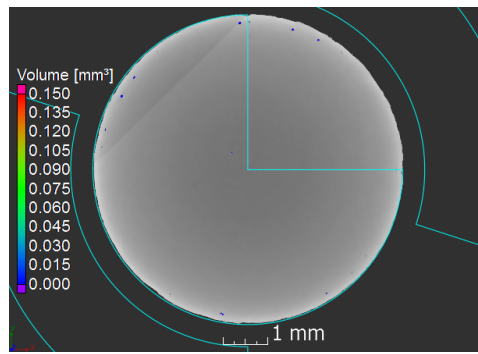


Fig. 4.9: 3D-rendering of the void distribution in the cylindrical specimen. Images taken from Ulbricht et al. [38]

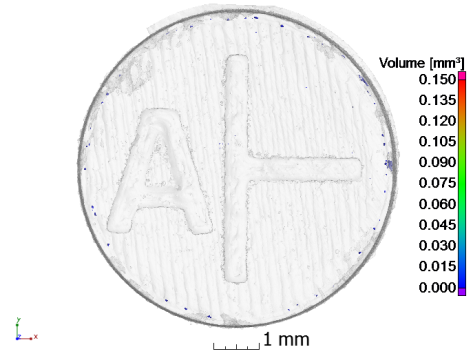
Even at Q9 (ten times the thickness of a standard layer, *i.e.*, $500\ \mu\text{m}$) only a porosity value of 5.6% was observed. This was surprising, since one would have expected to find unmolten powder particles in this quarter (As detected in the Low-VED tower of the specimen DPK002 shown in fig. 4.7 on page 50). Therefore, the DPK003 specimen had been designed with openings at the non-illuminated quarters to enable the removal of unmolten powder particles. This design goal was achieved by running the contour scan along the outline of the remaining three quarters of the illuminated material. This created an additional intersection between contour and bulk scan at the inner perimeter of the non-illuminated quarters. At the inner perimeter of the non-illuminated quarters voids were observed in Q6 and above (thickness of unexposed powder $> 300\ \mu\text{m}$). In Q8 and Q9 (unexposed thickness region of $> 450\ \mu\text{m}$) a network of voids was detected. The orientation of these voids (fig. 4.11) corresponds to the hatch orientation of the bulk scan strategy. Table 4.10 and fig. 4.12 show the present porosity in each of the nine unexposed quarters.

Tab. 4.10: Porosity values in the 9 quarters. The nominal porosity of each quarter would be 100 % (assuming all powder particles are removed)

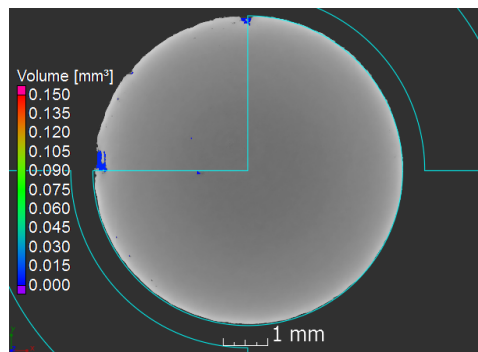
Q1	Q2	Q3	Q4	Q5	Q6	Q7	Q8	Q9
none	0.05 %	0.04 %	0.08 %	0.38 %	0.78 %	0.80 %	2.23 %	5.56 %



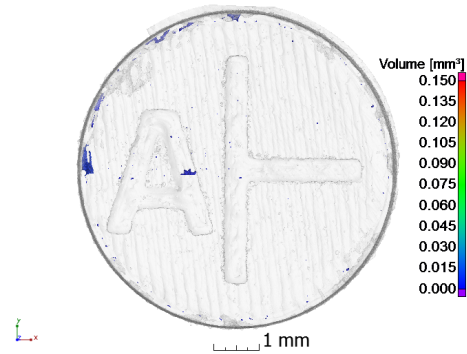
(a) Q4



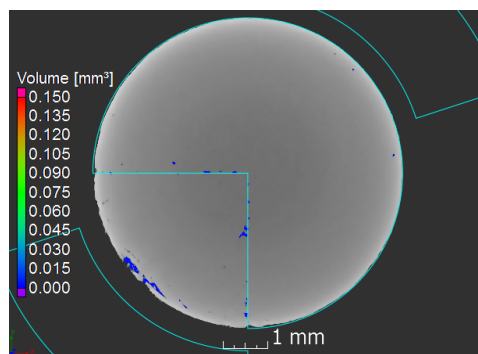
(b) Q4 3D Projection



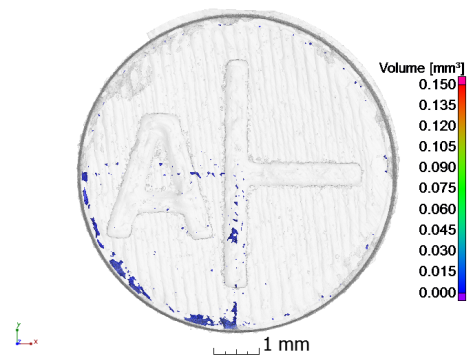
(c) Q5



(d) Q5 3D Projection

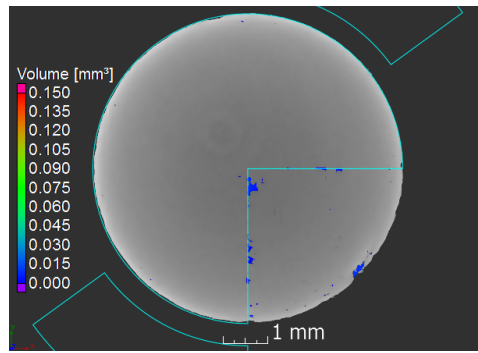


(e) Q6

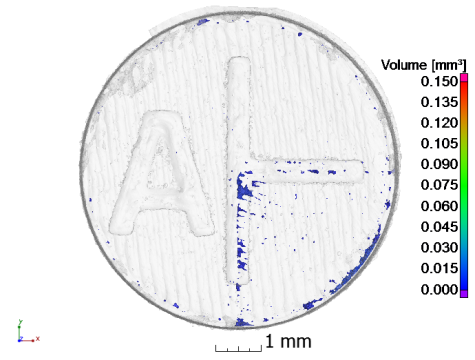


(f) Q6 3D Projection

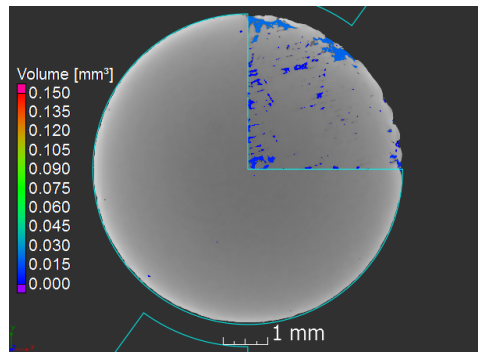
Fig. 4.10: Segmented voids in Q4–Q6 showing only a limited amount of voids formed at the periphery of the non-exposed quarters. Images taken from Ulbricht et al. [38]



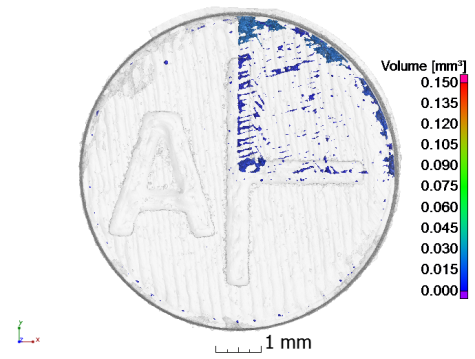
(a) Q7



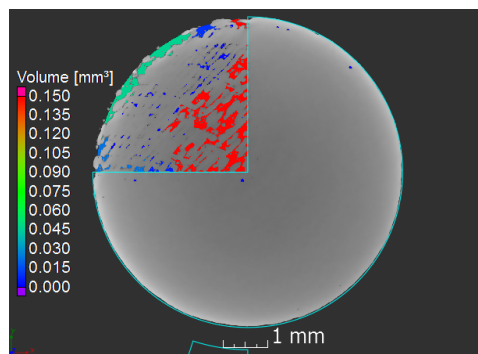
(b) Q7 3D Projection



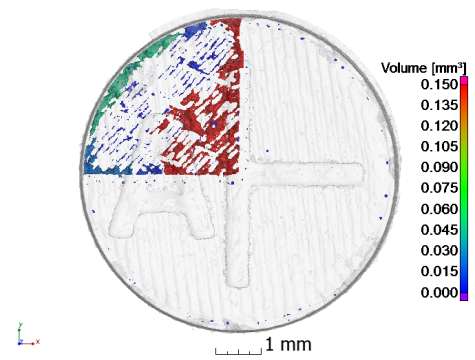
(c) Q8



(d) Q8 3D Projection



(e) Q9



(f) Q9 3D Projection

Fig. 4.11: Segmented voids in Q7–Q9 showing the structured voids. Images taken from Ulbricht et al. [38]

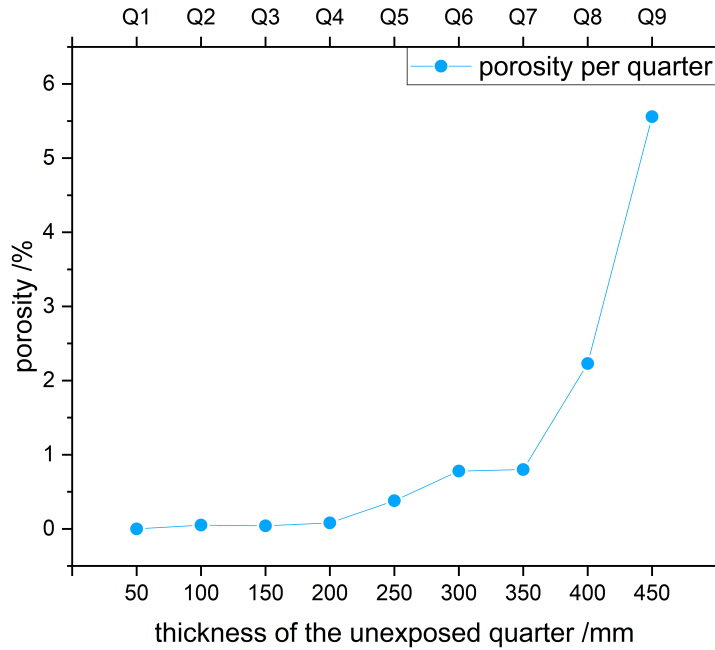


Fig. 4.12: Visualisation of the porosity per quarter given in table 4.10

As shown in fig. 4.12 the porosity remains stable in unexposed quarters of a thickness of up to $250\ \mu\text{m}$, which represents five times of the layer thickness. The porosity increases exponentially from a total layer thickness of $350\ \mu\text{m}$ upwards.

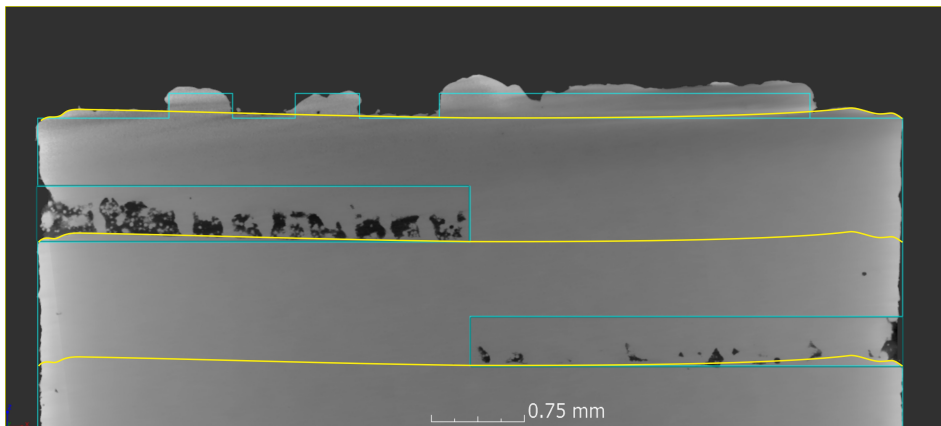


Fig. 4.13: Virtual cut from the mid of the inner cylinder showing the borders of Q9 (upper blue frame) and Q8 (lower blue frame). Yellow lines emphasise the structure of the internal surfaces. Images taken from Ulbricht et al. [38]

Fig. 4.13 shows a virtual cut taken at the middle of the cylinder's cross section. The image shows that the top surface of the cylinder is not even (See blue lines of the

CAD file as nominal reference). The bulk scans are slightly embossed towards the end of the scan tracks. The contour scan tracks are lesser embossed, and fit better to the CAD. In the image a yellow line was drawn from the shape of the cylinder's top surface. This line then was copied and fitted to the inner surface of Q8 and Q9, whose nominal position was marked in the image by the blue rectangles of the CAD file. The shape of the bottom of the inner surfaces of the Q8 and Q9 match pathway of the yellow line. This indicates that the slope of the upper surface is an inherent feature that materialises at every layer during the build job.

4.4 Residual Stress and Porosity in Prisms

In this chapter an experimental way is presented to unravel the two main mechanism for the formation of RS in PBF-LB/M parts: TGM and CSSM (see chapter 1.3). The chapter is based on the paper by Ulbricht et al. [39].

4.4.1 Experimental Details of the Determination of Residual Stress

As described in chapter 3.3.3 two prisms sharing a scan strategy that results in similar solidification shrinkage while featuring a different thermal history were built to unravel the two formation mechanisms of RS in PBF-LB/M. RS were obtained for the mid height build plane in the two specimens. The bulk residual stresses were determined by ND. Measurements were performed at the STRESS-SPEC diffraction instrument [95] at the Maier-Leibniz Zentrum in Garching, Germany. A schematic of the instrument is shown in fig. 2.9 in chapter 3.3.3. The used wavelength used for the experiment was 1.550 \AA . For conventionally produced fcc material measuring the Fe_{311} peak is recommended in literature [91]. This reflection is usually chosen due to the low accumulation of inter-granular stresses. The detector was set to a reflection angle of $2\theta = 90^\circ$ according to the reflection angle of the Fe_{311} peak at the used wavelength.

In a grid of 7×5 measurement positions of the bulk material as depicted in fig. 4.14 the diffraction peaks were measured to map the mid height plane. A gauge volume of $2 \times 2 \times 2 \text{ mm}^3$ was used. The peaks were measured along the three geometrical directions of the prisms, since the principle stress directions correspond to the geometrical dimensions of the prisms. σ_L represents the RS along the prisms' y -direction, σ_T the stress along their x -direction and σ_N along z -direction, which also is the build direction (see fig. 4.14).

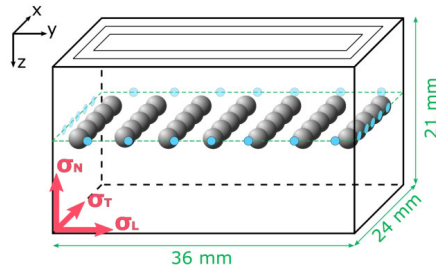


Fig. 4.14: ND measurement positions in the mid height plane

To determine absolute RS values a stress-free reference is needed. A small cube with a size of $3 \times 3 \times 3 \text{ mm}^3$ sectioned from a separate test build job of the $\square \nabla \square$ PtC specimen was used. Due to its size after sectioning by electro discharge machining the cube was regarded as free of type I macro stresses. The stress-free d_0 value was derived the average of the lattice spacing measured in three orthogonal directions along the three edges of the cube.

The contour plot function of the commercial software *Origin 2018* (OriginLab Corporation, Northampton, USA), which is based on the Delaunay triangulation, was used to visualise the results. As mentioned earlier the principal stress components (σ_L , σ_T , σ_N) follow the geometrical dimensions of the prisms (fig. 4.14).

To gain a full picture of the planar residual stress field of bulk compression and surface tensile RS, the ND data were complemented by surface XRD data obtained from laboratory XRD. The XRD data was provided by Maximilian Sprengel of div. 9.4 (Weld Mechanics) of BAM. Data acquisition of the surface using laboratory XRD is described in [39]. The applied XRD technique is only suited to determine the in-plane stress components (*i.e.*, parallel to the surface). The boundary condition that the perpendicular stress component at a surface must be zero is used to in the visualisations of the combined XRD and ND data. The visualisation of the combined ND and laboratory XRD results of the prismatic specimens shows this full field distribution (see fig. 4.15).

4.4.2 Results of Residual Stress Determination

In general, the RS distribution for the two scan strategies show similar distributions for each of the three orthogonal directions (see fig. 4.15). As expected from literature on PBF-LB/M materials, the distribution consist of compressive stresses in the centre and tensile stresses towards the surface. The general distribution of the longitudinal and transversal RS component of the two specimens looks similar, differing only

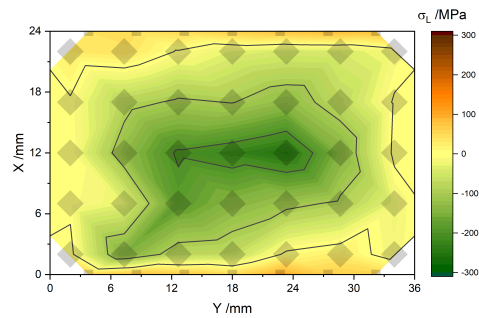
in the absolute values of the RS (see fig. 4.15a and fig. 4.15c for the $\square\blacktriangle$ CtP specimen or fig. 4.15b and fig. 4.15d for the $\square\blacktriangledown$ PtC specimen). The normal RS component of the two specimens (*i.e.*, build direction) displays a completely different distribution in terms of shape and magnitude (see fig. 4.15e for the $\square\blacktriangle$ CtP specimen and fig. 4.15f for the $\square\blacktriangledown$ PtC specimen). This direction also shows the highest magnitude of RS for both specimens. The $\square\blacktriangledown$ PtC specimen has higher compressive stress values for all three orthogonal directions.

The observed RS anisotropy between normal direction and transverse plane direction is also reflected in the determined d_0^{311} -spacing values of the stress-free reference cube. As shown in table 4.11, values of the longitudinal and transversal components are relatively similar to each other, whereas for the normal direction a larger d_0^{311} -spacing value was obtained. For the calculation of the RS the average of the three d_0^{311} -spacing values was used.

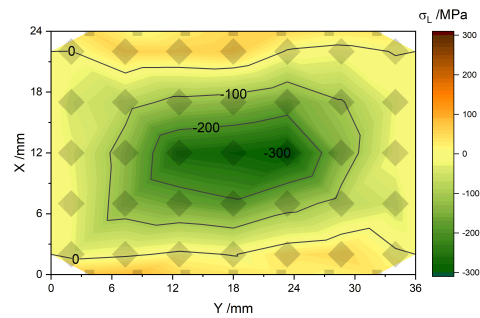
Tab. 4.11: Distribution of orthogonal d_0^{311} -spacing values of the reference cube

Orientation	d -Spacing	Error
Longitudinal	1.074 49 Å	2×10^{-5} Å
Transversal	1.074 48 Å	3×10^{-5} Å
Normal	1.074 93 Å	2×10^{-5} Å

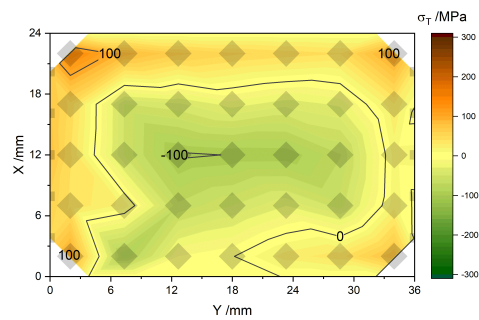
Fig. 4.16 shows line profiles obtained from data taken at $x = 12$ mm. The line profiles reveal that the $\square\blacktriangledown$ PtC specimen is under higher compression in the centre of the specimen than the $\square\blacktriangle$ CtP specimen. Interestingly, tensile stresses near the surface are similar in the two specimen. One would have expected that the higher compression in the centre of the $\square\blacktriangledown$ PtC specimen would be balanced by higher tensile stresses at near the surface. To investigate this imbalance XCT and radiograms were taken of both specimens to analyse correlations between internal stresses and the internal void distribution of the two specimens.



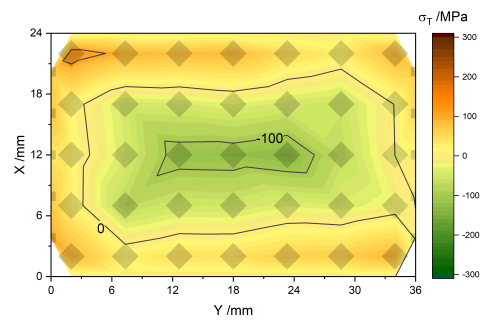
(a)  Longitudinal RS component for CtP border fill strategy



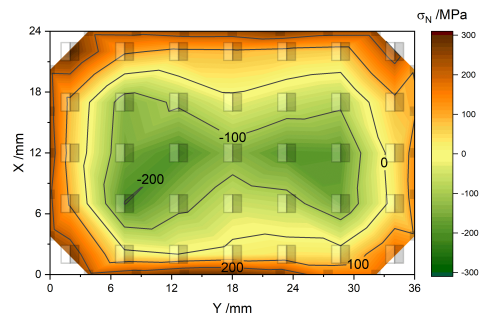
(b)  Longitudinal RS component for PtC border fill strategy



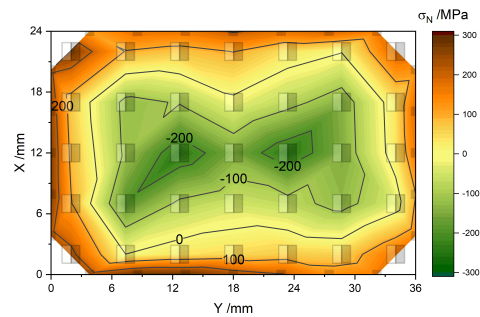
(c)  Transversal RS component for CtP border fill strategy



(d)  Transversal RS component for PtC border fill strategy



(e)  Normal RS component for CtP border fill strategy




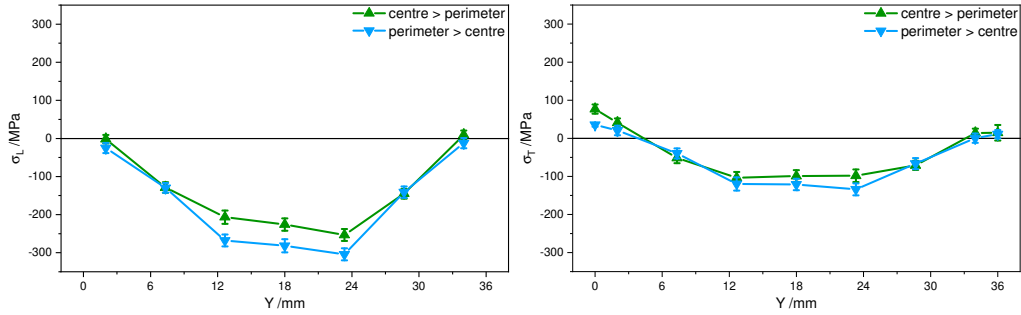
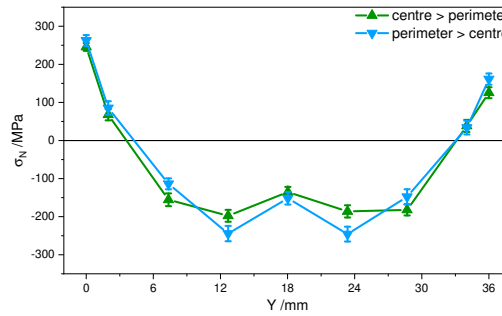
(f)  Normal RS component for PtC border fill strategy

Fig. 4.15: Comparison of RS maps of the two scan strategies including results from laboratory X-ray diffraction at the surface (*The big semi-translucent squares in the bulk represent the almost cubic ND gauge volume (orientated differently for different stress components), whereas the small semi-translucent squares at the edges represent the laboratory X-ray measurement positions*). Images taken from Ulbricht et al. [39]



(a) Longitudinal RS component at $x = 12$ mm (b) Transversal RS component at $x = 12$ mm



(c) Normal RS component (= build direction) at $x = 12$ mm

Fig. 4.16: Line scans in both samples for all three orthogonal directions using the combined data from ND and laboratory XRD. Images taken from Ulbricht et al. [39]

4.4.3 Experimental Details of the Determination of the Mesostructure

The reference cube was analysed by XCT to exemplarily determine the local defect distribution in the specimen. The commercial CT scanner GE v|tome|x 180/300 (GE Sensing & Inspection Technologies GmbH, Wunstorf, Germany) was used to acquire the XCT data. The used acquisition parameters are given in table 4.12.

Tab. 4.12: Acquisition parameters for the scan of the stress-free cube

Voltage	Current	Projections		Filter	Voxel Size
		N ^o	Time		
150 kV	70 μ A	3000	3 s	2	3 μ m

Also the 3 mm thick plane of the twin $\square \nabla \square$ PtC specimen was tomographed. The stress-free reference cube was glued to the plate to enable the analysis of the corner sections. The plane itself was cut into a grid of cubes before the XCT acquisition, which can be seen in fig. 4.18. The XCT acquisition was performed at the custom-made XCT scanner [98] achieving a voxel size of $13\mu\text{m}$. The XCT parameters are given in table 4.13.

Tab. 4.13: Acquisition parameters for the scan of the grid of stress-free cubes

Voltage	Current	Projections			Filter	Voxel Size
		N ^o	Time	Average		
210 kV	$90\mu\text{A}$	3000	2 s	5	1.0 mm Cu 0.25 mm Al	$13\mu\text{m}$

In addition, radiograms of the two specimens were made by Mr Marcel Grünwald of div. 8.3 (Radiological Methods) of BAM (see fig. 4.18). The images were made using radiography films and then digitalised. After digitalisation a $50\mu\text{m}$ pixel size was achieved.

4.4.4 Results: Defect Characterisation

The stress-free reference cube was cut from a corner. Therefore, it represents an area where the laser was turned off during repositioning. It was reported in literature that voids the end of a scan track is prone to void formation [25]. The XCT results in fig. 4.17 reveal a network of defects at the location where the laser started and ended, as well as between the hatches. Since the same scan vector was used on each hatch and each layer, the projection of defects into one plane (fig. 4.17c) reveals the lack of fusion between neighbouring hatches. As reported in literature [103, 104] alternating the orientation of scan vectors between layers prevents the formation of LoF defects. Since the effect of shrinkage on RS was the subject of this study, scan vectors were not altered between layers to magnify the effect of shrinkage induced RS.

The largest defects were situated close to the edge of the sample (fig. 4.17b-c). A total porosity of 0.28 % was observed.

The defect distribution between hatches is not visible in the XCT data of the full plate (see fig. 4.17c) due to the reduced resolution of the scan. Nonetheless, an accumulation of voids at the laser's turning points is visible in the figure. Also the

radiogram of the ∇ PtC specimen shows an accumulation of voids at the laser's turning location. Fig. 4.18c shows that voids are larger at the corner of the specimen than in the bulk. In the radiogram of the \blacktriangle CtP specimen at no voids were detectable at the pixel size of $50\ \mu\text{m}$.

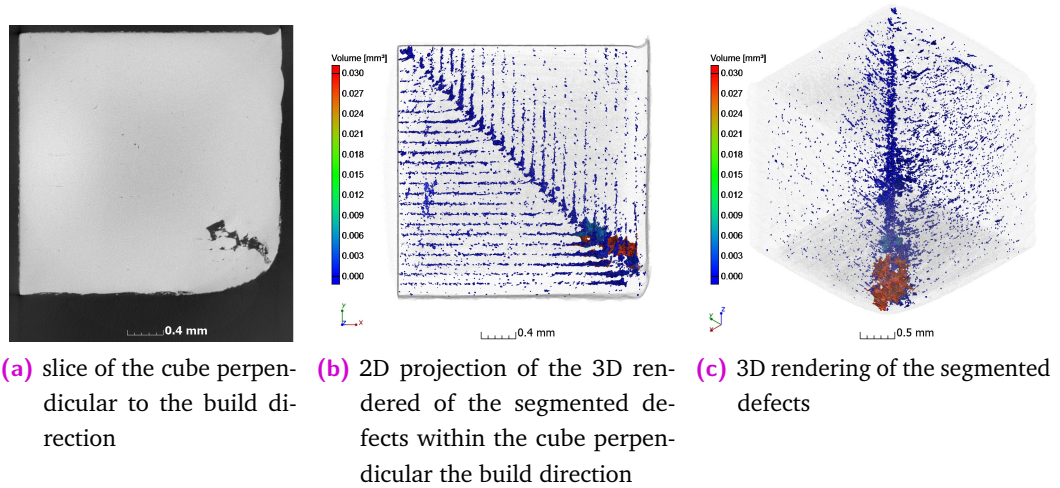
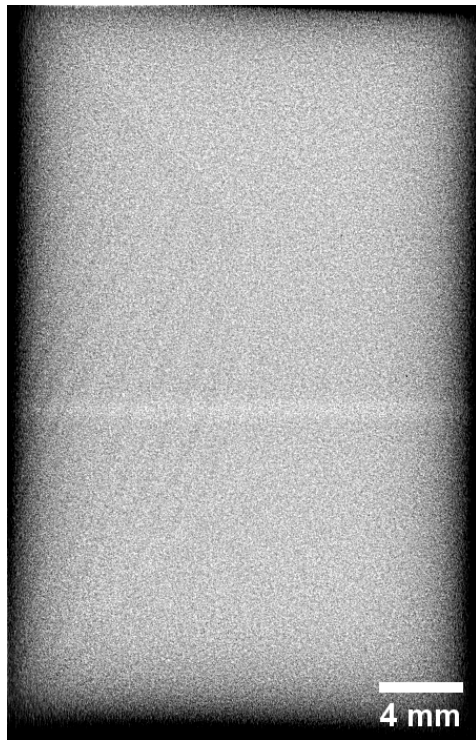
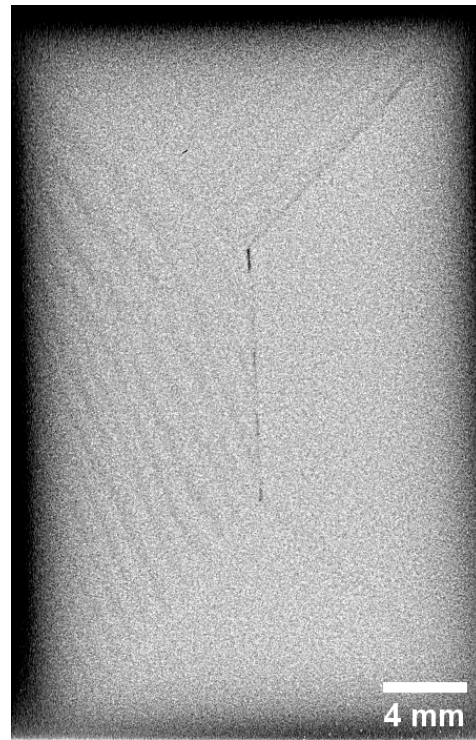


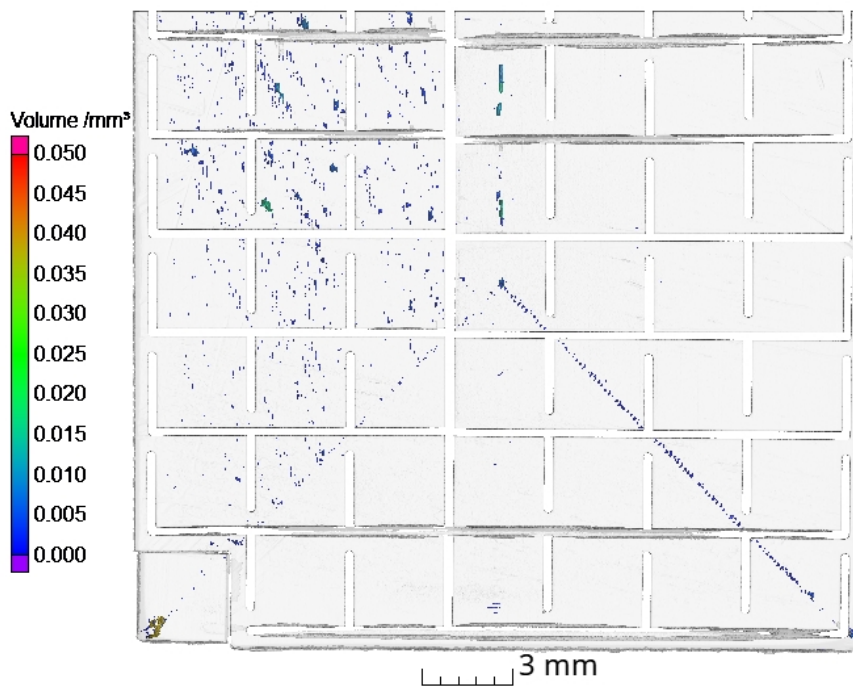
Fig. 4.17: XCT reconstructions of the ND reference cube sectioned from a twin ∇ PtC specimen. Images taken from Ulbricht et al. [39]



(a) radiogram of the $\square\blacktriangle$ CtP specimen



(b) radiogram of the $\square\blacktriangledown$ PtC specimen



(c) 3D rendering of the segmented defects in the 3 mm thick plane of a twin $\square\blacktriangledown$ PtC specimen

Fig. 4.18: Comparison of the radiograms and XCT emphasising the internal defect structure of the prisms. In both bottom corners of the specimen an accumulation of voids was observed.

4.5 Interlink between Porosity and Damage from Mechanical Loads

In the introduction the three main differences between conventionally manufactured (in this case hot rolled) and objects manufactured by the PBF-LB/M process were described: they are microstructure, RS, porosity. In chapter 4.1 the porosity of the PBF-LB/M process based on standard machine parameters was studied. This chapter assesses the influence of the microstructure and the initial porosity on damage formation from mechanical loads. Therefore, the void distribution of creep specimens at different stages of the mechanical testing was analysed.

The experiment consisted of two parts. The first part yielded the assessment of the different failure mechanisms between hot rolled and PBF-LB/M/316L creep specimens under the same mechanical loads. Therefore, the ruptured hot rolled creep specimen was compared to the PBF-LB/M/316L creep specimen K04. Based on the results of this experiment a further experiment was performed to assess the void and rupture formation of PBF-LB/M/316L creep specimens. Therefore, for the second part of the experiment two PBF-LB/M/316L creep specimens were scanned by XCT in their initial condition before creep testing (t_0), at a defined interruption time (t_i) and in their broken state following the creep tests (t_u). The XCT data of these three states for each specimen were analysed to assess the evolution of damage due to void formation.

4.5.1 Experimental Details

The studied creep specimens were extracted from the same batch of tower specimens as the tensile specimens studied before. Therefore, the initial porosity of the creep specimen was expected to be comparable to the tensile specimens. Due to the larger voxel size from this XCT measurements (creep specimens: $10\mu\text{m}$; tensile specimens: $5\mu\text{m}$) only pores larger than a diameter of $20\mu\text{m}$ could be detected in the creep specimens. The initial porosity of the creep specimens, which were inspected prior to mechanical testing, is found to be less than 0.001%. The XCT data from a PBF-LB/M/316L creep specimen (K04) and a hot rolled creep specimen were compared in their broken state following creep testing under the conditions specified in section 3.3.1, table 3.5 on page 35). The measurements were performed on the commercial XCT scanner GE V|tome|x 180/300 (GE Sensing Inspection Technologies GmbH, Wunstorf, Germany). A voxel size of $10\mu\text{m}$ was achieved,

enabling the determination of voids with a diameter above $\sim 20\mu\text{m}$. The acquisition parameters of the XCT scans of the two specimens is given in table 4.14:

Tab. 4.14: Acquisition parameters for the hot rolled specimen and the PBF-LB/M/316L specimen K04 in their broken state (The long and short broken part of each specimen were scanned separately)

Voltage	Current	Projections			Filter	Voxel Size
		N ^o	Time	Average		
200 kV	50 μA	2300 (hot rolled short)	2 s	–	0.25 mm Ag	10 μm
		1700 (hot rolled long)				
		3000 (K04 short)				
		2400 (K04 long)				

Remark The different numbers of projections in table 4.14 (and table 4.16) are the result of the precision with which the specimen was adjusted to the rotation centre of the manipulation stage. The projection number of the shorter part of the broken K04 specimen is even larger, because the specimen’s threaded ending was part of the projected image. Thus, requiring even more projections were required to cover the wider object.

Aside from the number of projections the same acquisition parameters as for the hot rolled specimen and K04 were used to scan the initial (t_0) and interrupted (t_i) state of the PBF-LB/M/316L creep specimens K01 and K05 (see table 4.15). To scan the specimens at a voxel size of $10\mu\text{m}$ five vertically stacked scans were required to cover their whole length. Positioning of the XCT’s manipulator stage and merging of the five 3D volumes into one was performed automatically by the machine’s control software. The same custom-made XCT scanner as described in chapter 4.1 was used to scan the specimens K01 and K05 in their broken state (t_u). The same voxel size of $10\mu\text{m}$ was used to enable comparability of this data to the data acquired by the GE XCT scanner. This scanner’s control software does not include automatic merging of the five 3D volumes. Therefore, open source image manipulation software *Fiji* [87] was used to manually merge the 3D volumes of the scans.

Tab. 4.15: Acquisition parameters for K01 and K05 in the before and intermediate state

Voltage	Current	Projections			Filter	Voxel Size
		N ^o	Time	Average		
200 kV	50 μA	2600	2 s	–	0.25 mm Ag	10 μm



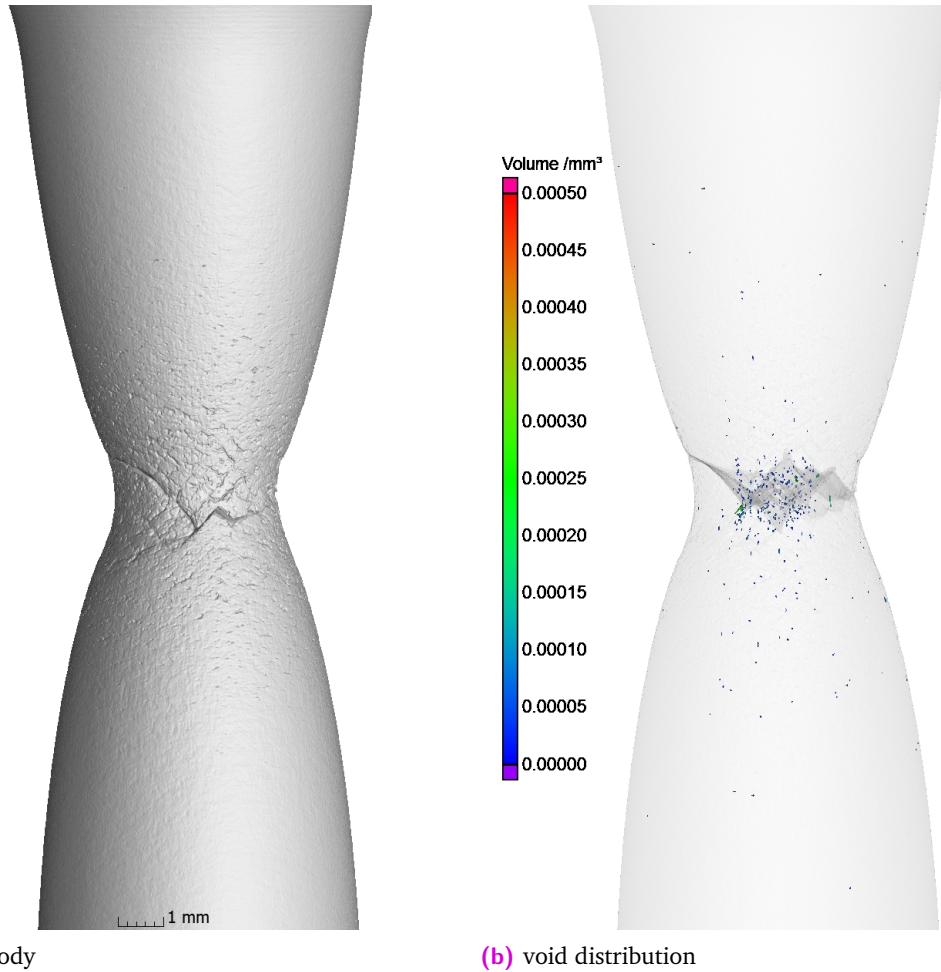
Fig. 4.19: Combined image showing the four studied creep specimens. Photographs of the PBF-LB/M/316L specimen K01 and the hot rolled specimen A5.12 were taken after the XCT scans when the two specimens were already cut for further analysis. Original images provided by Luis Ávila.

Tab. 4.16: Acquisition parameters for K01 and K05 in their broken state (The long and short broken part of each specimen were scanned separately)

Voltage	Current	Projections			Filter	Voxel Size
		Nº	Time	Average		
210 kV	70 μ A	2100 (K01 short)	2 s	5	1.0 mm Cu 0.25 mm Al	10 μ m
		2100 (K01 long)				
		2250 (K05 short)				
		2100 (K05 long)				

4.5.2 Results

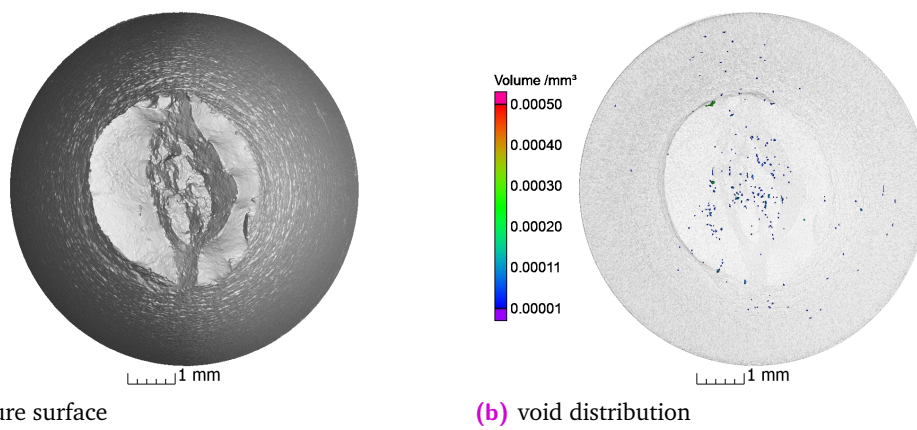
At first, the hot rolled and the PBF-LB/M/316L creep specimens are compared in the broken condition. In the second part of this result section a more detailed analysis of two PBF-LB/M/316L creep specimens under two specific creep loads are compared before the creep testing, at a load-controlled specific interruption time and after the creep tests. Fig. 4.20a shows the rendered and virtually merged parts of the broken hot rolled creep specimen. The rupture occurred near the top side of the specimen (see fig. 4.19). The hot rolled material shows the typical necking due to plastic deformation [67] near the rupture location. Also at the surface near the rupture, smaller surface cracks can be observed. Fig. 4.20b shows the internal void distribution. Only very small voids ($V < 0.0003 \text{ mm}^3$) were observed near the rupture location. Also they occur mainly in the centre of the cross section (see also fig. 4.21b).



(a) full body

(b) void distribution

Fig. 4.20: 3D rendering of the broken hot rolled creep specimen. The two parts were virtually merged.



(a) rupture surface

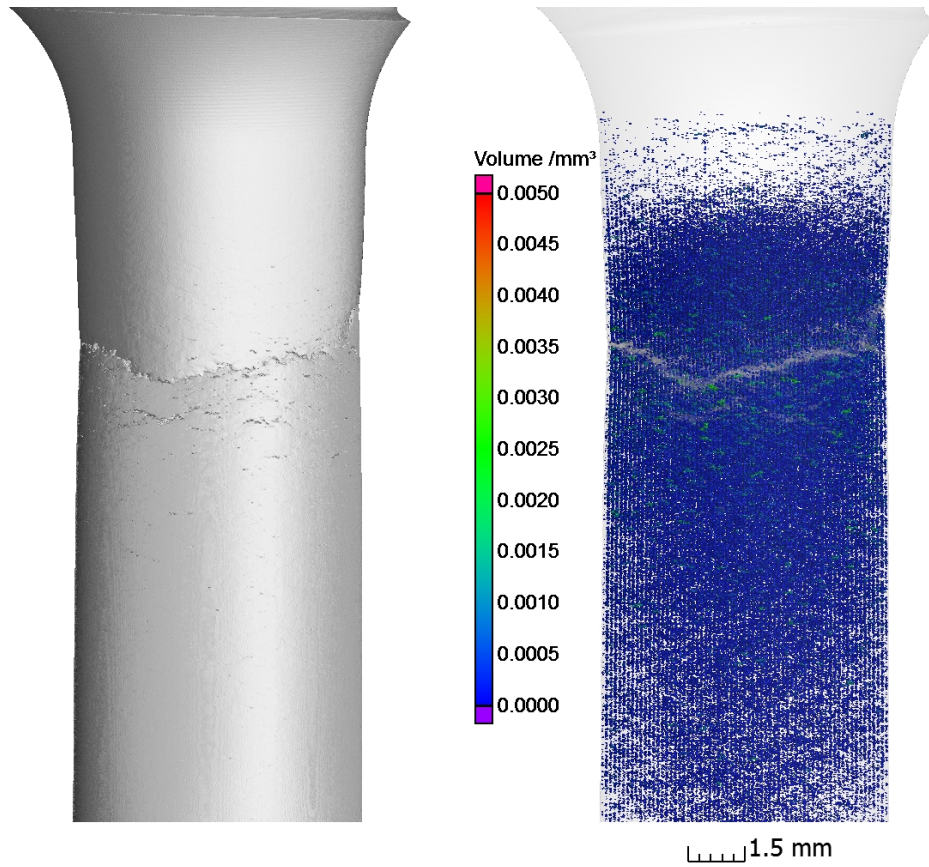
(b) void distribution

Fig. 4.21: 3D rendering of the bottom end of the hot rolled creep specimen. (in respect to the orientation of the virtually merged parts depicted in 4.20)

The rendered and virtually merged parts of the broken PBF-LB/M/316L creep specimen K04 are depicted in fig. 4.22. The rupture occurred near the top end of the gauge length of 60 mm ($\varnothing = 8$ mm). In figure 4.22b a dense structured distribution of voids can be observed. Larger voids (marked in green in fig. 4.22b) are only found near the rupture surface. Secondary cracks can be observed on the surface below the main fracture.

Fig. 4.23a shows the rendered rupture surface of the longer bottom end of the broken creep specimen K04. Fig. 4.23a shows the internal void distribution in the part. As depicted in the image the larger void clusters (marked in green) are evenly distributed within the cross section of the specimen.

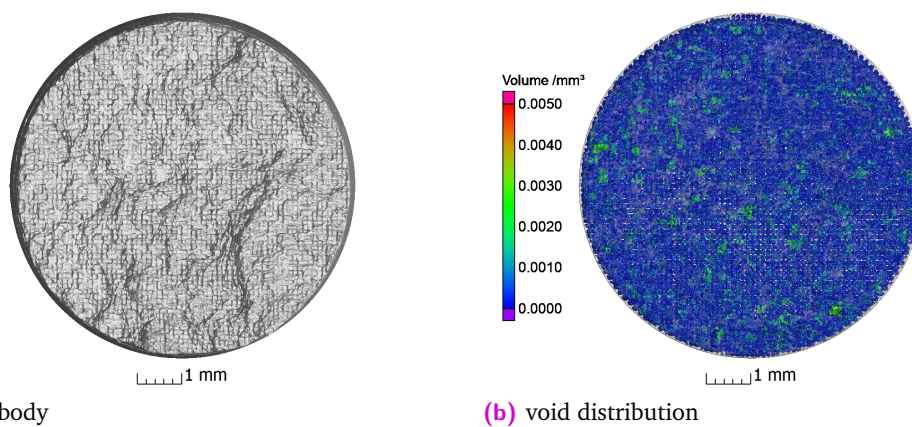
When comparing the PBF-LB/M/316L specimen K04 (fig. 4.22) to the hot rolled specimen (fig. 4.20) a clear difference is observed in the damage and fracture behaviour. The broken hot rolled creep specimen A5.12 shows distinct local necking in the fracture region, which is a feature of ductile fracture. In contrast, the fracture surface of the PBF-LB/M/316L specimen K04 displays almost no necking, indicating a brittle fracture. The comparison of hot rolled and PBF-LB/M/316L creep specimens also shows that the internal damage distribution is different. In the hot rolled specimen only a few spherical cavities near the rupture surface were observed (see fig. 4.20b). In the PBF-LB/M/316L specimen interlinked cavities formed small cracks. These small cracks were observed along the whole gauge length, with increased crack density near the rupture surface (see fig. 4.22b). The distribution of cavities is structured in grids and layers. A selection of different sized voids from the upper broken part of K04 is depicted in fig. 4.24.



(a) full body

(b) void distribution

Fig. 4.22: 3D rendering of the broken creep specimen K04. The two parts were virtually merged.



(a) full body

(b) void distribution

Fig. 4.23: 3D rendering of longer bottom section (in respect to the build direction) of the broken specimen K04. Rupture surface and internal void distribution is shown.

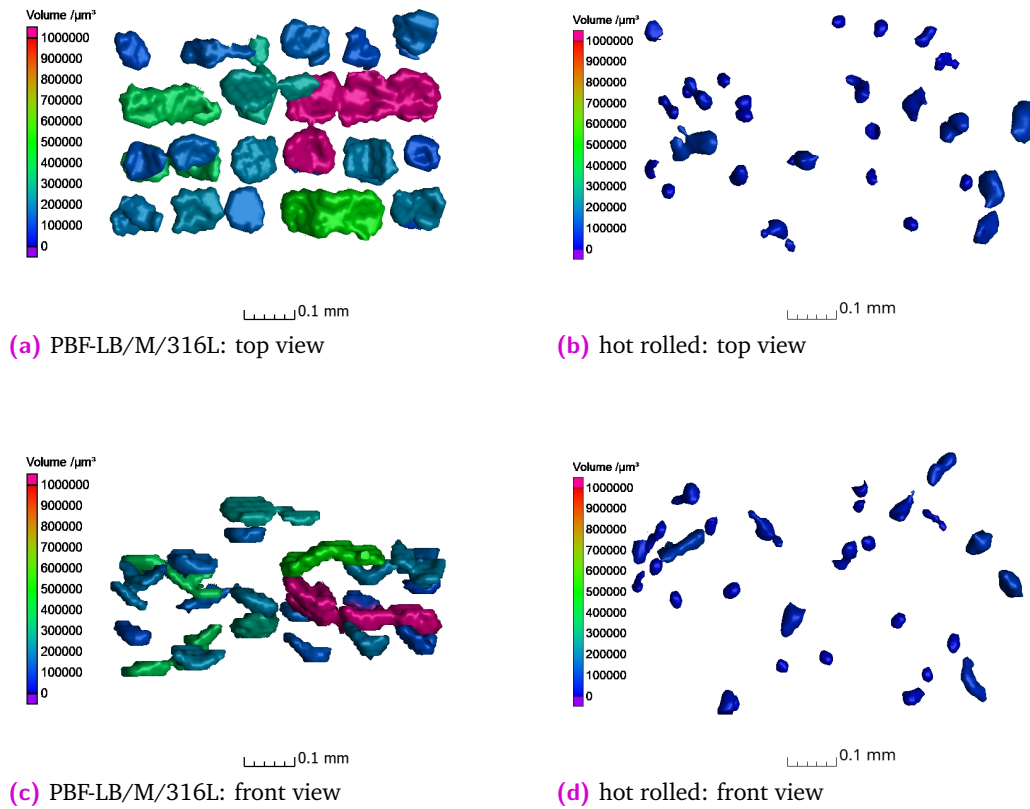
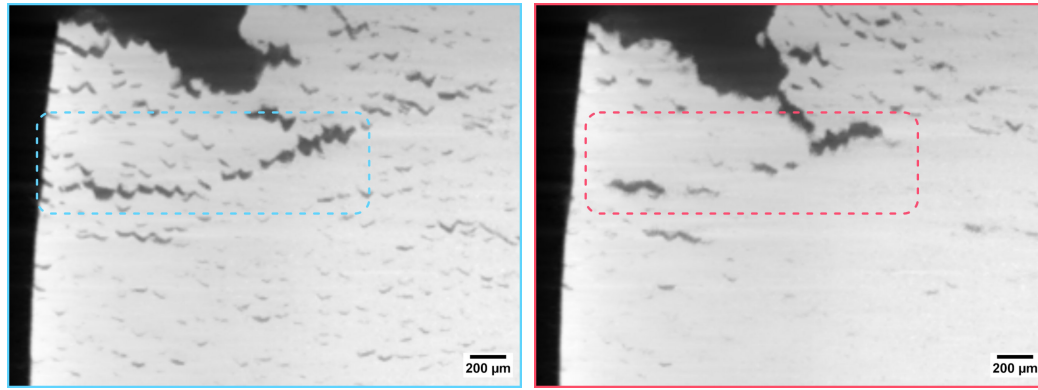


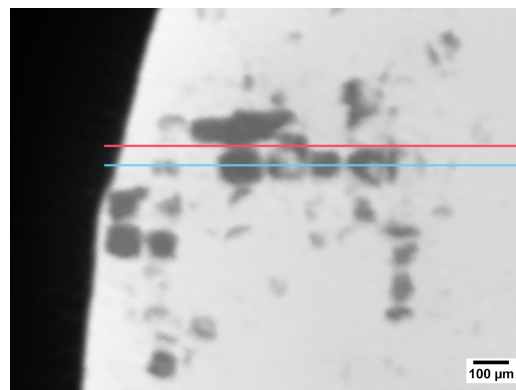
Fig. 4.24: Rendering of several voids. Comparison of PBF-LB/M/316L and hot rolled material at the same scale.

In contrast, in the hot rolled specimen cavities are of a roughly ellipsoidal shape and their distribution does not form patterns. Also, they occur mainly near to the rupture surface (see fig. 4.20b on page 68).

A comparison of the size and shape of the observed crack cavities reveal that they correspond to the shape and size of the grains produced by the PBF-LB/M scan strategy (see fig. 5.8). The meandering stripe scan strategy described in chapter 3.3.1 results in the formation of grains that look square-shaped from the top. The size of such squares is in the range of the hatching distance of $120\mu\text{m}$. A detailed description of the microstructure of this material is given by Charmi et al. [17] and Ávila et al. [67].



(a) front view: virtual cut at the middle of the voids
 (b) front view: virtual cut at the rim of the voids



(c) top view: marking the positions of the vertical cuts shown in (a) and (b)

Fig. 4.25: Virtual cuts of the bottom section of K04 showing crack growth by connecting to clusters

The dashed rectangle in fig. 4.25a and 4.25b highlight that cracks in PBF-LB/M/316L do not exclusively grow from the outside to the centre, but also occur within the specimen. The interconnection of micro cracks form clusters that become macroscopic cracks. Fig. 4.25c shows the position of the two virtual cuts. Many micro cracks can be observed in fig. 4.25a. Here, the virtual cut was placed at the centre of the voids. Much lesser micro cracks are observable in fig. 4.25b, where the virtual cut was placed at the rim of the voids.

A much lower quantity of pores was detected in the unloaded creep specimen than in the tensile specimen due to the different voxel size of the XCT measurements (creep: $10\ \mu\text{m}$, tensile $5\ \mu\text{m}$).

Remark It should be noted that the reconstruction of the whole gauge length of the creep specimen is a result of several vertically stitched data sets

results to achieve the voxel size of $10\mu\text{m}$. The same XCT scanner using the same parameters was used for the scans of all heights. Due to internal fluctuations in the X-ray source and the detector during and between measurements, the grey values of the reconstructed volumes differ slightly from each other (see fig. 4.29d). This influences the segmentation quality slightly at the regions where volumes were stitched together (see fig. 4.26c and fig. 4.29c).

Before the test a very low porosity was observed in the gauge length of K01. In fact only 37 voids were detected at a voxel size of $10\mu\text{m}$ (see fig. 4.26a and fig. 4.27a). Considered that the diameter of the observed voids was about $60\mu\text{m}$ the specimens can be regarded as broadly free of any defects (Porosity $< 0.001\%$). At the interruption of the creep test at $t_i = 143\text{ h}$ additional voids were detected, resulting in a observed total of 105 voids. XCT acquisition parameters as well as post-process data treatment and analysis methods were the same for the two states (t_0 and t_i). The additional voids appear homogeneously distributed through the height of the specimen. Fig. 4.28 shows the 3D rendering of the largest void found in K01 at t_0 and t_i . At t_i a slight deformation of the void's shape is observed (see fig. 4.28b). This deformation is observed for all voids. After the creep test K01 displays a very localised distribution of internal damage (see fig. 4.26c) close to the rupture surface whereas K05 shows internal damage being distributed over the whole parallel length 4.29c.

In the t_0 state of K05 in the whole gauge volume only 14 voids were detected. The interrupted stage t_i shows a few more pores (24) in the same volume. Figure 4.30 highlights the projected position of the voids. The length and width of the specimen did not change between t_0 and t_i . The virtual combination of the two broken segments from t_u revealed an elongation of the specimen without significant reduction in the specimens diameter (see fig. 4.29c). As listed in table 3.5 on page 35 the total plastic strain (e_p) for K05 is 9.2% , whereas for K01 $e_p = 2.4\%$. The larger applied strain in combination with the presented void distribution in fig. 4.29c are the cause of the elongation.

Tab. 4.17: Parallel length of the creep specimen obtained from XCT data.

	t_0	t_i	t_u
K01	$(60.2 \pm 0.5)\text{ mm}$	$(60.4 \pm 0.5)\text{ mm}$	$(61.7 \pm 0.5)\text{ mm}$
K05	$(60.1 \pm 0.5)\text{ mm}$	$(60.4 \pm 0.5)\text{ mm}$	$(65.6 \pm 0.5)\text{ mm}$

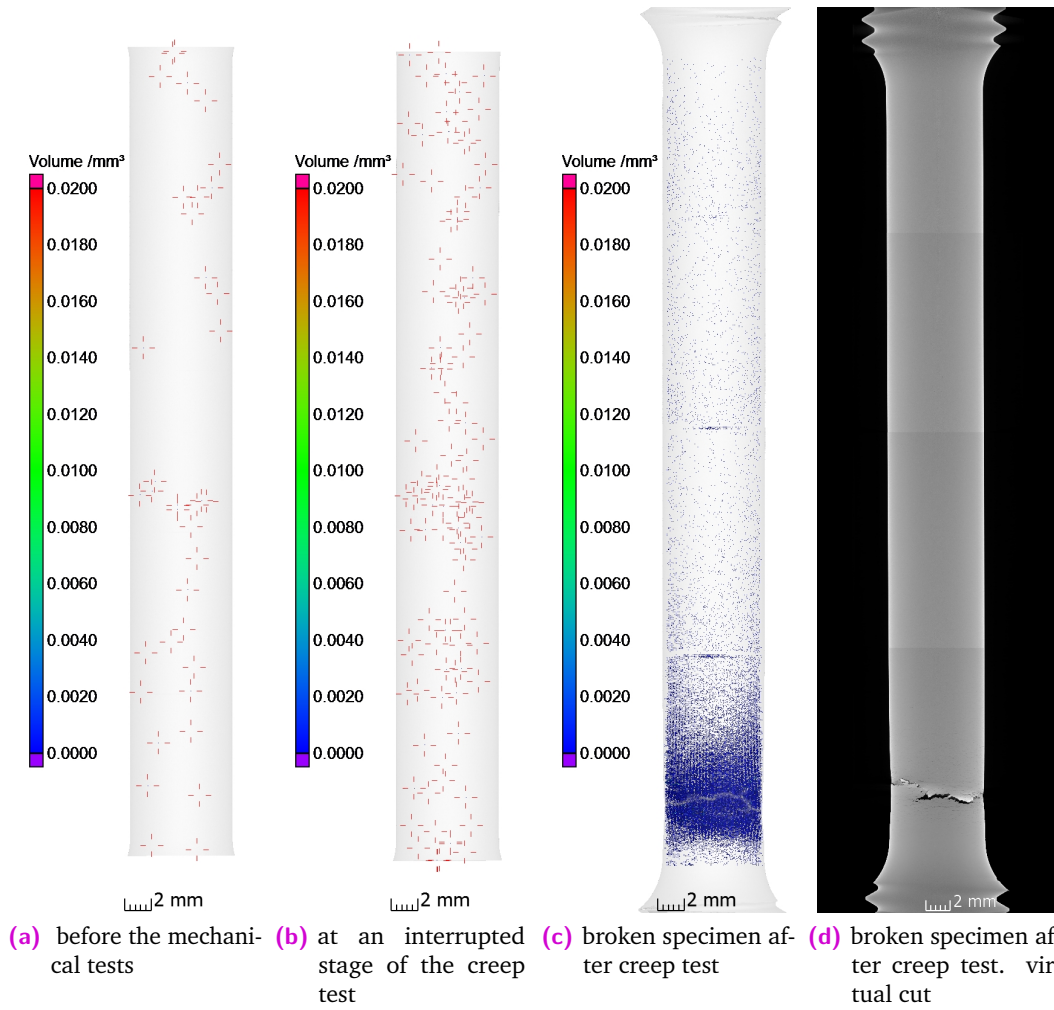


Fig. 4.26: XCT reconstructions of creep specimen K01 at different stages of mechanical testing. The void spatial distribution is shown.

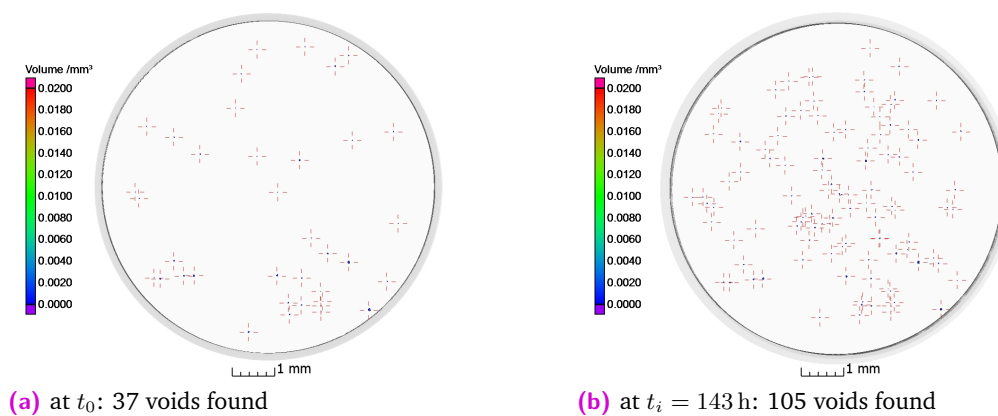


Fig. 4.27: 3D rendering of the void distribution in the creep specimen K01 before the test and at the interrupt time of $t_i = 143$ h

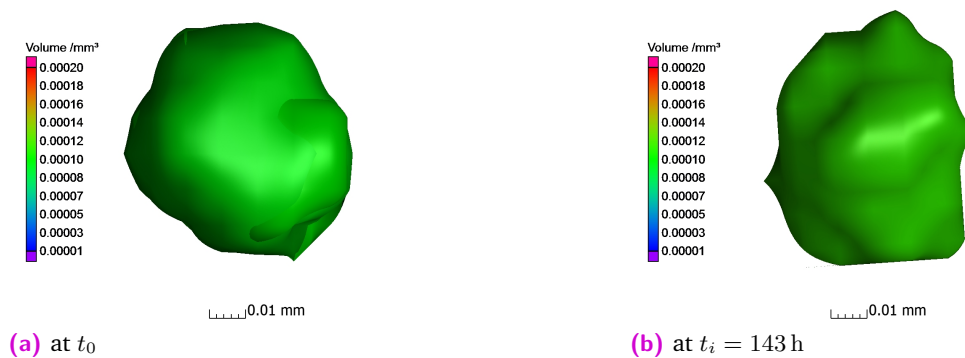


Fig. 4.28: 3D rendering of the biggest void in the creep specimen K01 at t_0 and at the interrupt time of $t_i = 143$ h

Remark The absolute values of the elongation should be taken with a grain of salt, since they depend on the method of combining the two broken parts virtually. The parts were stitched together in such a way that the respective outer surfaces of the top and the bottom part met each other. This choice of stitching leaves a gap in the centre of the rupture surface of the specimens (see fig. 4.26a on page 74 for K01 and fig. 4.29d on page 76 for K05).

Fig. 4.31b displays the structured distribution of the internal cavities. Clusters of cavities that form cracked regions are highlighted in green. The inspection of the rupture surface of this part (fig. 4.31a) reveals that the rupture surface resulted from interlinked cavities. Fig. 4.32 shows that the rupture surface was mostly planar (*i.e.*, the interlink between cavities to form the rupture surface occurred in only a few layers). The observed defect distribution is completely different compared to hot rolled creep samples which show significant necking near the rupture surface (see fig. 4.20) as described for the hot rolled specimen. Fig. 4.30 and fig. 4.31 reveal that the spatial distribution of the voids is structured. Possible coherence between the spatial distribution of voids and the orientation of the PBF-LB/M/316L microstructure are discussed in the following chapter.

The void distribution of a broken tensile specimen, which was tested at the same temperature of 600 °C, was analysed to check whether the structured distribution of cavities also occur in tensile specimens. Fig. 4.33b and fig. 4.35b show that a structured void distribution is also visible in PBF-LB/M/316L tensile specimens. Especially in the centre of the specimen, void formations follows the grain morphology (see fig. 4.35). Closer to the edge of the rupture surface the voids are more deformed than voids located further away. The necking (see fig. 4.33) and the cup-cone-shape of the fracture surface (see fig. 4.35 for the cup-shaped part)

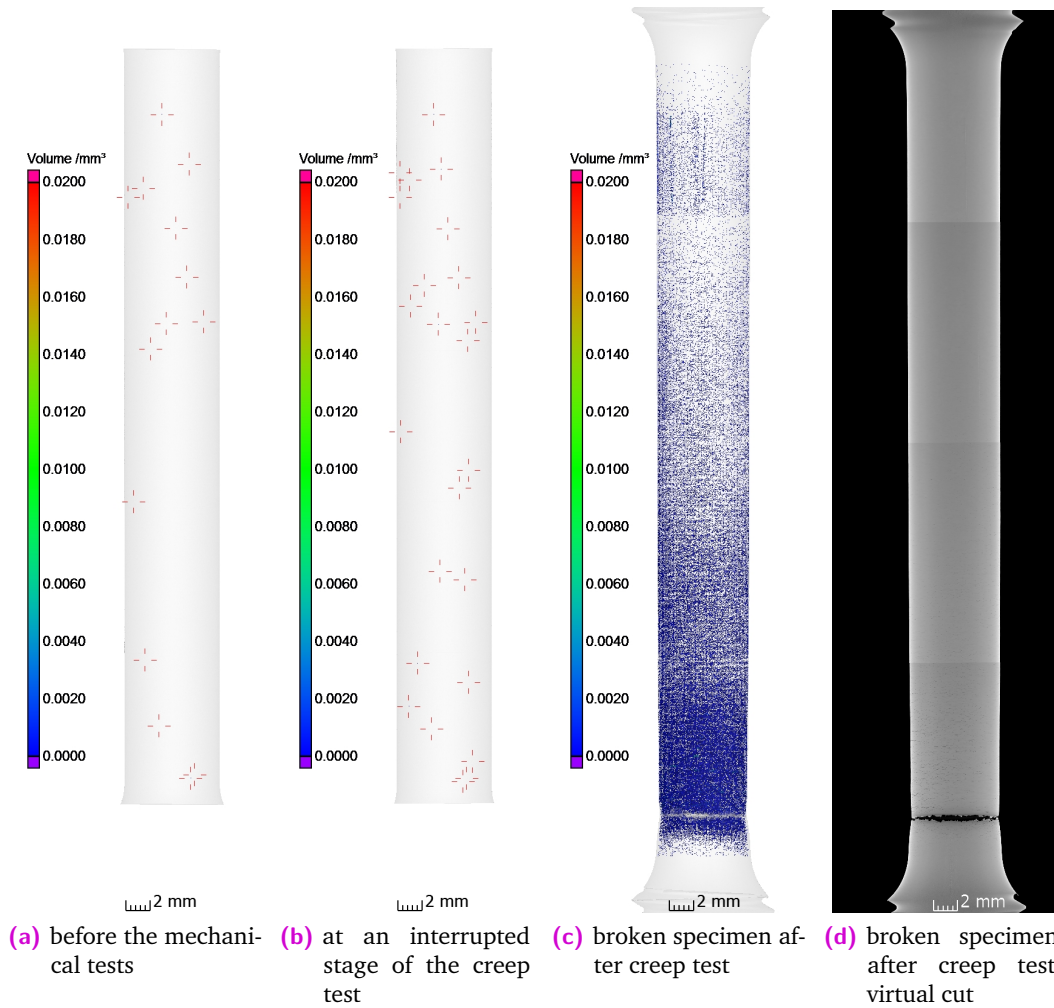


Fig. 4.29: XCT reconstructions of creep specimen K05 at different stages of mechanical testing. The void spatial distribution is shown.

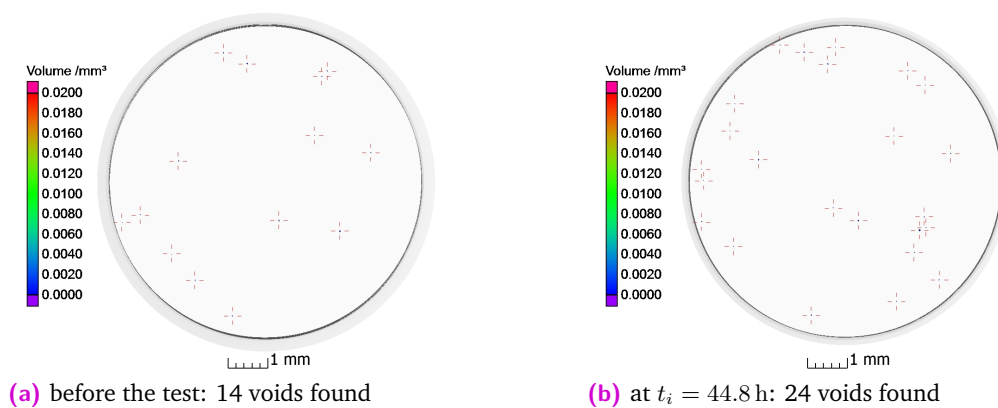
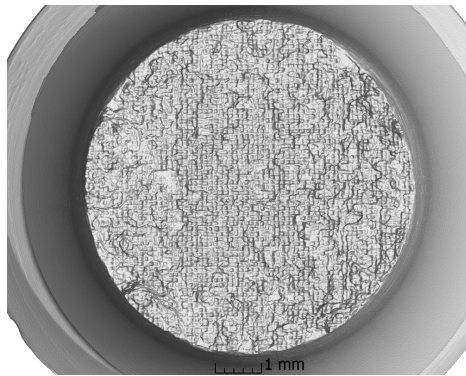
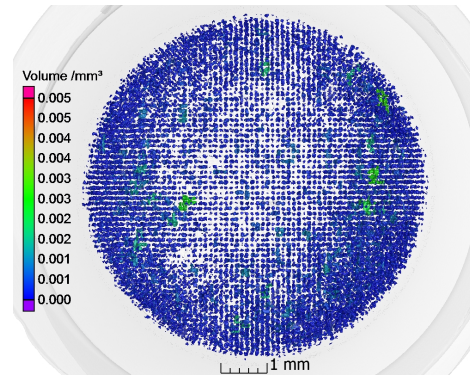


Fig. 4.30: 3D rendering of the void distribution in the creep specimen K05 before the test and at the interrupt time of $t_i = 44.8$ h

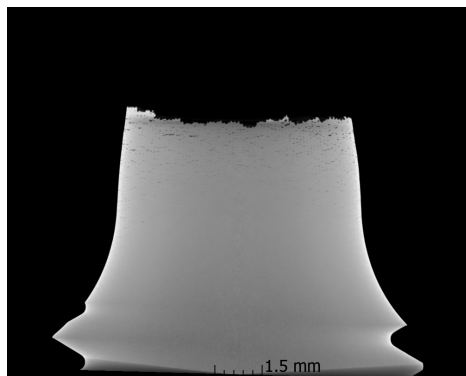


(a) Rupture surface

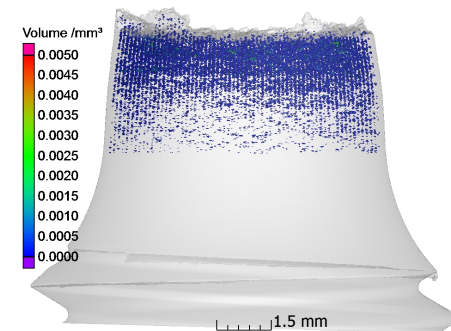


(b) Void distribution

Fig. 4.31: 3D rendering of the bottom part (closest to the build plate) of K05



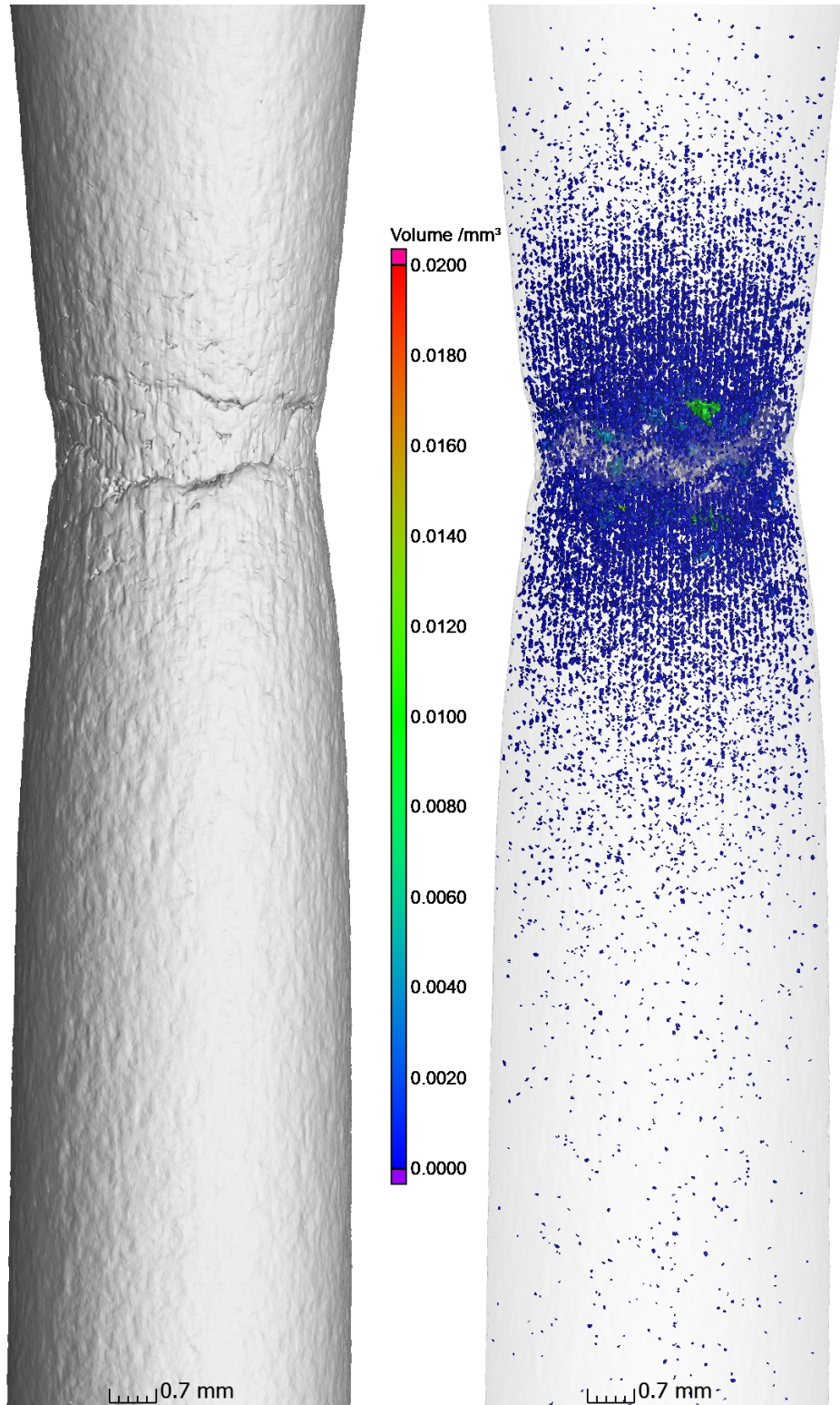
(a) virtual cut at the diameter



(b) segmented voids

Fig. 4.32: XCT reconstructions of bottom part (closest to the build plate) of creep specimen K05. Void distribution in the short part is shown

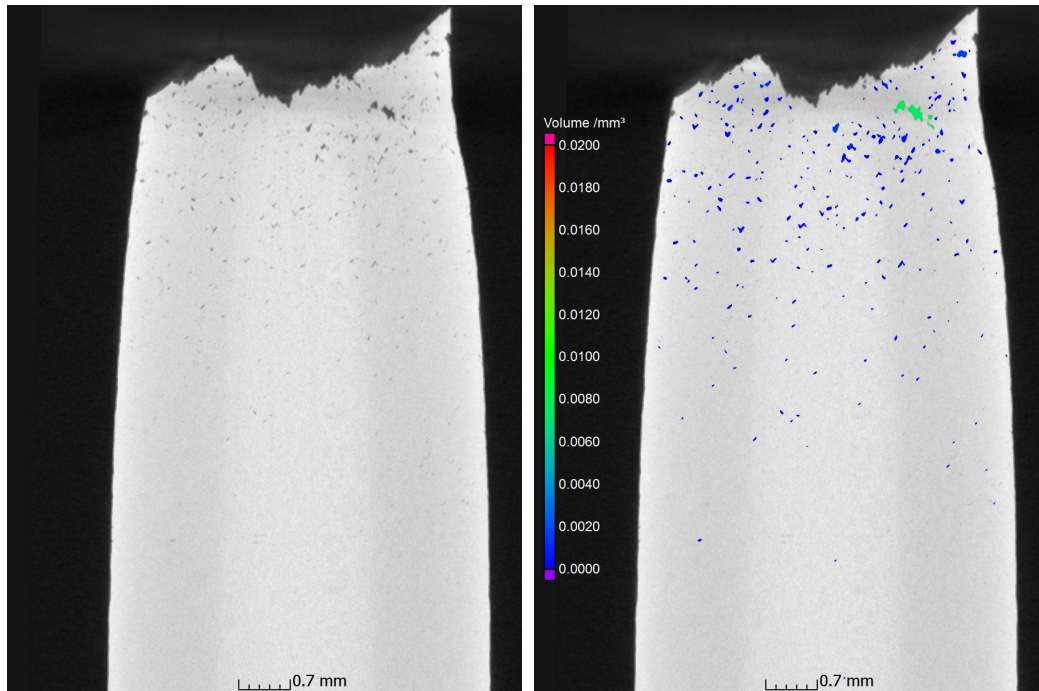
indicated a less brittle fracture than in the creep specimens. This is confirmed by the ductility data from Ávila et al. [67]. Fig. 4.33b shows the void distribution in the broken tensile specimen, whose two parts were virtually merged. In contrast to the creep specimens, which show micro-cracks throughout the whole gauge length, the tensile cracks occur only near the rupture surface. The 3D rendering shown in fig. 4.33a shows a much stronger necking for the tensile specimen than for the creep specimen. A virtual cut through the upper part of the tensile specimen (see fig. 4.34) shows the internal voids structure. Whereas the rupture surface of the creep specimens is rather flat, the rupture surface of the tensile specimen is very rough. Therefore, in the tensile specimen internal voids can be distinguished from voids which are connected to the rupture surface. In fig. 4.34b the non-coloured voids are connected to the rupture surface. (Only closed voids are marked in colors.) The largest void is marked in green. It consists of a connection of small grain-shaped voids. Fig. 4.35a shows the 3D rendering of the upper parts of the rupture surface. In the centre of the surface the grain morphology is visible. Closer to the surface, the rendering shows a smoother surface. Fig. 4.36 shows a virtual cut plane of the tensile specimen's bottom part. The displayed rupture surfaces displayed in fig. 4.36 show a combination of smooth surfaces and interlinked cavities.



(a) full body

(b) void distribution

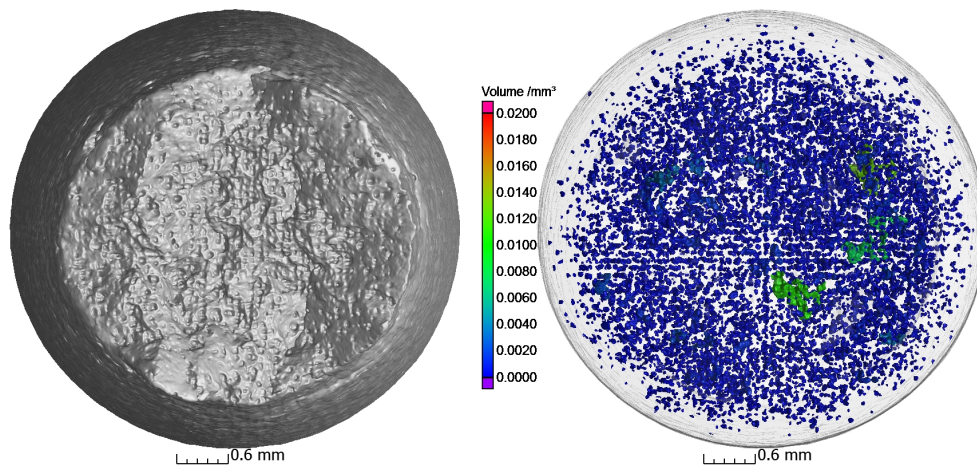
Fig. 4.33: 3D rendering of the broken tensile specimen. The two parts were virtually merged.



(a) Virtual cut

(b) Virtual cut highlighting the segmented void distribution. Only closed voids were segmented.

Fig. 4.34: Virtual cut at the diameter of the bottom part.



(a) full body

(b) void distribution

Fig. 4.35: 3D rendering of the bottom part's rupture surface.

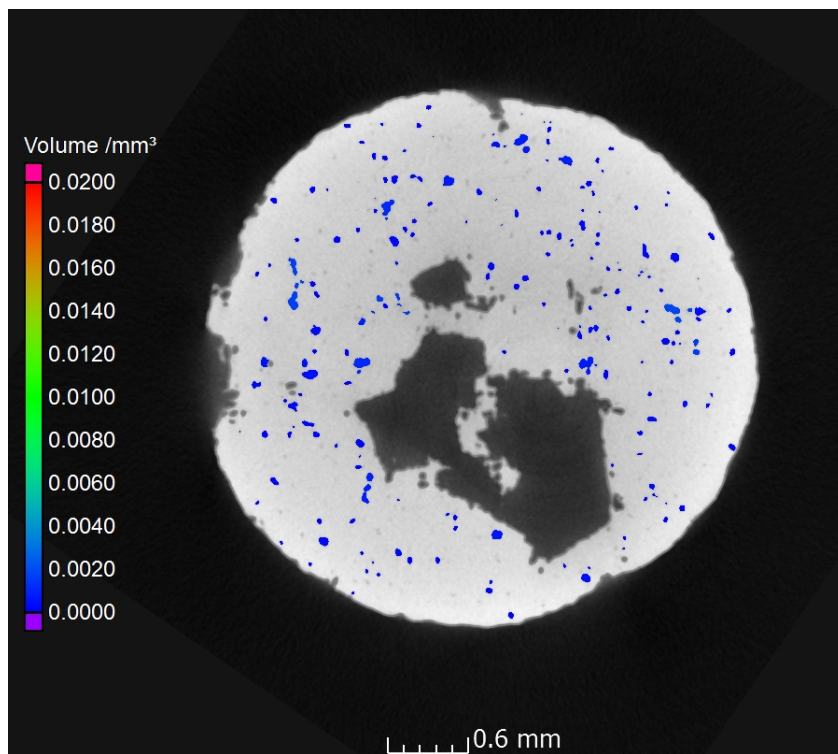


Fig. 4.36: Virtual cut of the bottom part of the fractured tensile specimen. Segmented voids are closed voids. Non-segmented voids are open to the rupture surface.

Discussion on Defect and Residual Stress Formation

” *You can tell you’ve found a really interesting question when nobody wants you to answer it.*

— **James S. A. Corey**
(The Expanse: Nemesis Games)

Based on the presented results this chapter discusses the influence of production process parameters onto void formation in PBF-LB/M/316L. Furthermore, it is revealed how the formation mechanisms of residual stress determine the magnitudes of the residual stress distribution in PBF-LB/M/316L. Finally, the correlation between microstructure and damage formation in this material is discussed.

5.1 Why to Focus on Void Formation?

Void formation is inevitable to PBF-LB/M components as described in chapter 1.3.1. As listed in the introduction, Hojjatzadeh et al. [27] name four typical mechanisms that can lead to pore formation in PBF-LB/M: “pore transfer from feedstock powder [28], instability of depression zone during printing process [25], vaporization of volatile elements [29], gas precipitation [30]”. Aside from freedom of design weight reduction is one of the key advantages of AM metallic parts. The reduction in weight goes hand in hand with building structures containing just enough material to bear the expected external loads and fulfil the needed safety margins. This increases the effect of internal voids on the prediction of the service life.

So, for service life prediction of PBF-LB/M parts, it is essential to distinguish voids from potential defects. As defects one meant voids whose shape, size, orientation and/or position in the component can diminish the service life of the component. An ellipsoidal shaped pore of an equivalent diameter of $100\ \mu\text{m}$ might be a negligible void in a rod of a diameter of 1 cm if the rod is under compression (fig. 5.1a). If the rod is under tension, then the orientation of the ellipsoidal pore becomes important

to consider. If the sharp edges of such a pore are oriented perpendicular to the loading axes, they can serve as crack initiation sites (fig. 5.1b). If its orientation is parallel to the loading axes it could be a negligible void (fig. 5.1c). Also the position of voids in the component can differentiate voids from potential defects. A surface-breaking spherical pore in the bespoke rod is more prone to become a crack initiator (fig. 5.1d) than the same pore located in the center of the rod (fig. 5.1e).

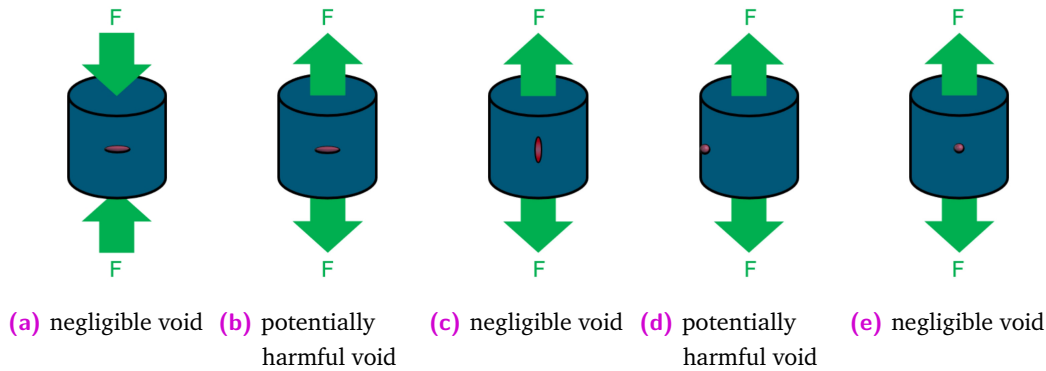


Fig. 5.1: General illustration of the influence of shape, orientation and positioning of voids becoming potential defects respective to external loads

Therefore, due to the reduced material thickness of components made by PBF-LB/M, it is essential to have a full view on the 3D distribution of voids in a component to predict its service life. This is only possible using a 3D ex-situ analysis method such as XCT.

5.2 The Process of Void Formation in PBF-LB/M/316L

The results presented in chapter 4.1 show that specimens built using standard parameters for AISI 316L can be regarded as almost free of voids. Results obtained from SXCT of a small pin extracted from a wall show a lower limit of voids (based on the volume of material examined) in this material at a diameter $2.7\mu\text{m}$ (see fig. 4.4c). This is an interesting result since one could have expected that the number of detected voids is only limited by the used resolution. The used voxel size of $0.438\mu\text{m}$ enabled the detection of voids of a diameter large than about $800\mu\text{m}$. The powder particles are mostly spherical as described by Thiede et al. [70]. The amount of entrapped air in a layer of powder depends on local distribution of powder particles. A complex interaction of the laser with the powder particles has been reported by Foroozmehr et al. [44]. Most of the air in a layer escapes from

the melt pool. The almost perfect spherical shape of voids in the PBF-LB/M/316L specimens produced with optimised process parameters leads to the conclusion that these voids are gas-filled pores. It is most likely that these gas filled pores are keyhole pores. If the process parameters are changed from the optimised values provided by the machine manufacturer, voids will be induced into the solidified material on a global scale. In the High-VED tower of specimen DPK002 described in chapter 4.2 keyhole pores were observed due the unstable melt pool [12] at the large penetration depth of the laser. The fact that the base section was void-free before the remelt suggests that the observed spherical pores do not consist of entrapped air. This observation is important when one considers to locally increase the VED *repair* potential irregularities (*i.e.*, melt entrapped unmolten powder) in underlying layers. The shown results reveal that such measures will require a precise knowledge of size and position of a irregularity. Also the increase of the VED should be well chosen. Otherwise the risk of creating more irregularities in the part in form of keyhole pores is immanent. To solve these issues a more detailed view on the interaction of laser energy and feedstock material is needed.

The results of the Low-VED tower of specimen DPK002 show that a reduced VED caused small voids at the intersection of the scan tracks of odd and even layers since the depth of the melt pool is not sufficient to remelt the subjacent layer and form a void-free bonding with the current layer of feedstock powder (as depicted in the bottom half of fig. 4.7 on page 50). Additionally, to these small voids larger LoF voids form locally as depicted in fig. 4.7. Entrapped unmolten feedstock powder particles are visible in fig. 4.7. This proves the inability of the laser illumination of superjacent layers to melt these powder particles because of the reduced melt pool depth due to the reduced VED.

LoF void formation was studied in a systematic way in specimen DPK003. The VED was kept at the optimised process parameter values given by the PBF-LB/M machine manufacturer. In the specimen the thickness of local areas of the layer was varied to achieve the similar effect of insufficient melt pool depths as in DPK002. The ability of the laser to melt different multiples of the nominal layer thickness ($50\mu\text{m}$) enabled the analysis of the bond between layers. As described in literature [12, 25, 44], the melt pool does not only melt the current layer of powder but also remelts several subjacent layers to form a solid bonding. No LoF voids were observed in the non-illuminated quarters Q1 to Q4. This observation shows that the melt pool is able to form a sufficient bond between powder particles within a thickness of five times of the nominal layer thickness. Therefore, it is possible to melt potential unmolten powder particles of irregularities in subjacent layers even without locally changing the VED. These process parameter setting intrinsically contain a *repair*

function for voids in irregularities in subjacent layers. Also, from the quality aspect of internal porosity, these results lead to the conclusion that an reduced VED (e.g, by increasing the illumination velocity) enables the production of void-free parts in shorter build times.

To discuss the formation of LoF voids in the non-illuminated quarters Q5 to Q9 on-line monitoring signals in terms of thermographic OT is analysed. A comparison of the OT images of the last fully illuminated layer below Q9 (see fig. 5.2a) and of the first fully illuminated layer above Q9 (see fig. 5.2b) reveals a significantly different temperature field at the location of Q9 (see quadrant I in fig. 5.2).

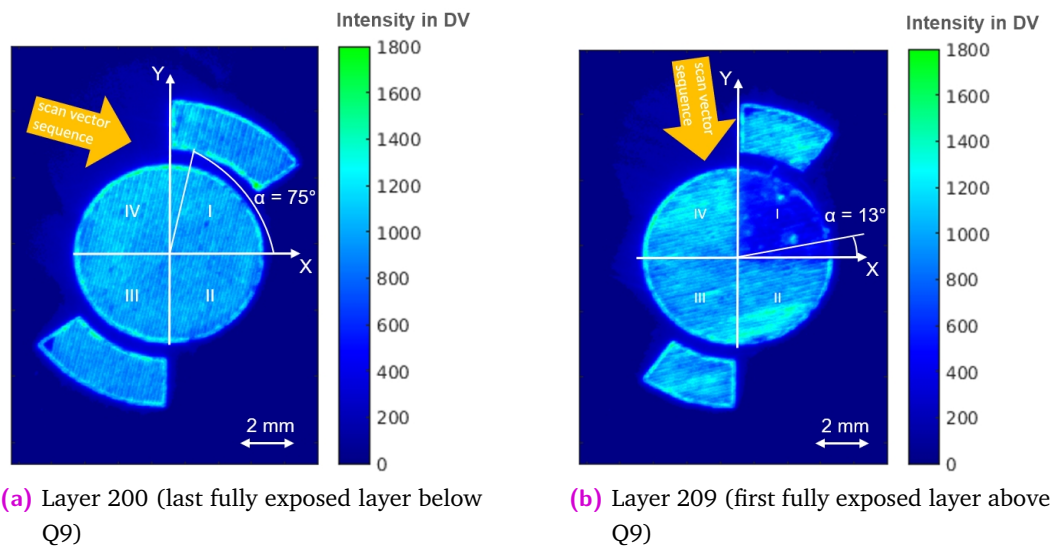


Fig. 5.2: Optical tomography of the laser exposure of the layers below and above the non-exposed quarter Q9. Images taken from Ulbricht et al. [38]

The lower apparent radiated temperatures above Q9 are surprising, since the feedstock powder is usually regarded as an heat insulator [105]. In this case the lower apparent surface temperature seems to show that the laser energy is transmitted to the powder particles below the current layer. Foorozmehr et al. [44] simulated the optical penetration of the light of the laser into 316L powder. In agreement with [43, 46] it is assumed that, aside from absorption, multiple reflections of the beam at the surfaces of the spheric powder particles occur. So, the interaction between laser and powder is a complex combination of transmission, scattering and absorption of the laser energy by particles of the powder *within* the layer. 94 % of the material in Q9 was solidified. This high amount of solidification in Q9 illustrates that energy from the laser was used to melt powder particles throughout the height of Q9. The deeper penetration of the laser into the powder bed resulted in reduced reflected

energy at the position of Q9, which consequently led to a lower signal of radiated temperature observed by the OT camera. Also, voids in the non-exposed quarters are mainly found at the bottom of the quarters (see fig. 4.13 on page 56) due to the insufficient illumination by the laser at deepest parts of the non-illuminated quarters. This result agrees with results from Li et al. [106].

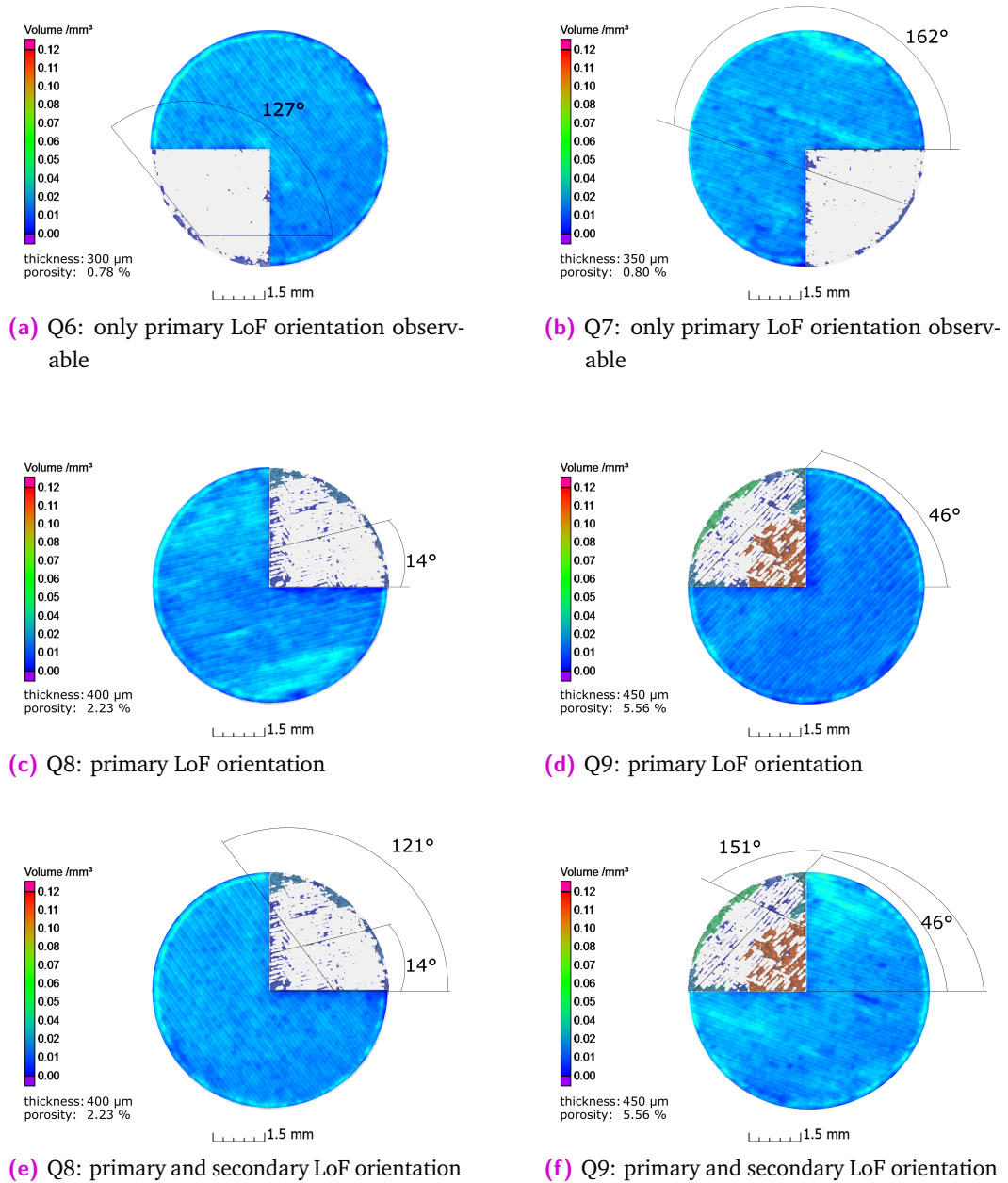


Fig. 5.3: Combination of the void distribution obtained from XCT and hatching orientation obtained from OT. The angles were obtained from the analysis of the XCT data. Images taken from Ulbricht et al. [38]

The combination of OT and XCT results in terms of an overlay enables a better understanding of the formation mechanisms of the observed LoF voids. The layer-wise rotation of the scan tracks by 67° created a unique orientation of the scan tracks for each layer. Therefore, a clear assignment between the orientation of LoF voids and the orientation of the scan tracks (*i.e.*, the vertical position of this layer) is possible. As depicted in fig. 5.3 there is a coincidence between the orientation of the LoF distribution and the orientation of the laser tracks of the first fully illuminated layer above the quarters. A distinct orientation of LoF voids is observable in the XCT data of Q6 to Q9. The powder bed in Q6 consists of six times the nominal layer thickness and one time the nominal thickness of the first fully illuminated layer above Q6. Therefore, the depth of the melt pool is supposed to be in the range of the nominal thickness of seven layers, which is about $350\ \mu\text{m}$. This conclusion is supported by the XCT data of the quarters Q7 to Q9, where the size of orientated LoF voids increased with the thickness of the non-illuminated powder bed. The fact that even in Q9 parts of the non-illuminated quarter were completely transformed into solid material indicates that the melt pool depth is unstable (reaching even deeper areas in the powder bed), and is able to form a void-free bonding of powder particles and underlying material even at depths of larger than $350\ \mu\text{m}$. At deeper regions the melt pool becomes narrower. The combined OT and XCT results shown in fig. 5.3 lead to the conclusion that the melt pool widths from neighbouring scan tracks do not overlap. Surface tension effects (*e.g.*, Marangoni effect [25, 107, 108]) combined with solidification shrinkage have created voids between scan tracks. Surface tension due to the Marangoni effect leads to neighbouring powder particles to be drawn into the melt pool. This creates free inner surfaces, which increase due to material shrinkage. Since these LoF voids were not observed in Q1 to Q3 (*i.e.*, $350\ \mu\text{m}$ layer thickness), the overlap of melt pools from neighbouring scan tracks seems to sufficiently overlap to prevent the formation of LoF voids.

In Q8 and Q9 also a secondary LoF orientation was found to coincide with the orientation of the second fully illuminated layer above the quarters. This results supports the conclusion that the powder bed is thicker than the penetration depth of the melt pool in Q8 and Q9. In addition to the visual agreement of OT and XCT orientations shown in fig. 5.3 table 5.1 shows the determined hatch orientation of the two data sets.

Tab. 5.1: Hatch orientation obtained from XCT and matching OT layer orientation

quarter number	non-exposed height	main LoF angle (XCT)	2nd LoF angle (XCT)	1st layer above (OT)	2nd layer above (OT)
Q6	350 μm	127°	–	127°	59°
Q7	400 μm	162°	–	160°	93°
Q8	450 μm	14°	121°	13°	127°
Q9	500 μm	46°	151°	44°	157°



(a) virtual cut taken 60 μm above the bottom of Q8 combined with OT data of layer 200

(b) virtual cut taken 10 μm below the bottom of Q9 combined with OT data of layer 220





Fig. 5.4: Third orientation of LoF voids obtained from the combination of virtual cuts of the XCT data and OT images from the last fully illuminated layer below the quarters. Images taken from Ulbricht et al. [38]

In fig. 5.4 also a third orientation of LoF voids was detected in the Q8 and Q9. The combination with OT data shows that the hatching orientation of the last layer illuminated fully before Q8 and Q9 matches the orientation of the voids. The angular coincidence shows that this third orientation was not caused by the illumination of subsequent layers. Instead, the surface roughness of the internal surface seems to have served as seeding points for LoF voids. These small inner surfaces caused by roughness allow surface effects of the melt pool to draw powder particles into the melt pool easier and they do not hinder solidification shrinkage. A detailed analysis of Q9 reveals that the third LoF orientation is mainly found at the bottom of the quarter and even slightly below. Therefore, one can conclude that changes to the process parameters which result in smoother surfaces also have the potential to reduce LoF void formation in the bulk material when applied for every illuminated layer. Another interesting result from the XCT data was that the slope of the bulk

surface matches the bottom of the voids found in these quarters. This shows that these raised ends of the bulk scan tracks were also present in all layers during the build. As mentioned in section 4.3 the applied scan strategy used sky writing to prevent changes to the VED at the turn locations of the laser. There, the laser was turned off until the guiding mirrors were positioned for the next track, so that deceleration and acceleration effects can be avoided. Yeung et al. [109] reported that a sudden turning off of the laser causes elevation of the end of scan tracks followed by a dent. These results were also confirmed by simulations of the build process by Khairallah et al. [25]. These explanations correspond to the observations shown in fig. 4.13. Since the hatching orientation was rotated by 67° for each layer the elevated end-sections formed an elevated ring on the cylinder's surface.

5.3 Residual Stresses in PBF-LB/M/316L

As described in the results section, the spatial distribution of the longitudinal and transversal stress component look similar in both specimens. In both specimens the magnitudes of the longitudinal stresses are larger than for their specific transversal component. Both observations can be explained as an effect of the CSSM. The lateral stress components and the orientation of the scan tracks are part of the same plane. The hatches in longitudinal direction are longer than in transversal direction. The constrained shrinkage of hatches parallel to the longitudinal stress direction induces larger compressive internal stresses into the material, than the shrinkage of the shorter hatches along the transversal direction. The effect of this phenomenon can be observed for both specimens. The spatial distribution of the normal stress component, which is parallel to the build direction, differs from the planar distributions in both specimens. The shrinkage of the material in this direction is not constrained. Therefore, the shape of the distribution is mainly determined by the TGM.

The difference between the two specimens is the magnitude of the remaining RS components. In the  PtC specimen larger compressive stresses can be observed than in the  CtP specimen. Interestingly, the tensile stress component near the surface is quite similar in both specimen. This can be explained by the analysis of the radiogram and XCT data. In the  PtC specimen voids were detected at the turning location of the laser. These tend to become larger towards the corner of the specimens. This indicates that these voids serve as initial zones for stress relieving crack formation. In the  CtP specimen hardly any gray value difference between

bulk and the turning location of the laser is observable. Therefore, a much smaller amount of voids or even the lack of voids can be assumed in this specimen.

To support this conclusion the different thermal distributions of the two prisms during the build process were analysed. The build process was accompanied with on-line thermographic imaging by Simon Altenburg of div. 8.7 (Thermographic Methods) at BAM. Details on the thermographic data acquisition can be found in Ulbricht et al. [39]. Fig. 5.5a–5.5b show the maximum apparent temperatures at the mid-height plane. The figures 5.5c–5.5d display the average of 40 illuminated layers around the mid-height plane. This corresponds to the used RS gauge volume height of 2 mm. Fig.5.5 illustrates that the centre of the $\square\blacktriangledown$ PtC specimen shows much higher apparent temperature values than the $\square\blacktriangle$ CtP specimen. Also the turning locations of the laser can be deduced from the images.

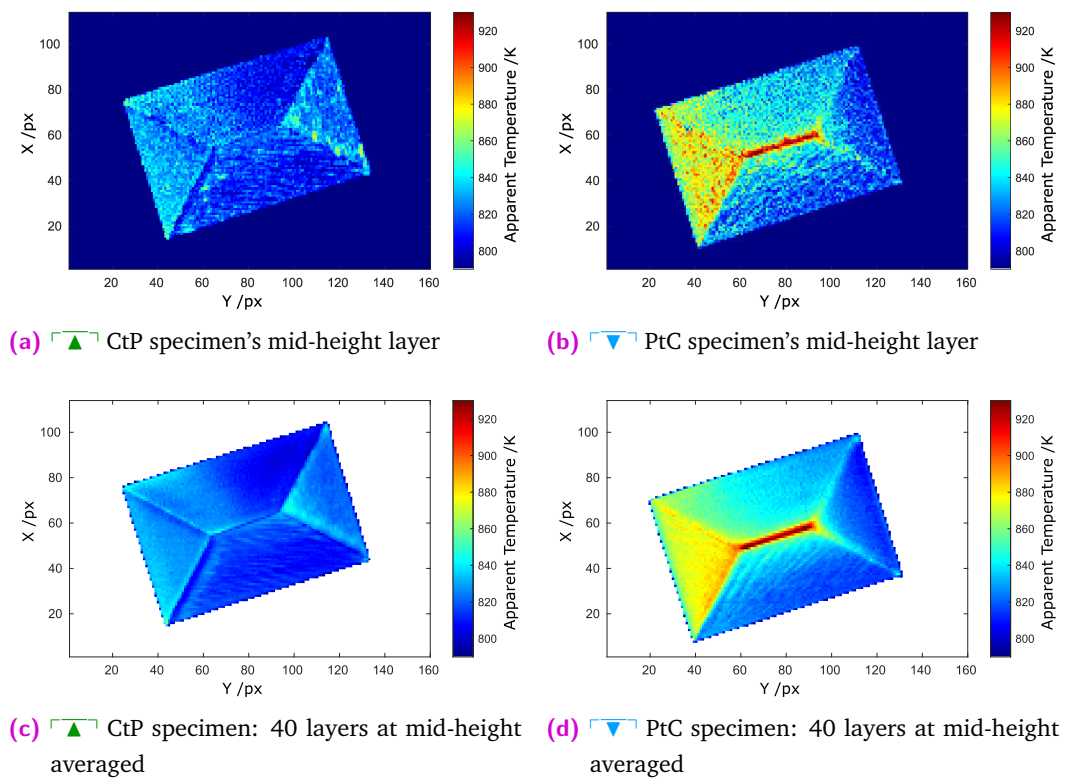


Fig. 5.5: Uncalibrated apparent maximum surface temperature obtained from thermography data acquired *during* the build process at the sample's mid build height. Each border fill scan started and ended at the bottom right hand. Fig. a) and b) display the mid-height layer, fig. c) and d) display an average of 40 layers at the mid-height. Images taken from Ulbricht et al. [39]

The cooling rate $-dT/dt$ of the two specimens is shown in fig. 5.6. Details on the determination of the cooling rates can be found in [39]. As for the apparent temperatures fig. 5.6 displays the mid-height plane and averaged values for 2 mm around the mid-height plane. From the displayed data we can derive that the ∇ PtC specimen in addition to higher apparent temperatures also features lower cooling rates in the centre. The images of the \blacktriangle CtP specimen show a lower cooling rate at the edges of the specimen. This indicates that the surrounding metal powder served as an heat insulator for conduction, as described in literature [110].

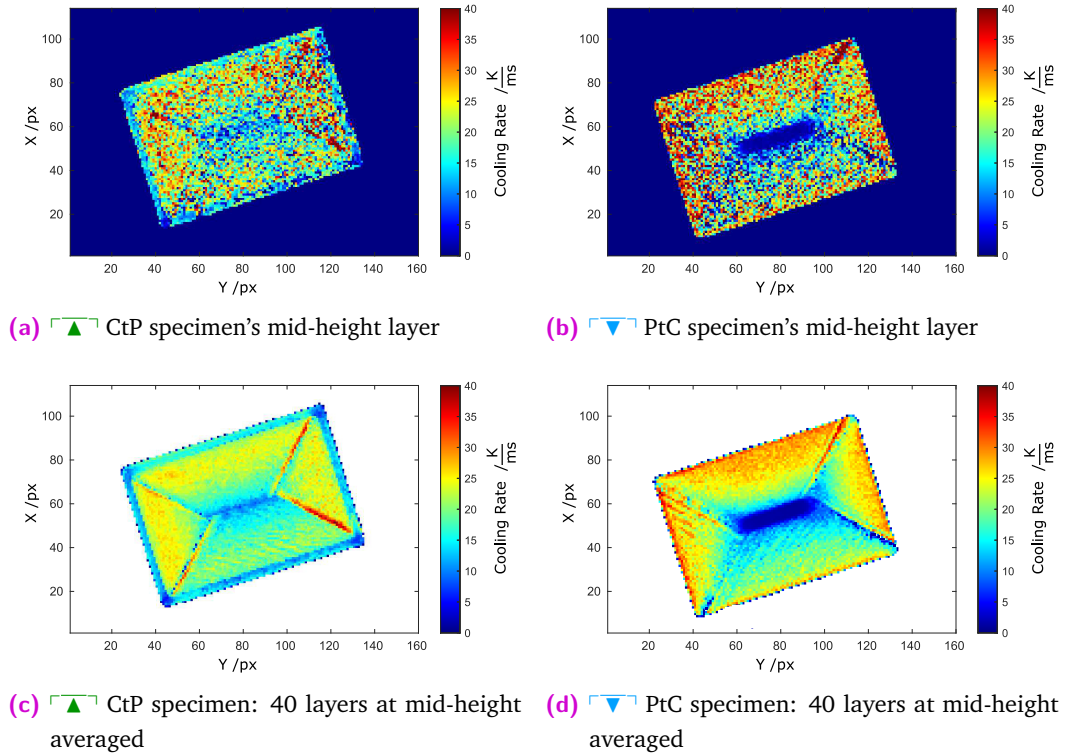


Fig. 5.6: Cooling rates determined by the different between images taken at $t_1 = 1$ ms and $t_2 = 2$ ms after an apparent surface temperature of 700 K was observed at. Fig. a) and b) display the mid-height layer, fig. c) and d) display an average of 40 layers around the middle of the total build height. Images taken from Ulbricht et al. [39]

So, from the on-line monitoring by thermographic cameras, it can clearly be derived that the two specimens have a different thermal history. The formation of RS by CSSM results from shrinkage of the illuminated laser tracks due to the solidification of the melt. In both specimens, scan tracks along the 36 mm long edge parallel to the y -axes are longer than for the 24 mm long edge parallel to the x -axes (see fig. 3.5 on page 39). Therefore, the longer scan tracks along the y -axes were more affected by the CSSM due to their length than the shorter scan tracks along the x -axes. In the

two prisms the shape of the σ_L - and σ_T -distribution looks similar. They differ only in their magnitude. These similarities between longitudinal and transversal stress component in the two specimens indicates that the CSSM is the main mechanism that forms the spatial distribution of these RS components. In the two specimens the TGM does not seem to have a significant role in the determination of the shape of the spatial RS distribution. Otherwise, a significant difference in the spatial distributions of the three RS components would be observable between the two specimens. However, the magnitudes of the bulk compressive stresses are higher for the ∇ PtC specimen than for the \blacktriangle CtP specimen. This result suggests that for these stress components the TGM only changes the magnitude of the RS distribution without changing the shape of the distribution itself. Mercelis and Kruth [13] describe the TGM as mechanism that is based on local plastic deformation at high temperatures, which induce compressive stresses when the plastically deformed regions cool down. This mechanism does not require melting and is not restricted to the current top layer. TGM can cause plastic deformation also in subjacent layers whose material is heated up several times by the illumination of superjacent layers. Therefore, the TGM can change the magnitude of RS values of the RS distribution. The results of the RS determination show that for the longitudinal and the transversal stress components the CSSM is shaping the RS distribution. Since the TGM is based on local deformations and the CSSM is based to a greater degree on global scan track shrinkage it is very plausible that the influence of the CSSM on the RS formation is much higher than the locally applied TGM. The distribution of the RS component along the z -axes (*i.e.*, parallel to the build direction) shows a completely different shape than the two other orthogonal directions. The illuminated top surface is always a free surface. Therefore, solidification shrinkage in the build direction is not constrained. Hence, the influence of the CSSM on the formation of the σ_N component should be very low. As a result, the observed distribution for σ_N is suggested to be mainly controlled by the TGM. This assumption can be verified with the help of the thermography data. In fig. 5.7 an overlay is shown of the contour plot of the σ_N distribution and the apparent temperature data obtained during the build job.

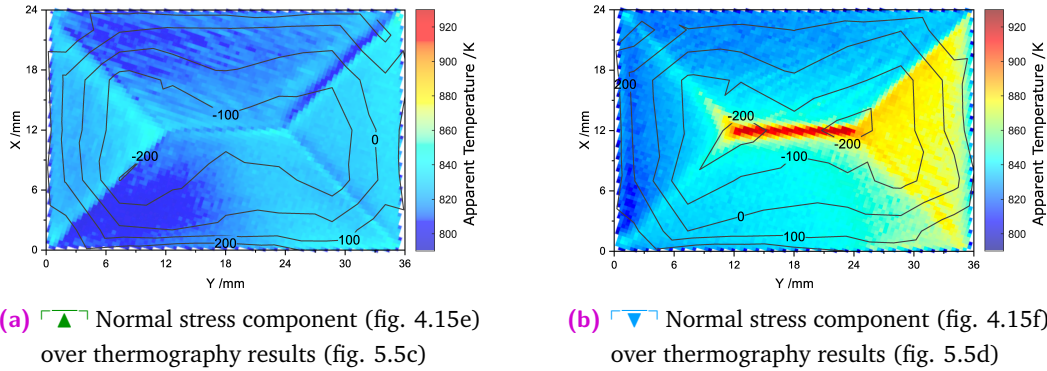


Fig. 5.7: Normal (*i.e.*, build direction) stress component (contour lines) in MPa (fig. 4.15e-f) combined with thermography results (fig. 5.5c-d) to highlight the compressive stresses at the laser's turn locations. Images taken from Ulbricht et al. [39]

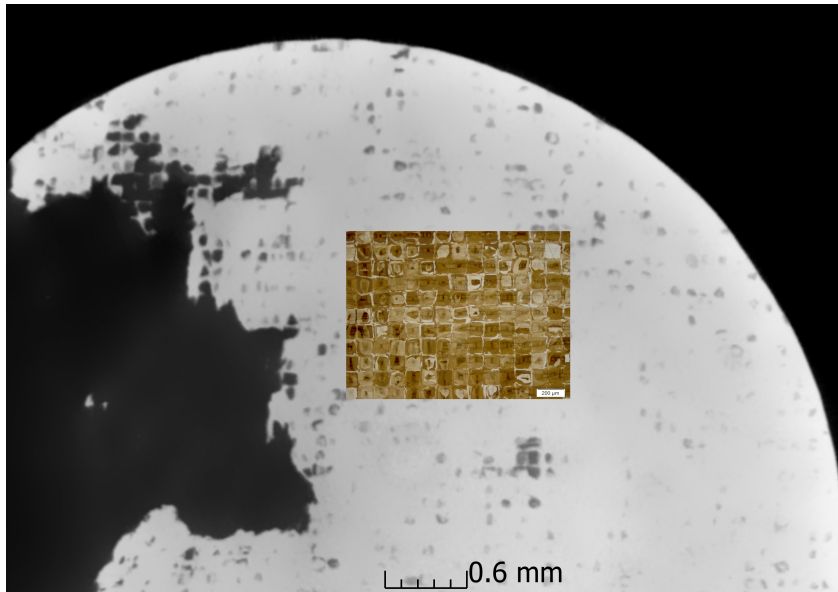
The figure clearly shows that the shape of the RS distribution is connected to the turning locations of the laser. At these location the laser decelerates due to the repositioning of the guiding mirrors, resulting in an increased VED. In both specimens the increased VED seems to locally induce higher compressive stresses at the turn locations than at locations of constant VED (*i.e.*, the mids of the scan tracks). Comparing the σ_N component of the two specimens shows that the $\square \blacktriangledown \square$ PtC specimen features higher magnitudes of compressive RS than the $\square \blacktriangle \square$ CtP specimen. The combination of thermography data and RS data (fig. 5.7) shows that the centre of the $\square \blacktriangledown \square$ PtC specimen not only was heated up to higher temperatures than the $\square \blacktriangle \square$ CtP specimen, it also cooled down more slowly (see fig. 5.6). Therefore, thermography data support the assumption that an increased heat input in the centre induced higher compressive RS values, as indicated for the turning locations of the laser.

In terms of void formation, the results of XCT and radiography of the specimens show that voids form at the centre of the $\square \blacktriangledown \square$ PtC specimen as well as at the laser's turning locations. The increased VED at these locations is an indicator for the formation of keyhole pores [12].

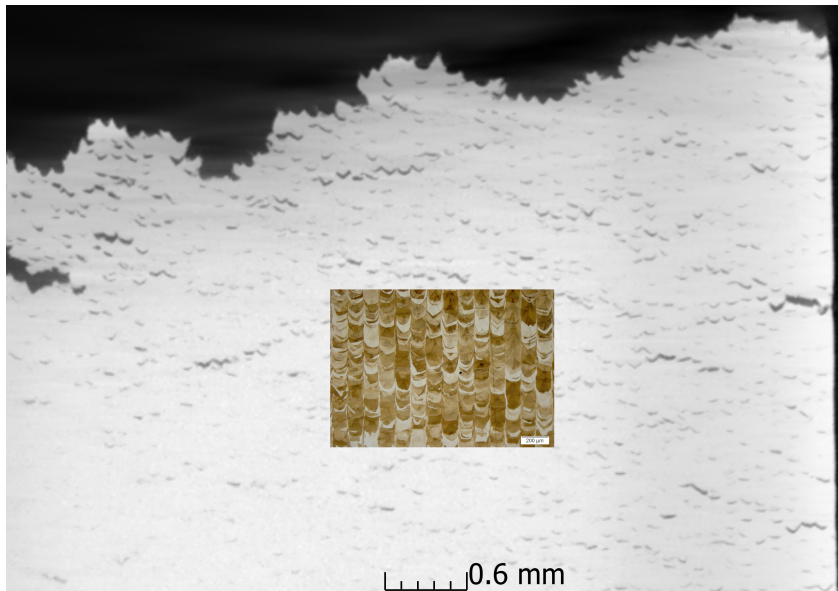
5.4 Damage Formation in High Temperature Creep and Tensile Deformed PBF-LB/M/316L

As described in the result chapter 4.5.2, hot rolled and PBF-LB/M/316L specimens react differently to the application of external loads. In the case of creep specimens

the comparison of an PBF-LB/M/316L specimen (K04) and a hot rolled specimen revealed that the PBF-LB/M/316L specimen seems behave in a more brittle way during creep deformation. This is shown by the rather brittle fracture surface which shows no macroscopic signs of plastic deformation such as necking. The latter can be observed for the hot rolled specimen. Necking is an indicator for plastic deformation. The elongation of the specimen results in a reduction of the specimen's diameter. In contrast, the PBF-LB/M/316L material response to creep is a structured network of internal micro cracks. No significant reduction in the specimen's diameter was observed. The specimen's elongation was realised only by the development of micro cracks. As depicted in these images the distribution of internal voids is structured in stacked voids. Comparing these voids with optical microscopy images of the PBF-LB/M/316L microstructure [67] reveals that the size and shape of these stacked micro cracks corresponds to the morphology of the grains of PBF-LB/M/316L (see fig. 5.8). Micro cracks occur predominantly along the grain boundaries perpendicular or up to 45° to the building direction, reflecting the bowl shaped grain morphology [17, 67].



(a) horizontal virtual cut



(b) vertical virtual cut

Fig. 5.8: Combination of XCT images of K04 and microscopy images of a similar untested specimen of the same microstructure. The microscopy images of the microstructure were obtained from a similar PBF-LB/M/316L specimen and were scaled to match the resolution of the XCT images. The microscopy images were provided by Konstantin Sommer.

The XCT analysis of the PBF-LB/M/316L creep specimen K04 revealed that larger cracks in the material are formed by connected networks of micro cracks which are found close to the fracture surface. The fracture surface itself consists of connected

micro cracks along the grain boundaries. In the hot rolled material cracks started to occur on the specimens surface. They grew until the final rupture of the specimen. In contrast, in the PBF-LB/M/316L specimen it could be shown that macroscopic cracks develop from clusters of interconnected micro cracks. These macroscopic cracks form at different locations within the specimen. Therefore, in PBF-LB/M/316L the formation of macroscopic cracks does not seem to be limited to be initiated from surface cracks.

To reveal a more detailed picture of the microstructural response of PBF-LB/M/316L the void distribution of two creep specimens (K01 and K05) was studied by XCT at three distinct stages of the creep test. No distinct cracks were detected in the vicinity of previous void locations in the broken specimen that are located far away from the rupture surface. In contrast to the results of Williams et al. [18] no correlation between internal porosity and crack growth was found. Due to the low porosity content and small void size, it was not possible to track the evolution of damage with respect to the original void population. The observed internal porosity of the analysed specimens of this work ($\approx 0.001\%$) was much lower than in Williams et al. [18] (0.3% to 0.4%).

Comparing K01 to K05 at t_0 and t_i similar porosity values are observed. After the creep test in K05 a similar structure of stacked micro cracks was observed as in K01 and K04. The main difference between the two specimens K01 and K05 is the amount of micro cracks observed in the broken state. In contrast to K01 the void distribution in K05 after the creep test is not localised near the rupture surface. Instead it is widely distributed along the long axis. In K01 only a small elongation of approximately 1.5 mm is observed, whereas in K05 a elongation of approximately 4 mm is observed. The elongation can be attributed to the difference in the spatial distribution and the amount of micro cracks in the two specimens.

The observed gap after stitching in the centre of the two broken creep specimen seems to indicate some plastic deformation at the outer regions of the specimens' cross section. As in K01 no significant networks of cracks (*i.e.*, macroscopic cracks) were observed further away from the rupture surface. Therefore, the initial voids do not seem to have an influence on damage accumulation in neither the specimen K01 nor K05. K01 was on test for 402 h until the final rupture. The interruption time was at 143 h (35% of the time to rupture). Although the number of detected voids increased by this time no significant micro cracks were detectable by XCT. This can be either interpreted so that cracks started to form at a later stage of the creep test or that possible existing cracks were closed when unloading the specimen. The creep test of specimen K05 was interrupted at 29% of the time to rupture of

155 h. Similar elongation and increase of the initial void population than in K01 indicate similar deformation mechanisms in the two specimens until their specific interruption times t_i . The two specimens' broken condition differed significantly. The accumulated damage of K05 was larger than of K01 despite the lesser applied load ($R_0 = 175$ MPa for K05 compared to $R_0 = 200$ MPa for K01). This indicates that the different testing temperature was the key parameter causing the difference in accumulated damage.

For conventionally produced AISI 316L Driver et al. [64] have reported that crack initiation mechanisms “tend to become partially intergranular at 600 °C.” These mechanisms seems to apply for PBF-LB/M/316L as well. Specimen K01 was tested at 600 °C, the temperature were intergranular crack initiation is supposed to start. Although micro cracks were found at all height of the gauge length of K01, their population is mainly concentrated near the rupture surface as seen for the hot rolled specimen. Although the response mechanism of PBF-LB/M/316L to creep is mainly micro cracking instead of plastic deformation. The testing temperature for specimen K05 was 50 °C higher than for K01, and this resulted in a network of micro cracks which was more evenly distributed along the gauge length of the specimen than in K01. This supports the assumption by Driver et al. of intergranular cracking at temperatures higher than 600 °C.

Interestingly, results from the XCT analysis of a broken tensile specimen draw a slightly different picture of the materials response to high temperature loads. In the tensile specimen necking is visible near the rupture surface. Despite the necking, a similar structured void distribution is observed in the tensile specimen as is for the creep specimens. This indicates that micro cracks at the grain boundaries are also the main damage mechanism. The fracture surface of the tensile specimen shows a different fracture pattern than the creep specimens. In the centre of the fracture surface the surface pattern looks similar to the fracture surface of the creep specimens. Closer towards the necked perimeter of the fracture surface a much more flattened fracture pattern is observed, and the chess-board pattern indicating intergranular fracture is less visible. This indicates a rather ductile fracture in this area, and the cup-and-cone fracture surface enhances this conclusion.

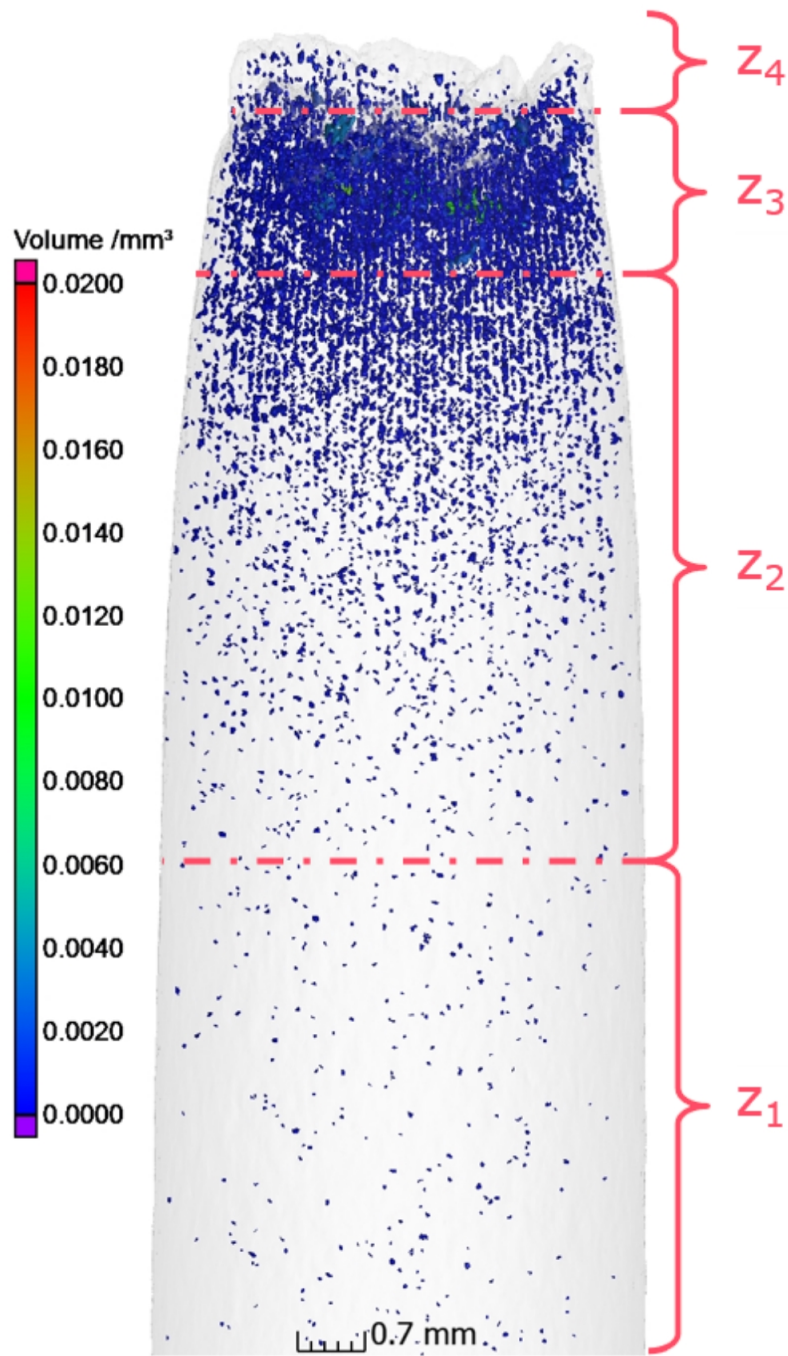


Fig. 5.9: 3D rendering of the void distribution in the longer bottom part of the broken tensile specimen

To highlight the different shapes of voids in distinct zones voids were virtually extracted from three positions in the upper half of the broken tensile specimen as depicted in fig. 5.10.

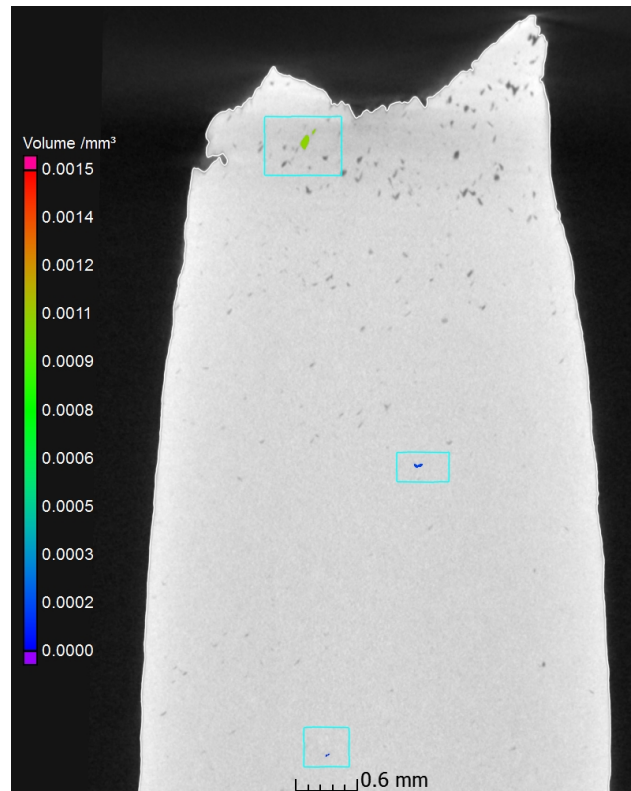


Fig. 5.10: Three distinct voids of different shape are marked in the longer bottom part of the broken tensile specimen

The analysis of the XCT data enables the classification of different zones within the specimen as depicted in fig. 5.9. The void distribution furthest away from the fracture surface (z_1) consists mainly of plate-shaped voids (see fig. 5.11a). This zone also shows no necking. In the next zone towards the fracture surface (z_2) a reduction of the specimen's diameter can be observed due to plastic deformation. In z_2 also "V" shaped voids (see fig. 5.11b) are observed in addition to the plate shaped voids. These voids correspond to the grain morphology of PBF-LB/M/316L (see fig. 5.8b on page 96). Therefore, as observed in the creep specimen, crack initiation at the horizontal grain boundaries seems to be the underlying damage mechanism. In the zone next to the rupture surface (z_3) cluster of combined micro cracks are observed (see fig. 5.11c). In this zone the diameter is even more reduced due to plastic deformation.

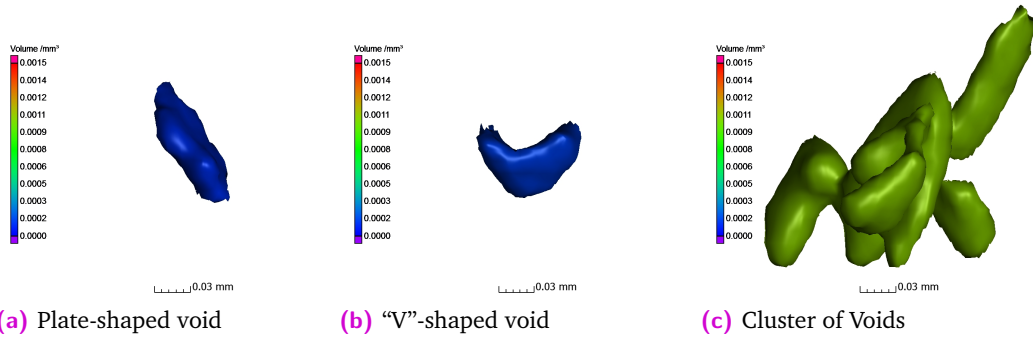


Fig. 5.11: 3D rendering of the three shapes of voids found in the broken tensile specimen.

Zone z_4 is the region of the actual rupture surface. At the centre of the rupture surface the crack’s surface has a shape similar to the rupture surface of the creep specimen. The rendering of rupture surface at the perimeter of the tensile specimen’s cross section seems to be much smoother than in the centre. This indicates a ductile fracture (*i.e.*, shear lip) forming its typical cup-and-cone fracture shape.

Summary and Concluding Remarks

“ *There is no such thing as an accident. That’s what science is all about. [...] There are only patterns we don’t yet recognize.*

— **Tad Williams**

(Otherland: City of the Golden Shadow)

6.1 Void Formation in PBF-LB/M/316L

The formation of voids in PBF-LB/M/316L has been studied by analysing specimens with optimised process parameter sets provided by the machine manufacturer and non-optimised parameter sets using computed tomography. The use of optimised process parameter sets for PBF-LB/M/316L creates parts without any significant porosity. Furthermore, it is shown that the melt pool depth of these parameter sets was able to melt multiples of the layer thickness without creating voids. It is shown that no additional porosity was observed up to a thickness of $200\mu\text{m}$ of unexposed powder (*i.e.*, four standard powder layers).

6.2 Residual Stress Formation in PBF-LB/M/316L

Two prismatic AISI 316L specimens using two alternate border fill scan strategy were produced in order to separate the effect of the temperature gradient mechanism from the solidification shrinkage mechanism in AM metallic parts produced by PBF-LB/M/316L. The following conclusions are made: A combination of surface and bulk residual stress results was needed to characterise the (surface) tensile and (bulk) compressive regions of the in-plane stress distribution. By comparing the two samples, it was revealed that the stress distributions observed are broadly similar. This indicates that constrained solidification shrinkage is the main mechanism

controlling the shape of the residual stress distribution in these specimens. The temperature gradient mechanism seems to influence only the magnitude of the compressive stresses without changing the overall spatial pattern of the stress distribution. On-line thermography results of the specimen illuminated towards the perimeter revealed a heat higher accumulation at the centre, which corresponds to highly localised compressive stresses due to the temperature gradient mechanism.

6.3 Damage in PBF-LB/M/316L

Creep and tensile specimens were studied to investigate the interaction of existing defects with damage accumulated during high temperature tensile and creep deformation. In all broken specimens a structured void distribution was detected, which was shown to be connected to the shape of the grains of the material. Analysis of XCT data showed that these micro cracks form as vertically stacked micro cracks. The micro cracks follow the horizontal grain boundaries and resemble the grins when they are open. In contrast to hot rolled material the main mechanism of PBF-LB/M/316L to creep is micro-cracking instead of plastic deformation.

As an addition to classical 2D methods (e.g., destructive metallography), non-destructive 3D analysis techniques such as XCT enable a three dimensional analysis to find correlations between the shape of observed defects and the grain morphology. The studied specimens were produced using 90° rotating stripe scan strategy, which results in stacked grains. The present result show that micro cracks occur mainly at the horizontal grain boundaries.

In comparison to the analysis of PBF-LB/M creep specimens available in literature, it could be shown that the grain morphology—which results from the applied scan strategy—determines the internal damage formation. It has also been shown how damage forms in creep in the near absence of initial internal porosity.

6.4 Concluding Remarks

The aim of this work was to analyse defects and residual stresses in specimens made of PBF-LB/M/316L to improve the understanding of their formation. It was shown that the use of optimised build process parameters provided by the machine manufacturer enabled the manufacture of specimens with very low porosity. The average void size was a fraction of the grain size of the material. The XCT analysis of

this material revealed that the formation of creep damage at temperatures of 600 °C and above is mainly caused by micro cracking along grain boundaries perpendicular to the loading axis (*i.e.*, build direction). This result emphasises the influence of the PBF-LB/M/316L microstructure on material performance. Since the microstructure is determined by build process parameters this work contributes to the discussion of how to classify additively manufactured metals. The strong dependency of PBF-LB/M/316L microstructure on specific process parameters—especially on the hatching pattern—emphasises the assumption that each combination of machine and process parameters results in a unique variant of PBF-LB/M/316L with different mechanical properties. It can be concluded that the heat input from a melt pool based on optimised process parameters for PBF-LB/M/316L on a SLM Solutions 280HM is able to sufficiently melt powder for a thickness of up to four times the standard thickness of 50 μm without the creation of voids. It was also shown that the melt pool has a sufficient depth to cause fusion of the underlying solid material, and still enable the escape of entrapped gas pores from the melt. This might enable further process parameter optimisation to make the process faster (e.g., by increasing the scan speed). However, the current process of melting powder and re-melting several solid layers of material renders the build process less prone to irregularities during the build job (e.g., heterogeneities of the powder re-coating process). The presented combined results of thermographic on-line inspection of the build process and XCT have increased the knowledge of the PBF-LB/M process. It was shown that the surface roughness of the layers can serve as seeding location for LoF voids. The present results also suggest that healing among layers only occurs, if the orientation of the scan pattern is changed at each layer. Applying the same scan pattern on each layer can form voids that are locked into the final part.

In terms of residual stress this work evaluated the influence of the two main contribution mechanisms on the formation of residual stress in PBF-LB/M/316L. It was shown that changes to the hatch lengths (*i.e.*, a change of the constrained solidification) determined the spatial distribution of residual stress. Consequently, well designed hatching patterns could improve the service life of PBF-LB/M/316L components when the residual stress distribution is modified to accommodate the expected external load cases of the component. Furthermore, the results of this work indicate that locations of high void concentration in components (e.g., locations where the laser turns) can serve as initiation zones for stress relieve by micro cracking. Therefore, process parameters should be adapted to prevent void formation in component locations where high tensile residual stress can be expected.

Outlook & Future Research

” ... to boldly go where no one has gone before.

— Gene Roddenberry
(Star Trek)

7.1 Advancements in Imaging

The analysis of specimens in this work revealed two interlinked problems common to the XCT analysis of parts produced by laser powder bed fusion:

1. The size of the most irregularities found in these specimens was very small (*i.e.*, in the order of magnitude of the material's grains and below)
2. The size of industrial relevant laser powder bed fused parts does not enable inspection by computed tomography at the needed resolution to detect irregularities.

The combination of on-line monitoring results and computed tomography results shown in this work can offer possible solutions for these problems. Instead of scanning a laser powder bed fused part completely, in the future one could perform a highly resolved scan at a location in the part, which is defined by results from on-line monitoring techniques. This will require a sophisticated registration of the two datasets, which covers the deformation history of a specimen from on-line monitored laser powder bed fusion of specific layers to the stress relieving removal of the component from the build plate.

Additionally, fusing computed tomography data with data from on-line monitoring of the build process and/or data from other non-destructive techniques will enable the analysis of the fused data in a higher dimensional space. Using machine learning techniques it is possible to detect irregularities in the higher dimensional data set, which could not be detected when each data set is separately analysed. The main challenge of the analysis of higher dimensional fused data sets is the complexity of the data. In contrast to most non-destructive testing techniques, the benefit

of computed tomography is that it generates visual results, that are intuitive to the human comprehension. For fused data one is depending on machine learning techniques to recognise irregularities or patterns in the data. The quality of these machine learning techniques is depending on the quality of the model's training. Creating a sufficient amount of training data is the key to solve problems using machine learning. Artificial datasets with increased void populations based on the void distribution of real data could improve the training data aside from forcing the emergence of voids in specimens by modifying process parameters.

More quantitative studies are required to assess whether the inherent voids of additively manufactured components could become a service life threatening defect. In-situ computed tomography measurements of creep and tensile loaded specimens could enable the tracking of damage formation throughout the mechanical test. Currently, such an assessment can only be performed with load rigs small enough to fit into computed tomography scanners. Therefore, only small test specimens can be scanned while being tested. Instead of building a load rig that fits into a computed tomography scanner one could think of the opposite: A gantry-based industrial computed tomography scanner placed around a mechanical loading rig. This could lift mechanical testing to a new level: the in-situ three-dimensional assessment of damage formation. Also, the acquisition times must be reduced drastically to enable computed tomography scans during mechanical tests. This can be achieved by implementing image enhancement techniques from medical computed tomography to the reconstruction of the data. Solutions to enhance the data quality of short measurements and to compensate the movement of the object during a scan have been developed for years for medical computed tomography. Implementing these optimisations into industrial computed tomography scanners could enable the scan of specimens during a mechanical test with no or very small stoppage time.

7.2 Advancements in Residual Stress Analysis

The key component to determine residual stresses accurately is the choice of a stress-free reference specimen. Unreleased residual stresses which remain in the reference specimen will offset the calculated values of the stresses of the inspected part. The neutron diffraction community is still in need of an in-depth study of how the thermal history of laser powder bed fusion influences the local lattice spacing within the part. The use of a global stress-free reference is based on the assumption that the stress-free lattice spacing is constant within the part, such that there are no

chemical gradients on the length-scale over which the stresses are determined. This is an assumption which has to be verified.

Even if this assumption is valid, the major problem remains: How can one assure that the stress-free reference's microstructure represents the actual microstructure of the analysed object?

Simulations could offer a possible solution to this problem—at least for some use cases. A stress and moment balance requires all residual stress components and moments to sum up to zero over the volume whole part. If at least one full internal plane is analysed, a stress-free lattice spacing could be derived from solving the stress balance of the studied part itself, making the neutron diffraction technique fully non-destructive. I developed a simplified stress balance algorithm but the quality of such an approach is determined by the density of the data. The subsurface tensile components of the residual stress distribution in laser powder bed fused parts are difficult to determine using non-destructive techniques. It needs to be verified whether the gap of information from these locations is detrimental to the quality of the stress balance. A possible approach could be the determination of residual stress of this internal plane by different residual stress analysis methods, as such as the contour method. Further materials and geometries need to be tested to ensure the robustness of the stress balance approach.

Bibliography

- [1] ASTM F2792-12a, *Standard Terminology for Additive Manufacturing Technologies, (Withdrawn 2015)*. West Conshohocken, PA, USA: ASTM International, 2012. DOI: 10.1520/f2792-12a (cit. on p. 1).
- [2] William E. Frazier. “Metal Additive Manufacturing: A Review”. In: *Journal of Materials Engineering and Performance* 23.6 (2014), pp. 1917–1928. DOI: 10.1007/s11665-014-0958-z (cit. on pp. 1, 2).
- [3] H. Bikas, P. Stavropoulos, and G. Chryssolouris. “Additive manufacturing methods and modelling approaches: a critical review”. In: *The International Journal of Advanced Manufacturing Technology* 83.1-4 (July 2015), pp. 389–405. DOI: 10.1007/s00170-015-7576-2 (cit. on p. 1).
- [4] Amir Mahyar Khorasani, Ian Gibson, Jithin Kozhuthala Veetil, and Amir Hossein Ghasemi. “A review of technological improvements in laser-based powder bed fusion of metal printers”. In: *The International Journal of Advanced Manufacturing Technology* 108.1-2 (May 2020), pp. 191–209. DOI: 10.1007/s00170-020-05361-3 (cit. on p. 3).
- [5] Tien T. Roehling, Sheldon S. Q. Wu, Saad A. Khairallah, et al. “Modulating laser intensity profile ellipticity for microstructural control during metal additive manufacturing”. In: *Acta Materialia* 128 (2017), pp. 197–206. DOI: 10.1016/j.actamat.2017.02.025 (cit. on pp. 3, 4, 6, 8).
- [6] Hideki Kyogoku and Toshi-Taka Ikeshoji. “A review of metal additive manufacturing technologies: Mechanism of defects formation and simulation of melting and solidification phenomena in laser powder bed fusion process”. In: *Mechanical Engineering Reviews* 7.1 (2020), pp. 1–19. DOI: 10.1299/mer.19-00182 (cit. on pp. 3, 8).
- [7] W. E. King, A. T. Anderson, R. M. Ferencz, et al. “Laser powder bed fusion additive manufacturing of metals, physics, computational, and materials challenges”. In: *Applied Physics Reviews* 2.4 (Dec. 2015), p. 041304. DOI: 10.1063/1.4937809 (cit. on p. 3).
- [8] William L. Smith, John D. Roehling, Maria Strantza, et al. “Residual stress analysis of in situ surface layer heating effects on laser powder bed fusion of 316L stainless steel”. In: *Additive Manufacturing* 47 (Nov. 2021), p. 102252. DOI: 10.1016/j.addma.2021.102252 (cit. on pp. 3, 6).
- [9] Terry Wohlers. *Rapid Prototyping, State of the Industry: 1995-96 Worldwide Progress Report*. Colorado, USA: Wohlers Associates, Inc., 1996 (cit. on p. 3).

- [10] Xiao-qing Ni, De-cheng Kong, Ying Wen, et al. “Anisotropy in mechanical properties and corrosion resistance of 316L stainless steel fabricated by selective laser melting”. In: *International Journal of Minerals, Metallurgy, and Materials* 26.3 (Mar. 2019), pp. 319–328. DOI: 10.1007/s12613-019-1740-x (cit. on p. 3).
- [11] Tobias Ronneberg, Catrin M. Davies, and Paul A. Hooper. “Revealing relationships between porosity, microstructure and mechanical properties of laser powder bed fusion 316L stainless steel through heat treatment”. In: *Materials & Design* 189 (Apr. 2020), p. 108481. DOI: 10.1016/j.matdes.2020.108481 (cit. on pp. 3, 5).
- [12] A. A. Martin, N. P. Calta, S. A. Khairallah, et al. “Dynamics of pore formation during laser powder bed fusion additive manufacturing”. In: *Nature Communications* 10.1 (2019), p. 1987. DOI: 10.1038/s41467-019-10009-2 (cit. on pp. 3, 5, 85, 94).
- [13] Peter Mercelis and Jean-Pierre Kruth. “Residual stresses in selective laser sintering and selective laser melting”. In: *Rapid Prototyping Journal* 12.5 (2006), pp. 254–265. DOI: 10.1108/13552540610707013 (cit. on pp. 3, 6, 9, 38, 93).
- [14] Richard J. Williams, Filippo Vecchiato, Joe Kelleher, et al. “Effects of heat treatment on residual stresses in the laser powder bed fusion of 316L stainless steel: Finite element predictions and neutron diffraction measurements”. In: *Journal of Manufacturing Processes* 57 (Sept. 2020), pp. 641–653. DOI: 10.1016/j.jmapro.2020.07.023 (cit. on pp. 3, 7).
- [15] Thomas Niendorf, Stefan Leuders, Andre Riemer, et al. “Highly Anisotropic Steel Processed by Selective Laser Melting”. In: *Metallurgical and Materials Transactions B* 44.4 (May 2013), pp. 794–796. DOI: 10.1007/s11663-013-9875-z (cit. on p. 4).
- [16] O. Fergani, V. Brotan, M. Bambach, and M. T. Perez-Prado. “Texture evolution in stainless steel processed by selective laser melting and annealing”. In: *Materials Science and Technology* 34.18 (Sept. 2018), pp. 2223–2230. DOI: 10.1080/02670836.2018.1523518 (cit. on p. 4).
- [17] A. Charmi, R. Falkenberg, L. Avila, et al. “Mechanical anisotropy of additively manufactured stainless steel 316L: An experimental and numerical study”. In: *Materials Science and Engineering: A* 799 (2021), p. 140154. DOI: 10.1016/j.msea.2020.140154 (cit. on pp. 4, 8, 32, 71, 95).
- [18] Richard J. Williams, Jalal Al-Lami, Paul A. Hooper, Minh-Son Pham, and Catrin M. Davies. “Creep deformation and failure properties of 316 L stainless steel manufactured by laser powder bed fusion under multiaxial loading conditions”. In: *Additive Manufacturing* 37 (2021), p. 101706. DOI: 10.1016/j.addma.2020.101706 (cit. on pp. 4, 8, 10, 97).
- [19] Gunther Mohr, Konstantin Sommer, Tim Knobloch, et al. “Process Induced Pre-heating in Laser Powder Bed Fusion Monitored by Thermography and Its Influence on the Microstructure of 316L Stainless Steel Parts”. In: *Metals* 11.7 (July 2021), p. 1063. DOI: 10.3390/met11071063 (cit. on p. 4).

- [20] R. E. Trevisan, D. D. Schwemmer, and D. L. Olson. “CHAPTER 3 - The Fundamentals of Weld Metal Pore Formation”. In: *Welding*. Ed. by David L. Olson, Ray Dixon, and Alan L. Liby. Vol. 8. Materials Processing: Theory and Practices. Elsevier, 1990, pp. 79–115. DOI: 10.1016/B978-0-444-87427-6.50009-5 (cit. on p. 4).
- [21] Seiji Katayama, Naoki Seto, Jong-Do Kim, and Akira Matsunaw. “Formation mechanism and reduction method of porosity in laser welding of stainless steel”. In: *International Congress on Applications of Lasers & Electro-Optics*. Vol. 1997. 1. Laser Institute of America. 1997, G83–G92. DOI: 10.2351/1.5059741 (cit. on p. 4).
- [22] Ross Cunningham, Sneha P Narra, Colt Montgomery, Jack Beuth, and AD Rollett. “Synchrotron-based X-ray microtomography characterization of the effect of processing variables on porosity formation in laser powder-bed additive manufacturing of Ti-6Al-4V”. In: *Jom* 69.3 (2017), pp. 479–484. DOI: 10.1007/s11837-016-2234-1 (cit. on p. 5).
- [23] Wayne E. King, Holly D. Barth, Victor M. Castillo, et al. “Observation of keyhole-mode laser melting in laser powder-bed fusion additive manufacturing”. In: *Journal of Materials Processing Technology* 214.12 (2014), pp. 2915–2925. DOI: 10.1016/j.jmatprotec.2014.06.005 (cit. on p. 5).
- [24] Chinnapat Panwisawas, Bama Perumal, R. Mark Ward, et al. “Keyhole formation and thermal fluid flow-induced porosity during laser fusion welding in titanium alloys: Experimental and modelling”. In: *Acta Materialia* 126 (2017), pp. 251–263. DOI: 10.1016/j.actamat.2016.12.062 (cit. on p. 5).
- [25] Saad A. Khairallah, Andrew T. Anderson, Alexander Rubenchik, and Wayne E. King. “Laser powder-bed fusion additive manufacturing: Physics of complex melt flow and formation mechanisms of pores, spatter, and denudation zones”. In: *Acta Materialia* 108 (2016), pp. 36–45. DOI: 10.1016/j.actamat.2016.02.014 (cit. on pp. 5, 6, 9, 62, 83, 85, 88, 90).
- [26] Gunther Mohr, Simon J. Altenburg, Alexander Ulbricht, et al. “In-Situ Defect Detection in Laser Powder Bed Fusion by Using Thermography and Optical Tomography—Comparison to Computed Tomography”. In: *Metals* 10.1 (2020), p. 103. DOI: 10.3390/met10010103 (cit. on pp. 5, 6, 9, 11, 31, 32, 36, 47).
- [27] S. Mohammad H. Hojjatzadeh, Niranjana D. Parab, Wentao Yan, et al. “Pore elimination mechanisms during 3D printing of metals”. In: *Nature Communications* 10.1 (2019). DOI: 10.1038/s41467-019-10973-9 (cit. on pp. 6, 83).
- [28] Ross Cunningham, Andrea Nicolas, John Madsen, et al. “Analyzing the effects of powder and post-processing on porosity and properties of electron beam melted Ti-6Al-4V”. In: *Materials Research Letters* 5.7 (2017), pp. 516–525. DOI: 10.1080/21663831.2017.1340911 (cit. on pp. 6, 83).
- [29] Ming Tang and P. Chris Pistorius. “Oxides, porosity and fatigue performance of AlSi10Mg parts produced by selective laser melting”. In: *International Journal of Fatigue* 94 (2017), pp. 192–201. DOI: 10.1016/j.ijfatigue.2016.06.002 (cit. on pp. 6, 83).

- [30] Christian Weingarten, Damien Buchbinder, Norbert Pirch, et al. “Formation and reduction of hydrogen porosity during selective laser melting of AlSi10Mg”. In: *Journal of Materials Processing Technology* 221 (2015), pp. 112–120. DOI: 10.1016/j.jmatprotec.2015.02.013 (cit. on pp. 6, 83).
- [31] Giulia Repossini, Vittorio Laguzza, Marco Grasso, and Bianca Maria Colosimo. “On the use of spatter signature for in-situ monitoring of Laser Powder Bed Fusion”. In: *Additive Manufacturing* 16 (2017), pp. 35–48. DOI: 10.1016/j.addma.2017.05.004 (cit. on p. 6).
- [32] Christopher Barrett, Carolyn Carradero, Evan Harris, et al. “Statistical analysis of spatter velocity with high-speed stereovision in laser powder bed fusion”. In: *Progress in Additive Manufacturing* 4.4 (Aug. 2019), pp. 423–430. DOI: 10.1007/s40964-019-00094-6 (cit. on p. 6).
- [33] Nils Scheuschner, Simon J Altenburg, Andrey Gumenyuk, and Christiane Maierhofer. “In-situ thermographic monitoring of the laser metal deposition process”. In: *Sim-AM 2019 : II International Conference on Simulation for Additive Manufacturing*. CIMNE, 2019. 2019, pp. 246–255 (cit. on pp. 6, 11).
- [34] Richard J. Williams, Alessandro Piglione, Tobias Rønneberg, et al. “In situ thermography for laser powder bed fusion: Effects of layer temperature on porosity, microstructure and mechanical properties”. In: *Additive Manufacturing* 30 (Dec. 2019), p. 100880. DOI: 10.1016/j.addma.2019.100880 (cit. on p. 6).
- [35] Jean-Baptiste Forien, Nicholas P. Calta, Philip J. DePond, et al. “Detecting keyhole pore defects and monitoring process signatures during laser powder bed fusion: A correlation between in situ pyrometry and ex situ X-ray radiography”. In: *Additive Manufacturing* 35 (2020), p. 101336. DOI: 10.1016/j.addma.2020.101336 (cit. on p. 6).
- [36] C. L. Druzgalski, A. Ashby, G. Guss, et al. “Process optimization of complex geometries using feed forward control for laser powder bed fusion additive manufacturing”. In: *Additive Manufacturing* 34 (2020), p. 101169. DOI: 10.1016/j.addma.2020.101169 (cit. on p. 6).
- [37] Richard J. Williams, Catrin M. Davies, and Paul A. Hooper. “In situ monitoring of the layer height in laser powder bed fusion”. In: *Material Design & Processing Communications* (Apr. 2020). DOI: 10.1002/mdp2.173 (cit. on p. 6).
- [38] Alexander Ulbricht, Gunther Mohr, Simon J. Altenburg, et al. “Can Potential Defects in LPBF Be Healed from the Laser Exposure of Subsequent Layers? A Quantitative Study”. In: *Metals* 11.7 (2021). DOI: 10.3390/met11071012 (cit. on pp. 6, 8, 31, 32, 52–56, 86, 87, 89).
- [39] Alexander Ulbricht, Simon J. Altenburg, Maximilian Sprengel, et al. “Separation of the Formation Mechanisms of Residual Stresses in LPBF 316L”. In: *Metals* 10.9 (2020). DOI: 10.3390/met10091234 (cit. on pp. 6, 9, 38, 57, 58, 60, 61, 63, 91, 92, 94).

- [40] Gunther Mohr, Simon J. Altenburg, and Kai Hilgenberg. “Effects of inter layer time and build height on resulting properties of 316L stainless steel processed by laser powder bed fusion”. In: *Additive Manufacturing* 32 (2020), p. 101080. DOI: 10.1016/j.addma.2020.101080 (cit. on p. 6).
- [41] Ming Tang, P. Chris Pistorius, and Jack L. Beuth. “Prediction of lack-of-fusion porosity for powder bed fusion”. In: *Additive Manufacturing* 14 (2017), pp. 39–48. DOI: 10.1016/j.addma.2016.12.001 (cit. on p. 6).
- [42] Jitka Metelkova, Yannis Kinds, Karolien Kempen, et al. “On the influence of laser defocusing in Selective Laser Melting of 316L”. In: *Additive Manufacturing* 23 (2018), pp. 161–169. DOI: 10.1016/j.addma.2018.08.006 (cit. on p. 6).
- [43] AV Gusarov and I Smurov. “Modeling the interaction of laser radiation with powder bed at selective laser melting”. In: *Physics Procedia* 5 (2010), pp. 381–394. DOI: 10.1016/j.phpro.2010.08.065 (cit. on pp. 6, 9, 86).
- [44] Ali Foroozmehr, Mohsen Badrossamay, Ehsan Foroozmehr, and Sa’id Golabi. “Finite Element Simulation of Selective Laser Melting process considering Optical Penetration Depth of laser in powder bed”. In: *Materials & Design* 89 (2016), pp. 255–263. DOI: 10.1016/j.matdes.2015.10.002 (cit. on pp. 6, 9, 84–86).
- [45] Mingming Ma, Zemin Wang, Ming Gao, and Xiaoyan Zeng. “Layer thickness dependence of performance in high-power selective laser melting of 1Cr18Ni9Ti stainless steel”. In: *Journal of Materials Processing Technology* 215 (2015), pp. 142–150. DOI: 10.1016/j.jmatprotec.2014.07.034 (cit. on pp. 6, 9).
- [46] A. Streek, P. Regenfuss, and H. Exner. “Fundamentals of Energy Conversion and Dissipation in Powder Layers during Laser Micro Sintering”. In: *Physics Procedia* 41 (2013), pp. 858–869. DOI: 10.1016/j.phpro.2013.03.159 (cit. on pp. 6, 9, 86).
- [47] P.J. Withers and H.K.D.H. Bhadeshia. “Residual stress. Part 1 – Measurement techniques”. In: *Materials Science and Technology* 17.4 (2001), pp. 355–365. DOI: 10.1179/026708301101509980 (cit. on pp. 6, 24).
- [48] Ruidi Li, Yusheng Shi, Zhigang Wang, et al. “Densification behavior of gas and water atomized 316L stainless steel powder during selective laser melting”. In: *Applied Surface Science* 256.13 (2010), pp. 4350–4356. DOI: 10.1016/j.apsusc.2010.02.030 (cit. on p. 7).
- [49] G. Miranda, S. Faria, F. Bartolomeu, et al. “Predictive models for physical and mechanical properties of 316L stainless steel produced by selective laser melting”. In: *Materials Science and Engineering: A* 657 (2016), pp. 43–56. DOI: 10.1016/j.msea.2016.01.028 (cit. on p. 7).
- [50] Di Wang, Shibiao Wu, Yongqiang Yang, et al. “The Effect of a Scanning Strategy on the Residual Stress of 316L Steel Parts Fabricated by Selective Laser Melting (SLM)”. In: *Materials* 11.10 (2018). DOI: 10.3390/ma11101821 (cit. on p. 7).
- [51] John D. Roehling, William L. Smith, Tien T. Roehling, et al. “Reducing residual stress by selective large-area diode surface heating during laser powder bed fusion additive manufacturing”. In: *Additive Manufacturing* 28 (2019), pp. 228–235. DOI: 10.1016/j.addma.2019.05.009 (cit. on p. 7).

- [52] Amanda S. Wu, Donald W. Brown, Mukul Kumar, Gilbert F. Gallegos, and Wayne E. King. “An Experimental Investigation into Additive Manufacturing-Induced Residual Stresses in 316L Stainless Steel”. In: *Metallurgical and Materials Transactions A* 45.13 (2014), pp. 6260–6270. DOI: 10.1007/s11661-014-2549-x (cit. on p. 7).
- [53] P. Dong, F. Vecchiato, Z. Yang, P.A. Hooper, and M.R. Wenman. “The effect of build direction and heat treatment on atmospheric stress corrosion cracking of laser powder bed fusion 316L austenitic stainless steel”. In: *Additive Manufacturing* 40 (Apr. 2021), p. 101902. DOI: 10.1016/j.addma.2021.101902 (cit. on p. 7).
- [54] F. Bartolomeu, M. Buciumeanu, E. Pinto, et al. “316L stainless steel mechanical and tribological behavior—A comparison between selective laser melting, hot pressing and conventional casting”. In: *Additive Manufacturing* 16 (2017), pp. 81–89. DOI: 10.1016/j.addma.2017.05.007 (cit. on p. 8).
- [55] M.S. Pham, B. Dovygy, and P.A. Hooper. “Twinning induced plasticity in austenitic stainless steel 316L made by additive manufacturing”. In: *Materials Science and Engineering: A* 704 (2017), pp. 102–111. DOI: 10.1016/j.msea.2017.07.082 (cit. on p. 8).
- [56] Y. Morris Wang, Thomas Voisin, Joseph T. McKeown, et al. “Additively manufactured hierarchical stainless steels with high strength and ductility”. In: *Nature Materials* 17.1 (Oct. 2018), pp. 63–71. DOI: 10.1038/nmat5021 (cit. on p. 8).
- [57] Xianglong Wang, Jose Alberto Muñiz-Lerma, Mohammad Attarian Shandiz, Oscar Sanchez-Mata, and Mathieu Brochu. “Crystallographic-orientation-dependent tensile behaviours of stainless steel 316L fabricated by laser powder bed fusion”. In: *Materials Science and Engineering: A* 766 (Oct. 2019), p. 138395. DOI: 10.1016/j.msea.2019.138395 (cit. on p. 8).
- [58] Q. Portella, M. Chemkhi, and D. Reiraint. “Influence of Surface Mechanical Attrition Treatment (SMAT) post-treatment on microstructural, mechanical and tensile behaviour of additive manufactured AISI 316L”. In: *Materials Characterization* 167 (Sept. 2020), p. 110463. DOI: 10.1016/j.matchar.2020.110463 (cit. on p. 8).
- [59] Sebastien Dryepondt, Peeyush Nandwana, Patxi Fernandez-Zelaia, and Fred List. “Microstructure and high temperature tensile properties of 316L fabricated by laser powder-bed fusion”. In: *Additive Manufacturing* 37 (Jan. 2021), p. 101723. DOI: 10.1016/j.addma.2020.101723 (cit. on p. 8).
- [60] Jong Min Yu, Van Hung Dao, and Kee Bong Yoon. “Effects of scanning speed on creep behaviour of 316L stainless steel produced using selective laser melting”. In: *Fatigue & Fracture of Engineering Materials & Structures* 43.10 (2020), pp. 2312–2325. DOI: 10.1111/ffe.13298 (cit. on pp. 8, 10).
- [61] Jithin James Marattukalam, Dennis Karlsson, Victor Pacheco, et al. “The effect of laser scanning strategies on texture, mechanical properties, and site-specific grain orientation in selective laser melted 316L SS”. In: *Materials & Design* 193 (2020), p. 108852. DOI: 10.1016/j.matdes.2020.108852 (cit. on pp. 8, 37).

- [62] Dirk Herzog, Vanessa Seyda, Eric Wycisk, and Claus Emmelmann. “Additive manufacturing of metals”. In: *Acta Materialia* 117 (Sept. 2016), pp. 371–392. DOI: 10.1016/j.actamat.2016.07.019 (cit. on p. 8).
- [63] A. Leicht, M. Rashidi, U. Klement, and E. Hryha. “Effect of process parameters on the microstructure, tensile strength and productivity of 316L parts produced by laser powder bed fusion”. In: *Materials Characterization* 159 (Jan. 2020), p. 110016. DOI: 10.1016/j.matchar.2019.110016 (cit. on p. 8).
- [64] JH Driver, C Gorlier, C Belrami, P Violan, and C Amzallag. “Influence of Temperature and Environment on the Fatigue Mechanisms of Single-Crystal and Polycrystal 316L”. In: *Low Cycle Fatigue*. Ed. by H. Solomon, G. Halford, L. Kaisand, and B. Leis. West Conshohocken, PA: ASTM International, 1988, pp. 438–455. DOI: 10.1520/stp24496s (cit. on pp. 8, 98).
- [65] G. Ziółkowski, E. Chlebus, P. Szymczyk, and J. Kurzac. “Application of X-ray CT method for discontinuity and porosity detection in 316L stainless steel parts produced with SLM technology”. In: *Archives of Civil and Mechanical Engineering* 14.4 (Aug. 2014), pp. 608–614. DOI: 10.1016/j.acme.2014.02.003 (cit. on p. 9).
- [66] Arthur Conan Doyle. *The Adventure of the Blanched Soldier*. The Case-Book of Sherlock Holmes. John Murray, 1927 (cit. on p. 10).
- [67] L. A. Ávila Calderón, B. Rehmer, S. Schriever, et al. “Creep and creep damage behavior of stainless steel 316L manufactured by laser powder bed fusion”. In: *Materials Science and Engineering: A* 830 (Jan. 2022), p. 142223. DOI: 10.1016/j.msea.2021.142223 (cit. on pp. 10, 11, 31, 34, 35, 67, 71, 78, 95).
- [68] Ester D’Accardi, Simon J. Altenburg, Christiane Maierhofer, Davide Palumbo, and Umberto Galietti. “Detection of Typical Metal Additive Manufacturing Defects by the Application of Thermographic Techniques”. In: *The 15th International Workshop on Advanced Infrared Technology and Applications 17-19.09.2019*. Vol. 27. 1. Firenze, Italy: MDPI AG, Sept. 2019, p. 24. DOI: 10.3390/proceedings2019027024 (cit. on p. 11).
- [69] Nils Scheuschner, Simon J. Altenburg, Giuseppe Pignatelli, et al. “Vergleich der Messungen der Schmelzbadtemperatur bei der Additiven Fertigung von Metallen mittels IR-Spektroskopie und Thermografie”. In: *tm - Technisches Messen* 88.10 (July 2021), pp. 626–632. DOI: 10.1515/teme-2021-0056 (cit. on p. 11).
- [70] Tobias Thiede, Tatiana Mishurova, Sergei Evsevlev, et al. “3D Shape Analysis of Powder for Laser Beam Melting by Synchrotron X-ray CT”. In: *Quantum Beam Science* 3.1 (2019). DOI: 10.3390/qubs3010003 (cit. on pp. 11, 84).
- [71] Tiago Werner, Mauro Madia, and Uwe Zerbst. “Comparison of the fatigue behavior of wrought and additively manufactured AISI 316L”. In: *Procedia Structural Integrity* 38 (2022), pp. 554–563. DOI: 10.1016/j.prostr.2022.03.056 (cit. on p. 11).

- [72] G. N. Hounsfield. “Computerized transverse axial scanning (tomography): Part 1. Description of system”. In: *The British Journal of Radiology* 46.552 (1973). PMID: 4757352, pp. 1016–1022. DOI: 10.1259/0007-1285-46-552-1016 (cit. on p. 13).
- [73] E. Maire and P. J. Withers. “Quantitative X-ray tomography”. In: *International Materials Reviews* 59.1 (Dec. 2013), pp. 1–43. DOI: 10.1179/1743280413y.0000000023 (cit. on p. 13).
- [74] Thorsten M. Buzug. *Einführung in die Computertomographie*. Springer Berlin Heidelberg, 2004. 432 pp. (cit. on pp. 13, 16, 17).
- [75] Wilhelm Conrad Röntgen. “Ueber eine neue Art von Strahlen. (Vorläufige Mittheilung.)” In: *Aus den Sitzungsberichten der Würzburger Physik.-medic. Gesellschaft*. Stahel’sche K. Hof- und Universitätsbuch- und Kunsthandlung, 1895, pp. 137–147 (cit. on p. 15).
- [76] Wilhelm Conrad Röntgen. “Ueber eine neue Art von Strahlen. (Fortsetzung.)” In: *Sitzungsberichte der Würzburger Physik.-medic. Gesellschaft*. Stahel’sche K. Hof- und Universitätsbuch- und Kunsthandlung, 1896, pp. 1–9 (cit. on p. 15).
- [77] Wilhelm Conrad Röntgen. “Weitere Beobachtungen über die Eigenschaften der X-Strahlen.” In: *Sitzungsberichte der Königlich Preußischen Akademie der Wissenschaften zu Berlin. Erster Halbband*. Verlag der Königlichen Akademie der Wissenschaften, 1897, pp. 576–592 (cit. on p. 15).
- [78] Johann Heinrich Lambert. *Photometria, sive de mensura et gradibus luminis, colorum et umbrae (Photometry, or, On the measure and gradations of light, colors, and shade)*. Ed. by Augustae Vindelicorum. Augsburg: Eberhardi Klett, 1760, p. 547. DOI: 10.3931/e-rara-9488 (cit. on p. 16).
- [79] August Beer. “Bestimmung der Absorption des rothen Lichts in farbigen Flüssigkeiten”. In: *Annalen der Physik* 162.5 (1852), pp. 78–88. DOI: 10.1002/andp.18521620505 (cit. on p. 16).
- [80] Efrat Shefer, Ami Altman, Rolf Behling, et al. “State of the Art of CT Detectors and Sources: A Literature Review”. In: *Current Radiology Reports* 1.1 (2013), pp. 76–91. DOI: 10.1007/s40134-012-0006-4 (cit. on p. 17).
- [81] Johann Radon. “Ueber die Bestimmung von Funktionen durch ihre Integralwerte längs gewisser Mannigfaltigkeiten”. In: *Berichte der mathematisch -physikalischen Kl. Sächsischen Gesellschaft fuer Wissenschaften* 59 (1917) (cit. on p. 18).
- [82] L. A. Feldkamp, L. C. Davis, and J. W. Kress. “Practical cone-beam algorithm”. In: *J. Opt. Soc. Am. A* 1.6 (1984), pp. 612–619. DOI: 10.1364/JOSAA.1.000612 (cit. on p. 19).
- [83] D. Einfeld. “Appendix A: Synchrotron radiation characteristics”. en. In: *SEE-LS: A 4th Generation Synchrotron Light Source for Science and Technology*. CERN, Geneva, Switzerland, 2020, pp. 171–188. DOI: 10.23731/CYRM-2020-001.171 (cit. on p. 22).

- [84] Amardeep Bharti and Navdeep Goyal. “Fundamental of Synchrotron Radiations”. In: *Synchrotron Radiation*. Ed. by Daisy Joseph. Rijeka: IntechOpen, 2019. Chap. 2. DOI: 10.5772/intechopen.82202 (cit. on p. 22).
- [85] Antoni Buades, Bartomeu Coll, and Jean-Michel Morel. “Non-Local Means Denoising”. In: *Image Processing On Line* 1 (2011). DOI: 10.5201/ipo1.2011.bcm_nlm (cit. on p. 23).
- [86] J. Darbon, A. Cunha, T. F. Chan, S. Osher, and G. J. Jensen. “Fast nonlocal filtering applied to electron cryomicroscopy”. In: *2008 5th IEEE International Symposium on Biomedical Imaging: From Nano to Macro* (2008), pp. 1331–1334. DOI: 10.1109/ISBI.2008.4541250 (cit. on p. 23).
- [87] Johannes Schindelin, Ignacio Arganda-Carreras, Erwin Frise, et al. “Fiji: an open-source platform for biological-image analysis”. In: *Nature Methods* 9.7 (2012), pp. 676–682. DOI: 10.1038/nmeth.2019 (cit. on pp. 23, 66).
- [88] Stuart Berg, Dominik Kutra, Thorben Kroeger, et al. “ilastik: interactive machine learning for (bio)image analysis”. In: *Nature Methods* (Sept. 2019). DOI: 10.1038/s41592-019-0582-9 (cit. on p. 23).
- [89] Peter Staron, Andreas Schreyer, Helmut Clemens, and Svea Mayer, eds. *Neutrons and Synchrotron Radiation in Engineering Materials Science: From Fundamentals to Applications*. 2nd ed. Wiley VCH Verlag GmbH & Co. KGaA, 2017. DOI: 10.1002/9783527684489 (cit. on pp. 24, 26, 29).
- [90] U. Wolfstieg and E. Macherauch. “Ursachen und Bewertung von Eigenspannungen.” In: *Chemie Ingenieur Technik* 45.11 (1973), pp. 760–770. DOI: 10.1002/cite.330451103 (cit. on p. 24).
- [91] M. Hutchings, P. Withers, T. Holden, and T. Lorentzen. *Introduction to the Characterization of Residual Stress by Neutron Diffraction*. Boca Raton: CRC Press, 2005. DOI: 10.1201/9780203402818 (cit. on pp. 27, 29, 57).
- [92] William Henry Bragg and William Lawrence Bragg. “The reflection of X-rays by crystals”. In: *Proceedings of the Royal Society of London. Series A, Containing Papers of a Mathematical and Physical Character* 88.605 (1913), pp. 428–438. DOI: 10.1098/rspa.1913.0040 (cit. on p. 28).
- [93] John Douglas Eshelby and Rudolf Ernst Peierls. “The determination of the elastic field of an ellipsoidal inclusion, and related problems”. In: *Proceedings of the Royal Society of London. Series A. Mathematical and Physical Sciences* 241.1226 (1957), pp. 376–396. DOI: 10.1098/rspa.1957.0133 (cit. on p. 29).
- [94] Ekkehart Kröner. “Berechnung der elastischen Konstanten des Vielkristalls aus den Konstanten des Einkristalls”. In: *Zeitschrift für Physik* 151.4 (1958), pp. 504–518. DOI: 10.1007/BF01337948 (cit. on p. 29).
- [95] Michael Hofmann, Weimin Gan, and Joana Rebelo-Kornmeier. “STRESS-SPEC: Materials science diffractometer”. In: *Journal of large-scale research facilities JLSRF* 1 (2015). DOI: 10.17815/jlsrf-1-25 (cit. on pp. 29, 57).

- [96] Gunther Mohr, Nils Scheuschner, and Kai Hilgenberg. “In situ heat accumulation by geometrical features obstructing heat flux and by reduced inter layer times in laser powder bed fusion of AISI 316L stainless steel”. In: *Procedia CIRP* 94 (2020), pp. 155–160. DOI: 10.1016/j.procir.2020.09.030 (cit. on p. 31).
- [97] Christian Gobert, Edward W. Reutzel, Jan Petrich, Abdalla R. Nassar, and Shashi Phoha. “Application of supervised machine learning for defect detection during metallic powder bed fusion additive manufacturing using high resolution imaging”. In: *Additive Manufacturing* 21 (2018), pp. 517–528. DOI: 10.1016/j.addma.2018.04.005 (cit. on p. 37).
- [98] Tyler Oesch, Frank Weise, Dietmar Meinel, and Christian Gollwitzer. “Quantitative In-situ Analysis of Water Transport in Concrete Completed Using X-ray Computed Tomography”. In: *Transport in Porous Media* 127.2 (2019), pp. 371–389. DOI: 10.1007/s11242-018-1197-9 (cit. on pp. 46, 52, 62).
- [99] Joachim Bamberg, Günter Zenzinger, and Alexander Ladewig. “In-process control of selective laser melting by quantitative optical tomography”. In: *19th World Conference on Non-Destructive Testing*. 2016 (cit. on p. 52).
- [100] Deniz Sera Ertay, Henry Ma, and Mihaela Vlasea. “Correlative Beam Path and Pore Defect Space Analysis for Modulated LPBF Process”. In: *The 2018 Annual International Solid Freeform Fabrication (SFF) Symposium—An Additive Manufacturing (AM) Conference* (2018). DOI: 10.26153/tsw/17015 (cit. on p. 53).
- [101] Anton du Plessis. “Effects of process parameters on porosity in laser powder bed fusion revealed by X-ray tomography”. In: *Additive Manufacturing* 30 (Dec. 2019), p. 100871. DOI: 10.1016/j.addma.2019.100871 (cit. on p. 53).
- [102] Elliott W. Jost, John C. Miers, Aron Robbins, David G. Moore, and Christopher Saldana. “Effects of spatial energy distribution-induced porosity on mechanical properties of laser powder bed fusion 316L stainless steel”. In: *Additive Manufacturing* 39 (Mar. 2021), p. 101875. DOI: 10.1016/j.addma.2021.101875 (cit. on p. 53).
- [103] Lore Thijs, Frederik Verhaeghe, Tom Craeghs, Jan Van Humbeeck, and Jean-Pierre Kruth. “A study of the microstructural evolution during selective laser melting of Ti–6Al–4V”. In: *Acta Materialia* 58.9 (2010), pp. 3303–3312. DOI: 10.1016/j.actamat.2010.02.004 (cit. on p. 62).
- [104] I. Yadroitsev, L. Thivillon, Ph. Bertrand, and I. Smurov. “Strategy of manufacturing components with designed internal structure by selective laser melting of metallic powder”. In: *Applied Surface Science* 254.4 (2007). Laser synthesis and processing of advanced materials, pp. 980–983. DOI: 10.1016/j.apsusc.2007.08.046 (cit. on p. 62).
- [105] Erik R. Denlinger, Vijay Jagdale, G. V. Srinivasan, Tahany El-Wardany, and Pan Michaleris. “Thermal modeling of Inconel 718 processed with powder bed fusion and experimental validation using in situ measurements”. In: *Additive Manufacturing* 11 (2016), pp. 7–15. DOI: 10.1016/j.addma.2016.03.003 (cit. on p. 86).

- [106] E. L. Li, L. Wang, A. B. Yu, and Z. Y. Zhou. “A three-phase model for simulation of heat transfer and melt pool behaviour in laser powder bed fusion process”. In: *Powder Technology* 381 (2021), pp. 298–312. DOI: 10.1016/j.powtec.2020.11.061 (cit. on p. 87).
- [107] Chunlei Qiu, Chinnapat Panwisawas, Mark Ward, et al. “On the role of melt flow into the surface structure and porosity development during selective laser melting”. In: *Acta Materialia* 96 (2015), pp. 72–79. DOI: 10.1016/j.actamat.2015.06.004 (cit. on p. 88).
- [108] S. J. Clark, C. L. A. Leung, Y. Chen, et al. “Capturing Marangoni flow via synchrotron imaging of selective laser melting”. In: *IOP Conference Series: Materials Science and Engineering* 861 (2020), p. 012010. DOI: 10.1088/1757-899x/861/1/012010 (cit. on p. 88).
- [109] H. Yeung, B. M. Lane, M. A. Donmez, J. C. Fox, and J. Neira. “Implementation of Advanced Laser Control Strategies for Powder Bed Fusion Systems”. In: *Procedia Manufacturing* 26 (2018), pp. 871–879. DOI: 10.1016/j.promfg.2018.07.112 (cit. on p. 90).
- [110] Erik R. Denlinger, Michael Gouge, Jeff Irwin, and Pan Michaleris. “Thermomechanical model development and in situ experimental validation of the Laser Powder-Bed Fusion process”. In: *Additive Manufacturing* 16 (2017), pp. 73–80. DOI: 10.1016/j.addma.2017.05.001 (cit. on p. 92).

Colophon

This thesis was typeset with $\text{\LaTeX}2_{\epsilon}$. It uses the *Clean Thesis* style developed by Ricardo Langner. The design of the *Clean Thesis* style is inspired by user guide documents from Apple Inc.

Download the *Clean Thesis* style at <http://cleanthesis.der-ric.de/>.